AD NUMBER

AD827106

LIMITATION CHANGES

TO:

Approved for public release; distribution is unlimited.

FROM:

Distribution authorized to U.S. Gov't. agencies and their contractors; Critical Technology; JAN 1968. Other requests shall be referred to Air Force Aero Proplsion Lab., Research and Technology Div., Attn: APIE-1, Wright-Patterson AFB, OH 45433. This document contains export-controlled technical data.

AUTHORITY

AFAPL ltr dtd 12 Apr 1972

AFAPL-TR-67-139

INDUCTIVE PLASMA ACCELERATOR DEVELOPMENT

TECHNICAL DOCUMENT REPORT No. AFAPL-TR-67-139

JANUARY, 1968

AIR FORCE PROPULSION LABORATORY
RESEARCH AND TECHNOLOGY DIVISION
AIR FORCE SYSTEMS COMMAND
WRIGHT PATTERSON AIR FORCE BASE, OHIO

Project No. 3141, Task No. 27614

(Prepared under Contract No. AF 33(615)-3744 by the Space Sciences Laboratories of the Applied Technology Division of Litton Systems, Inc., Beverly Hills, California; G. Fonda-Bonardi and R. Rosen, Authors)

PAGES _____

ARE

MISSING

IN

ORIGINAL

DOCUMENT

NOTICES

When Government drawings, specifications, or other data are used for any purpose other than in connection with a definitely related Government procurement operation, the United States Government thereby incurs no responsibility nor any obligation whatsoever; and the fact that the Government may have formulated, furnished, or in any way supplied the said drawings, specifications, or other data, is not to be regarded by implication or otherwise as in any manner licensing the holder or any other person or corporation, or conveying any rights or permission to manufacture, use, or sell any patented invention that may in any way be related thereto.

This document is subject to special export controls and each transmittal to foreign governments or foreign nationals may be made only with prior approval to the AFAPL (APIE-1).

Foreign announcement and dissemination of this report by DDC is not authorized.

Copies of this report should not be returned unless return is required by security considerations, contractual obligations, or notice on a specific document.

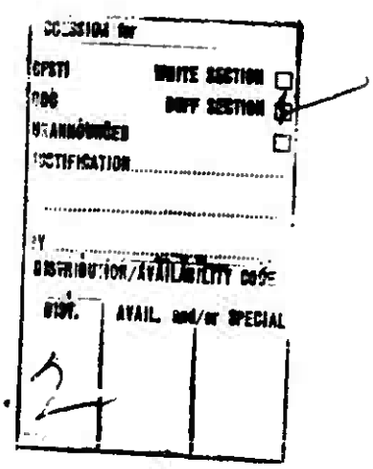

FOREWORD

This report (Litton Publication No. 7244) was prepared by the Space Sciences Laboratories of Litton Systems, Inc., at 336 N. Foothill Road, Beverly Hills, California, under Contract No. AF 33(615)-3744, covering the period from 1 July 1966 to 31 July 1967.

This document is a revision of prior Litton publication No. 6730, and was monitored by the Air Force Aero Propulsion Laboratory with Mr. Richard B. Rivir as the USAF Project Engineer.

Publication of this report does not constitute Air Force approval of the report's findings or conclusions. It is published only for the exchange and stimulation of ideas.

Paul E. Peko, Major, USAF
Chief, Propulsion and Power Branch

STATEMENT #2 UNCLASSIFIED

This document is subject to special export controls and each transmittal to foreign governments or foreign nationals may be made only with prior approval of AFAPL Attn: APIE-1 W-P AFB, Ohio 45433

ABSTRACT

The work described in this report comprises:

a. Theoretical studies of the performance of an electromagnetic induction plasma accelerator for radiation-cooled applications, and for pulsed operation.

b. The improvement of pre-existing instrumentation for the measurement of developed thrust and input electric power.

c. The development of suitable materials and techniques for the construction of thrustors.

d. The experimental testing of thrustors for the purpose of measuring performance and life times.

LIST OF ILLUSRTATIONS

LIST OF ILLUSTRATIONS (cont)

LIST OF ILLUSTRATIONS (cont)

LIST OF ILLUSTRATIONS (cont)

1. INTRODUCTION

The work described in this report is a continuation of work done under Contract AF 33(657)8697 and summarized in Report AFAPL-TR-65-49[1], which will be referred to hereinafter as the Report, since many occasions will be found to use information therein presented.

The work here described can be divided in four major areas:

a. Theoretical studies of the performance of the thrustor for the case in which ferrites cannot be used because the operating temperature exceeds the curie point of the materials. This condition applies when the thrustor is operated in the radiation-cooled mode. Another theoretical aspect investigated was pulsed operation, in which high instantaneous power, compatible with high efficiency, is used for short periods of time so as to generate low average thrust at low average power level.

b. Improvement of the experimental facility, particularly in respect to the maintaining of better vacuum during long thrustor firing, and the improvement of the precision of measurement for thrust and electrical input power.

c. Development of materials and techniques for the fabrication of thrustors capable of extended firing times in the radiation-cooled mode as well as in the water-cooled mode.

d. Experimental measurement of performance data, conditioned upon the availability of thrustors capable of being operated for sufficiently long times at sufficiently high power levels, and therefore upon satisfactory progress under point c. above.

Work done in each of the above areas is described in detail in the remainder of this report.

---

[1]Fonda-Bonardi, G. "Development of a plasma accelerator for thrust," Final report on Contract AF 33(657)8697, Litton Publication No. 4231, April 1967

2. THEORETICAL CONSIDERATIONS

2.1 GENERAL

Three topics have been considered during the present research period. The first two concern the present experimental device and the third topic considers a possible future thrustor mode of operation. In the order discussed they are:

2.2 Radiation-cooled thrustor design and performance

2.3 Thrustor models

2.4 Pulsed-mode thrustor operation

One of the main objectives of this research period was the development of a radiation-cooled thrustor in contrast to the water-cooled thrustor of Contract AF 33(657)-8697. Experiments showed (see Section 5.2) that at the design power levels, a radiation cooled coil would run at temperatures exceeding the Curie point of magnetic materials and far beyond that of ferrites. A radiation-cooled coil was designed by methods shown in the Report sec 2 and details are given below. The coil has closely the same dimensional and magnetic characteristics of the previous water-cooled coils at the expense of higher I^2R losses. The present performance analysis includes these losses. Since the original work was done at 240 Khz and all the instrumentation was developed for this frequency, a performance vs. frequency analysis was made to see whether performance peaks were close enough to 240 Khz or whether a large shift might be needed.

The losses associated with fractional mass utilization were also analyzed for a thrustor model in which resonant charge-exchange effects are not dominant, and an estimate was made of the charge-exchange mean free path in the interaction region of the thrustor.

The high efficiencies (indicated in the Report) of the water-cooled thrustor were obtained at high power levels, which may exceed the average power available for certain missions for which the thrustor may be otherwise attractive. However, if the thrustor could be run in a pulsed mode at low duty cycle, high peak power could be applied at low average power, therefore taking advantage of the high power-high efficiency thrustor characteristics. At the time of this writing, high efficiency data points were not available for the current coil design so the original data points of the Report were used.

2.2 RADIATION-COOLED THRUSTOR DESIGN AND PERFORMANCE CALCULATIONS

Figures 2-1, 2-2, and 2-3 show respectively the magnetic flux pattern, the inductive potential pattern, and the axial dependence of the inductive potential for the radiation-cooled thrustor. These are to be compared to Figures 2-23, 2-24 and 2-13 of the Report which are the corresponding plots for the water-cooled thrustor. It should be noted that the Report calculation were done for coil currents in ampereturns and the present calculation expresses the current in amperes. The trajectory equation for the plasma (Eqn. 2.11 of the Report) is:

$$\frac{d^2z}{dt^2} = 4.355 \times 10^7 \, I_o^{\,2} \, e^{-34.12z} \, \sin^2 \omega t$$

where I_o is the coil current in peak amperes. The digital computer available in the laboratory was programmed to solve this differential equation for a series of value of the operating frequency $f = \omega/2\pi$. The first plot of this series is shown in Figure 2-4, which presents the terminal exhaust velocity of the thrustor as a function of frequency and coil current. This plot is the limiting case of zero mass flow (therefore zero thrust), i. e. there are no de-coupling effects due to plasma currents and in a way this represents an ideal thrustor. When plasma currents de-couple the coil from the plasma more coil current is needed to produce the same output velocity, Section 2.3.2 of the Report is an analysis of the loading effect. Equation 2.37 of the Report allows one to calculate the currents needed when the plasma loads the thrustor and Figures 2-5 through 2-15 show the results of the calculation applied to the radiation-cooled coil. This series show lines of constant coil current as a function of frequency and exhaust velocity for a series of values of thrust from 0.05 to 5.0 newton.

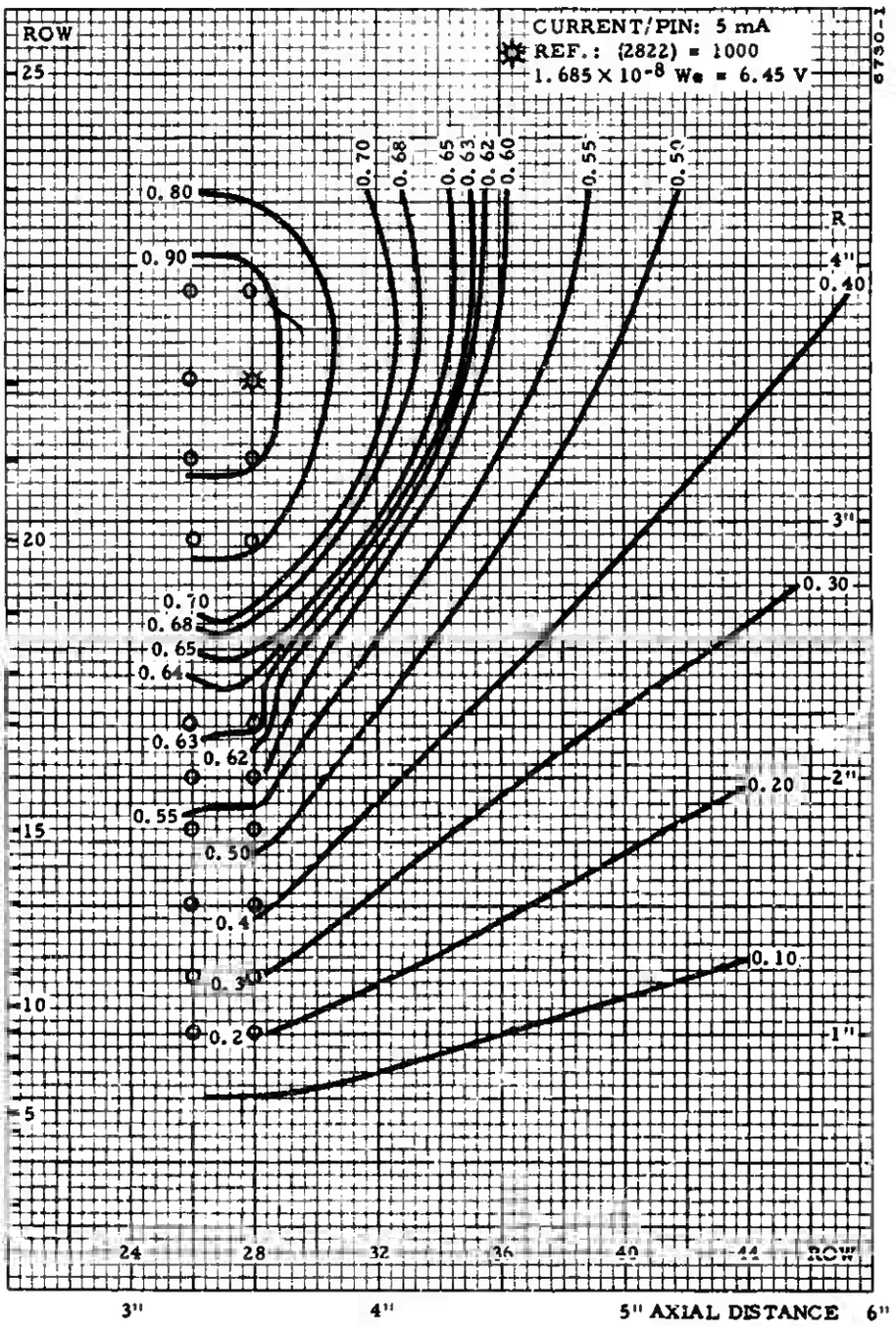

Figure 2-1. Flux Lines of Radiation Cooled Thrustor

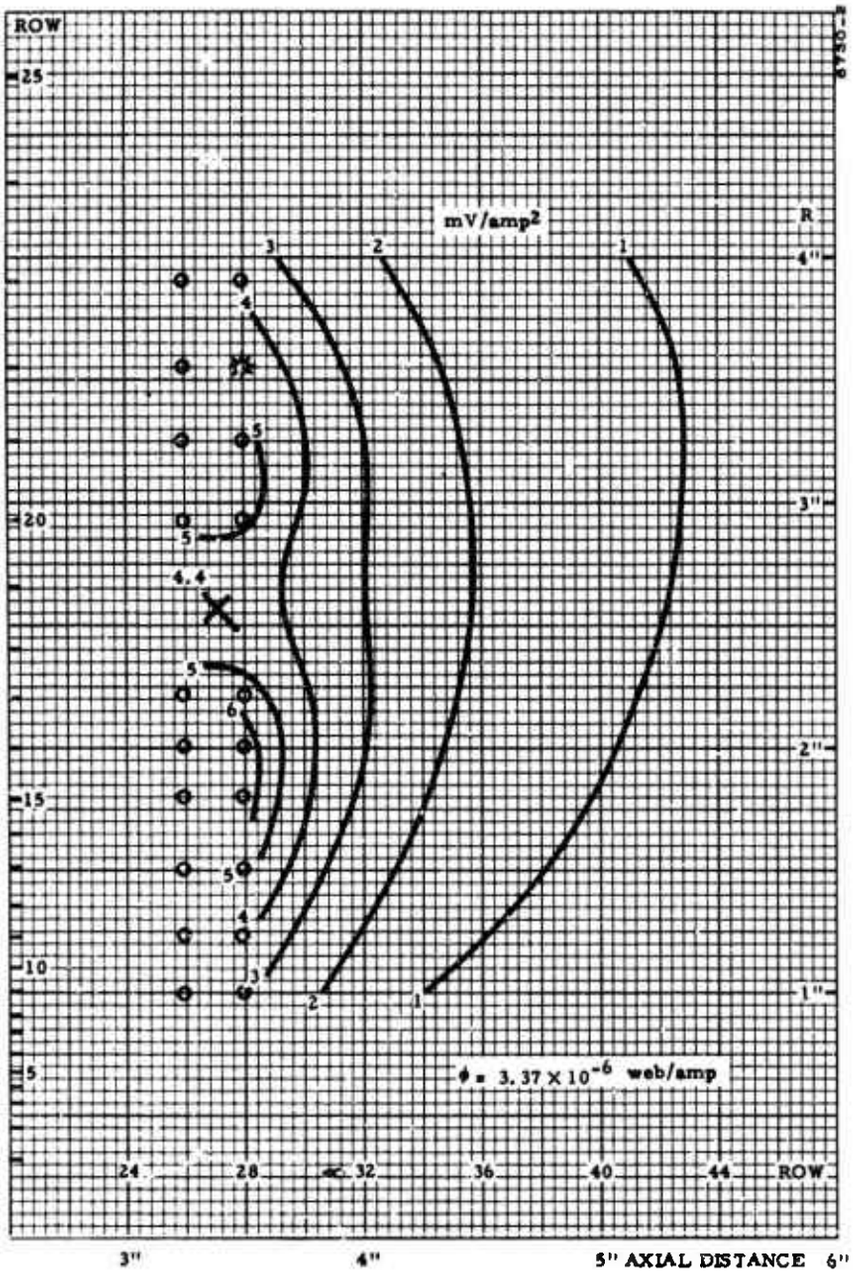

Figure 2-2. Equipotentials of Radiation Cooled Thrustor

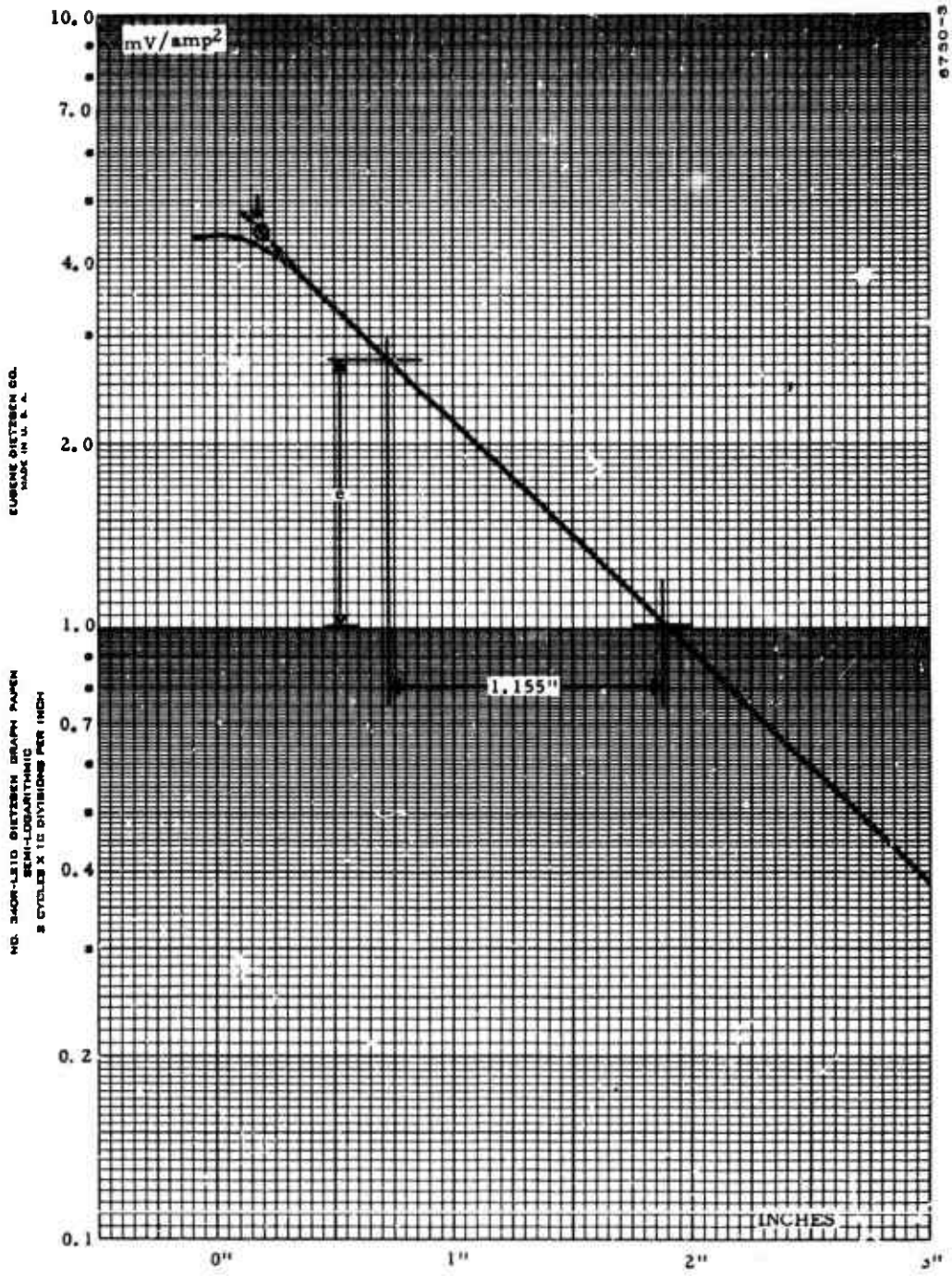

Figure 2-3. Axial Variation of Potential at Constant Radius

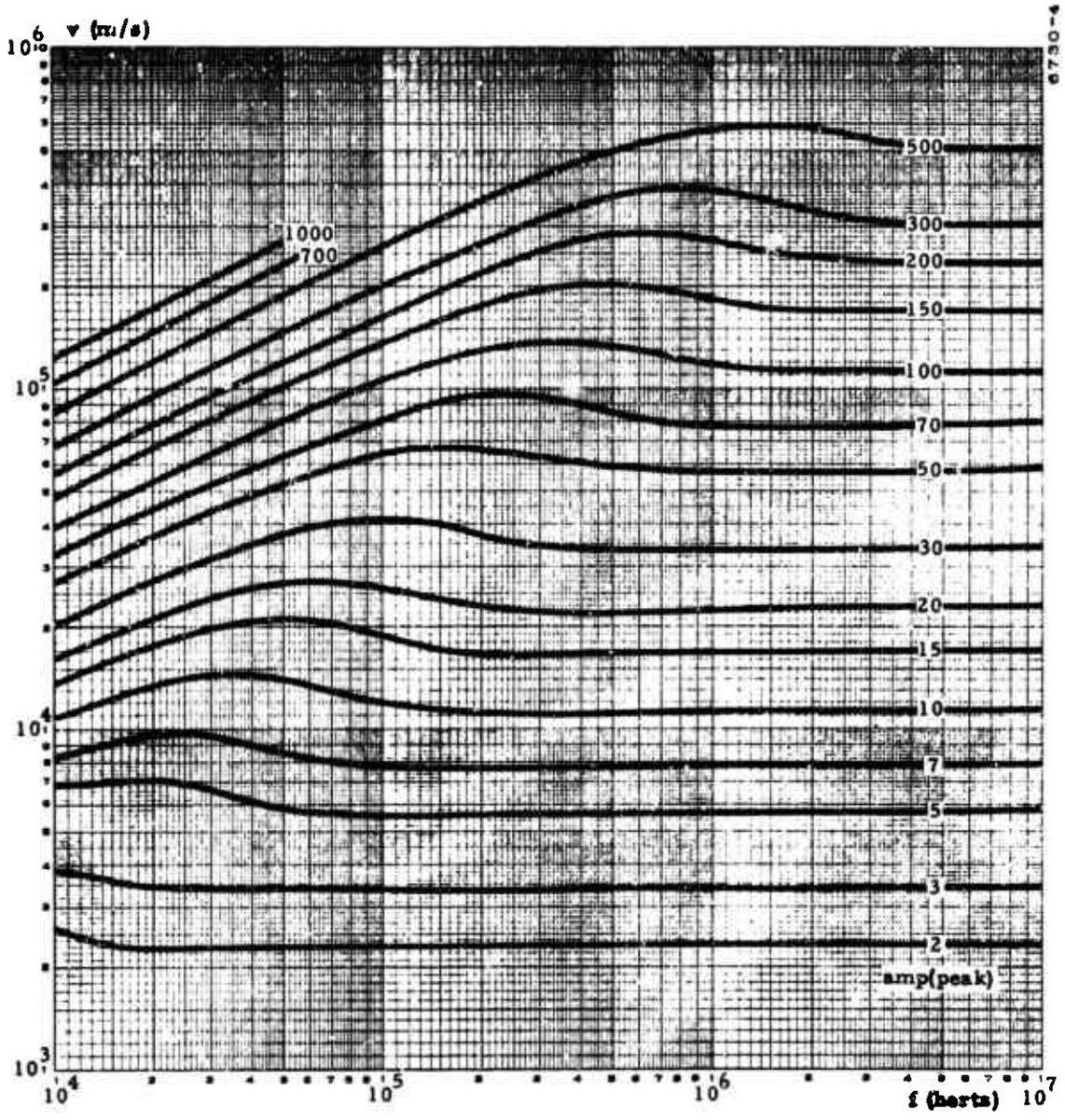

Figure 2-4. Current vs Terminal Velocity and Frequency (Zero Loading: $\tau = 0$)

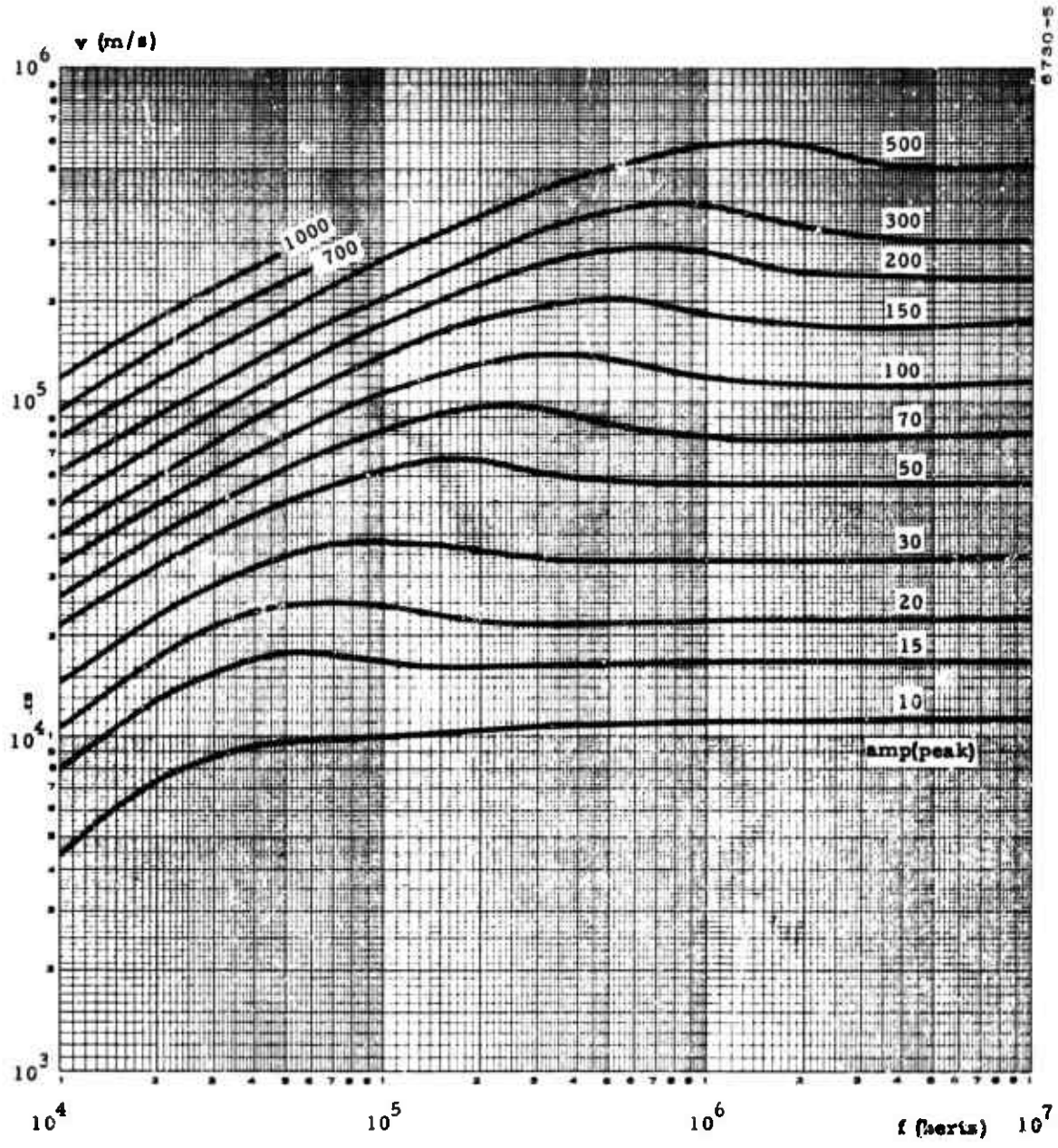

Figure 2-5. Current vs Terminal Velocity and Frequency (T = 0.05 newton)

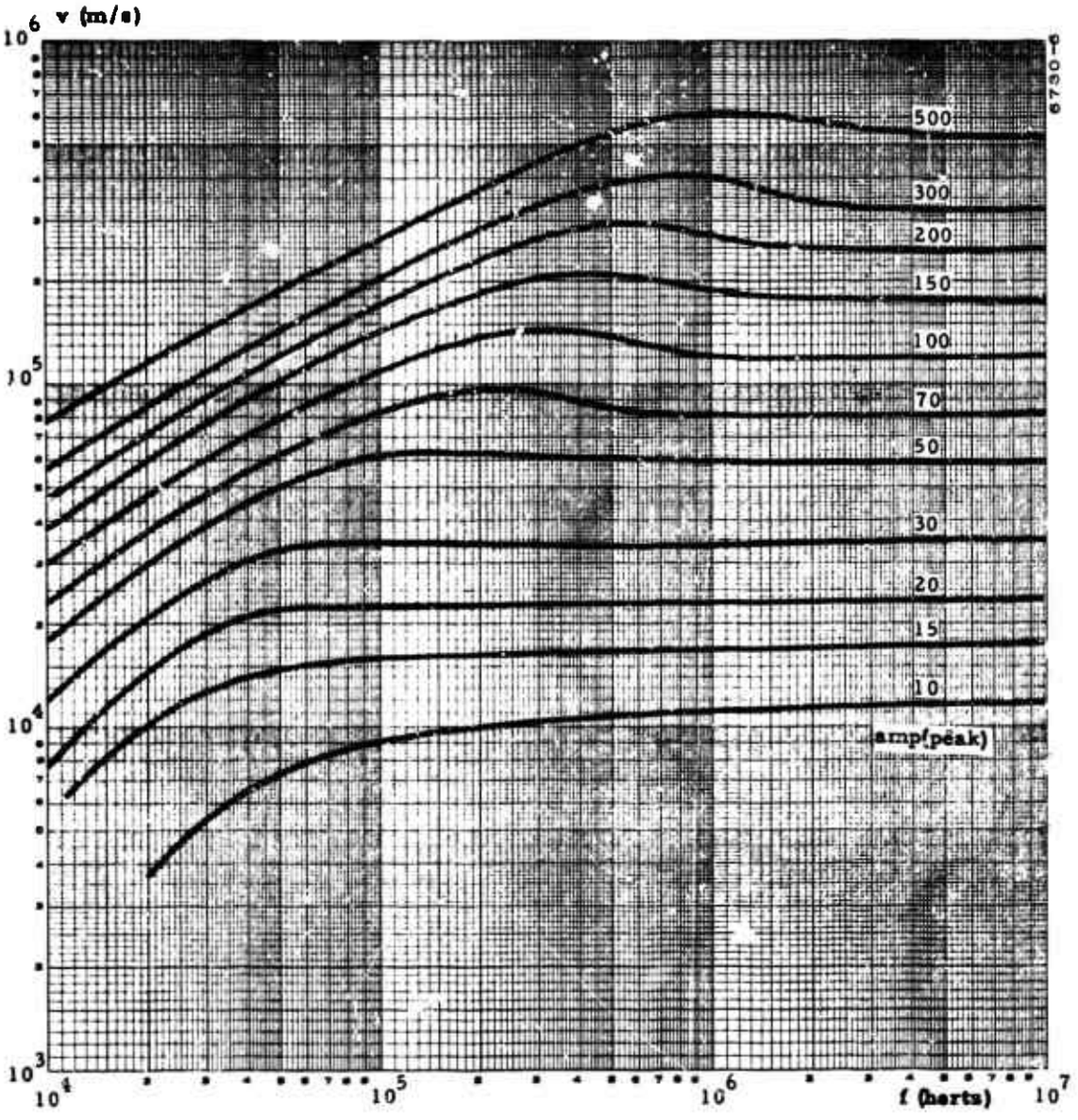

Figure 2-6. Current vs Terminal Velocity and Frequency (T = 0.1 newton)

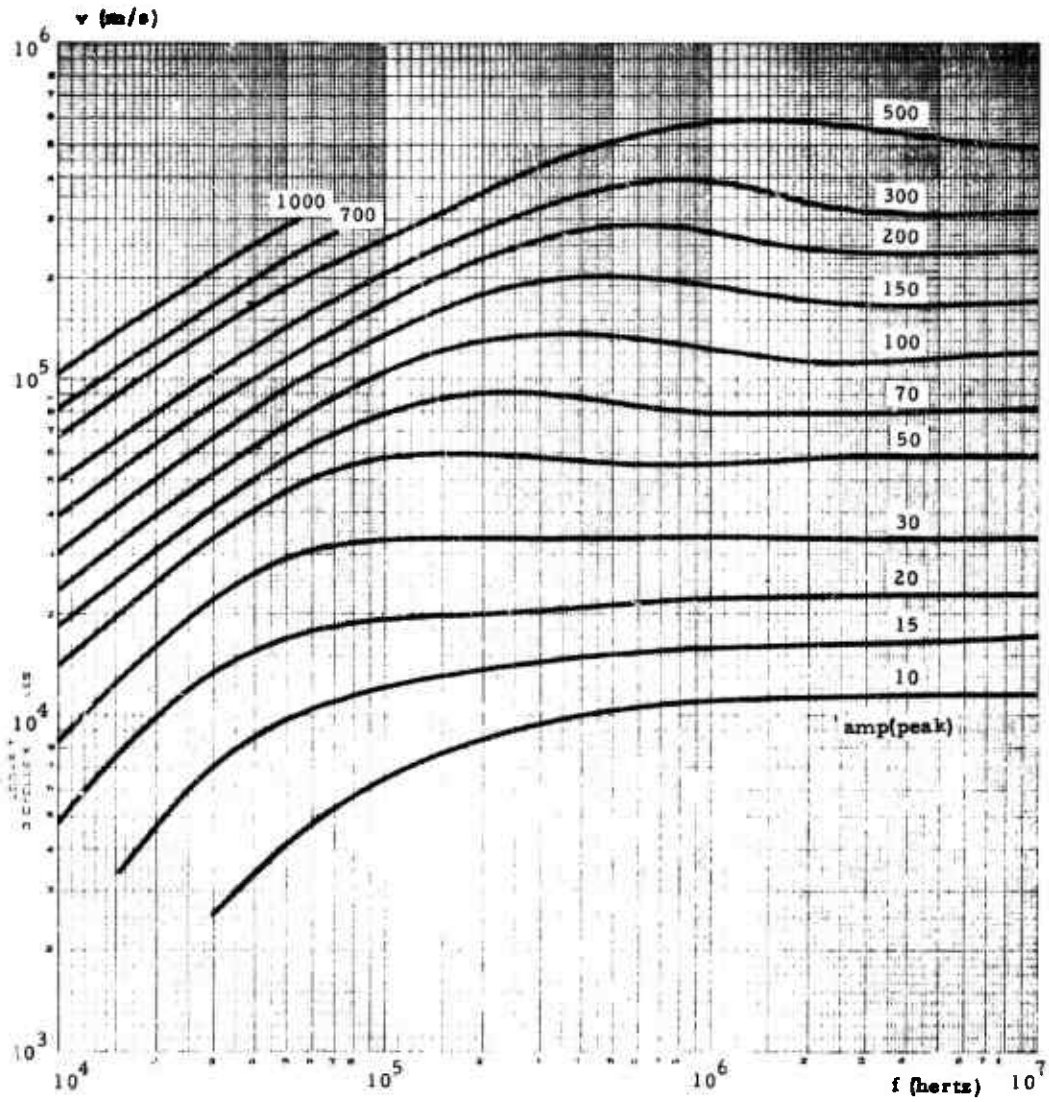

6730-7

Figure 2-7. Current vs Terminal Velocity and Frequency (T = 0.2 newton)

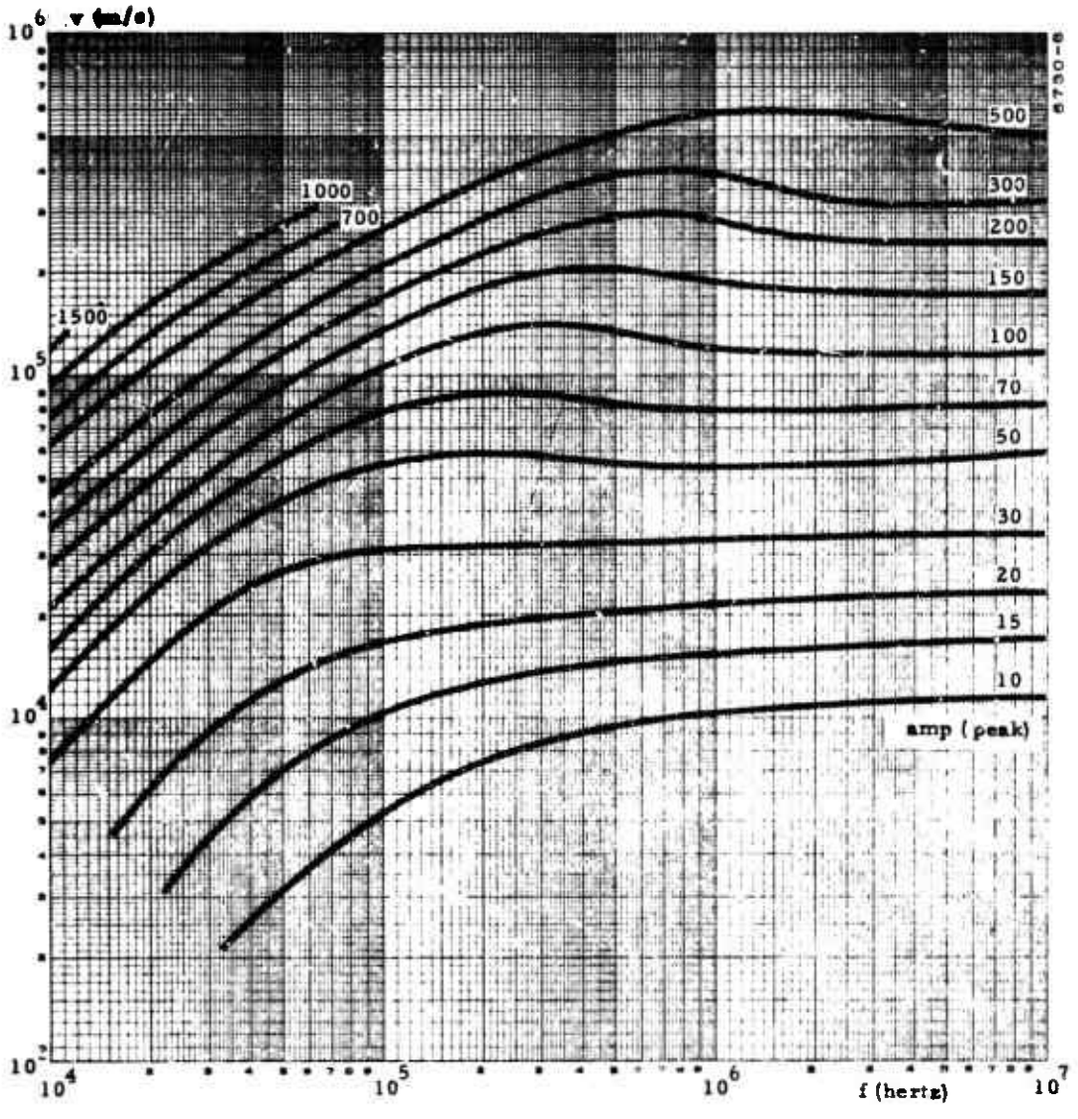

Figure 2-8. Current vs Terminal Velocity and Frequency (T = 0.3 newton)

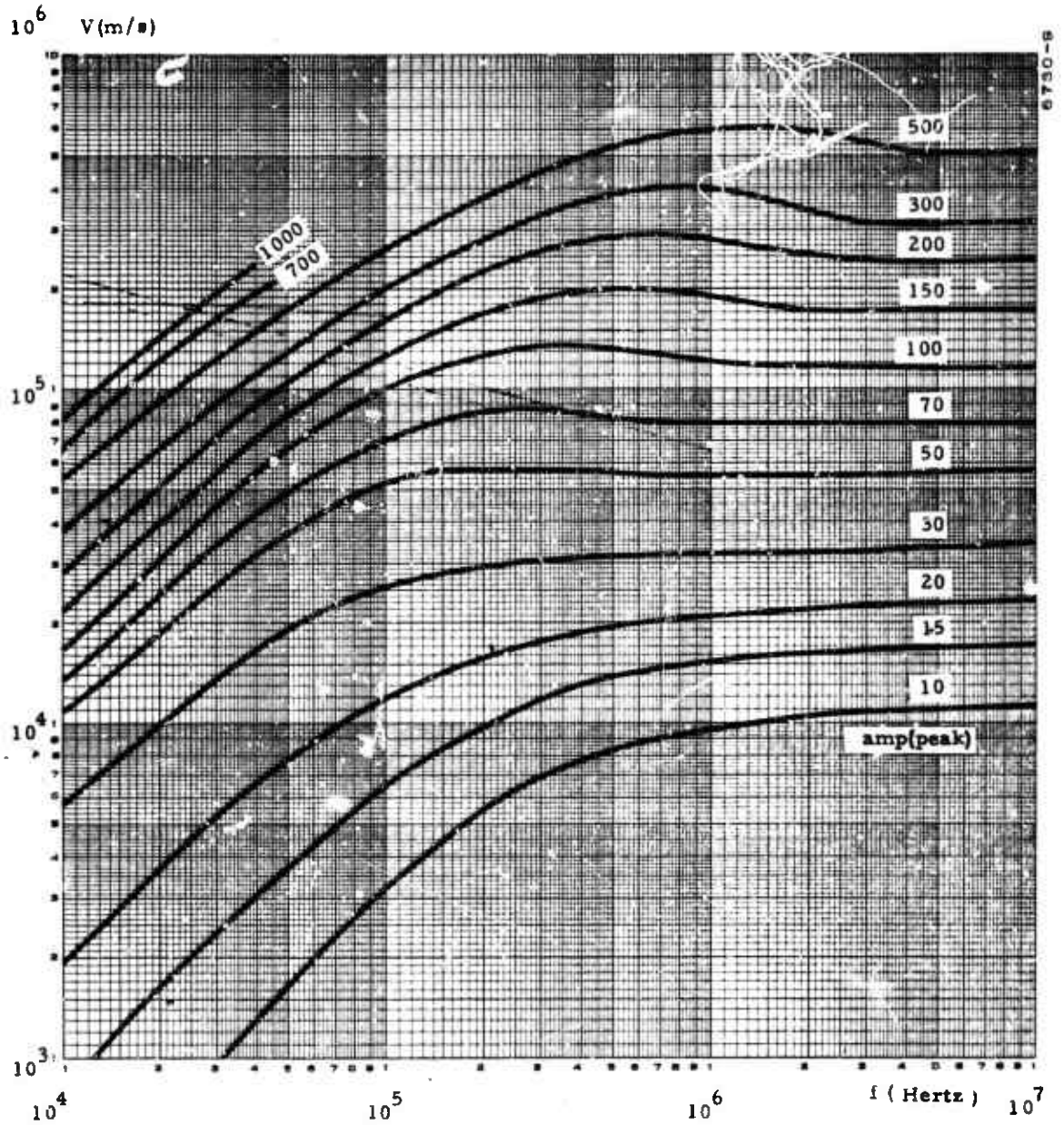

Figure 2-9. Current vs Terminal Velocity and Frequency (T = 0.5 newton)

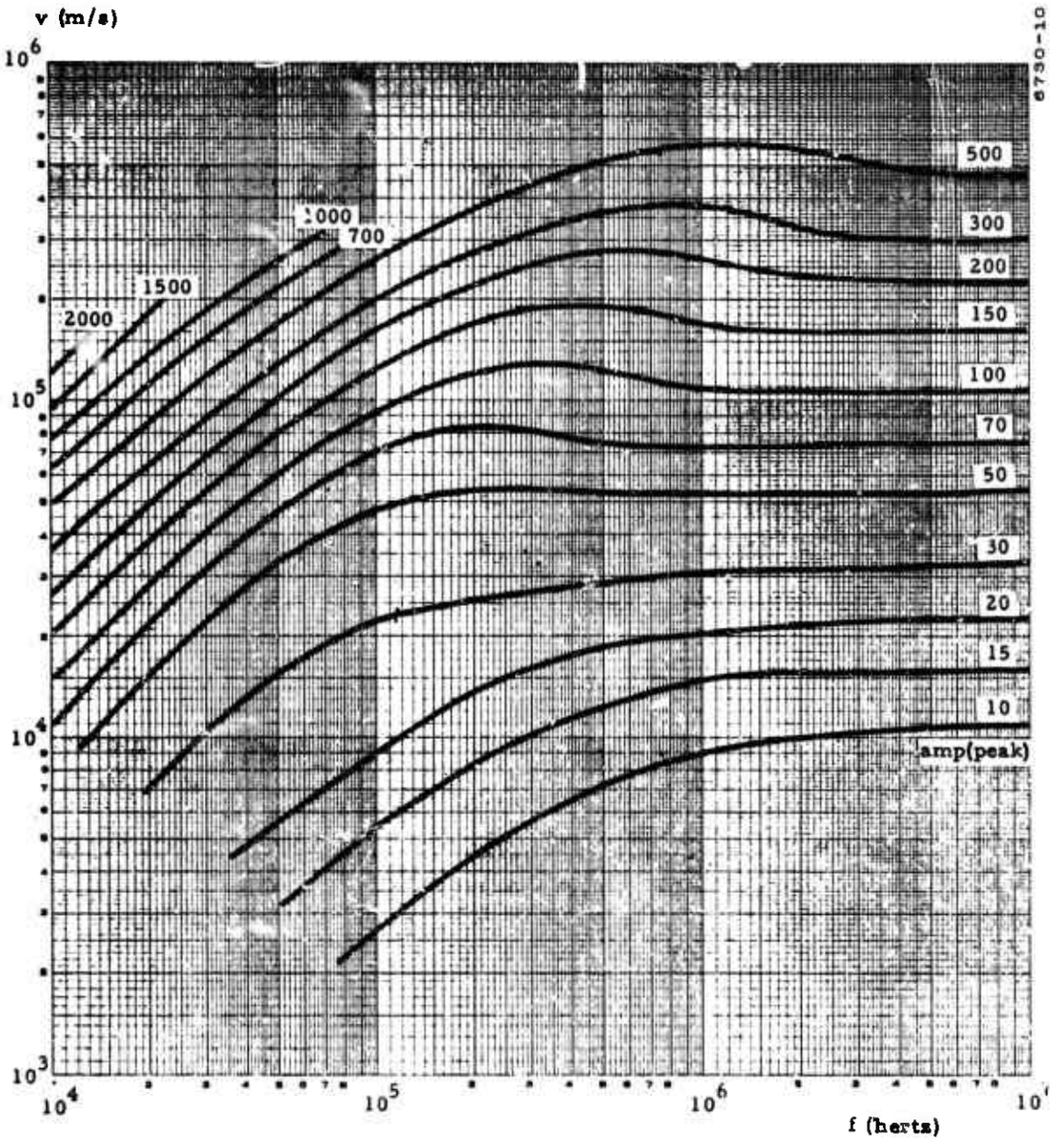

Figure 2-10. Current vs Terminal Velocity and Frequency (T = 0.7 newton)

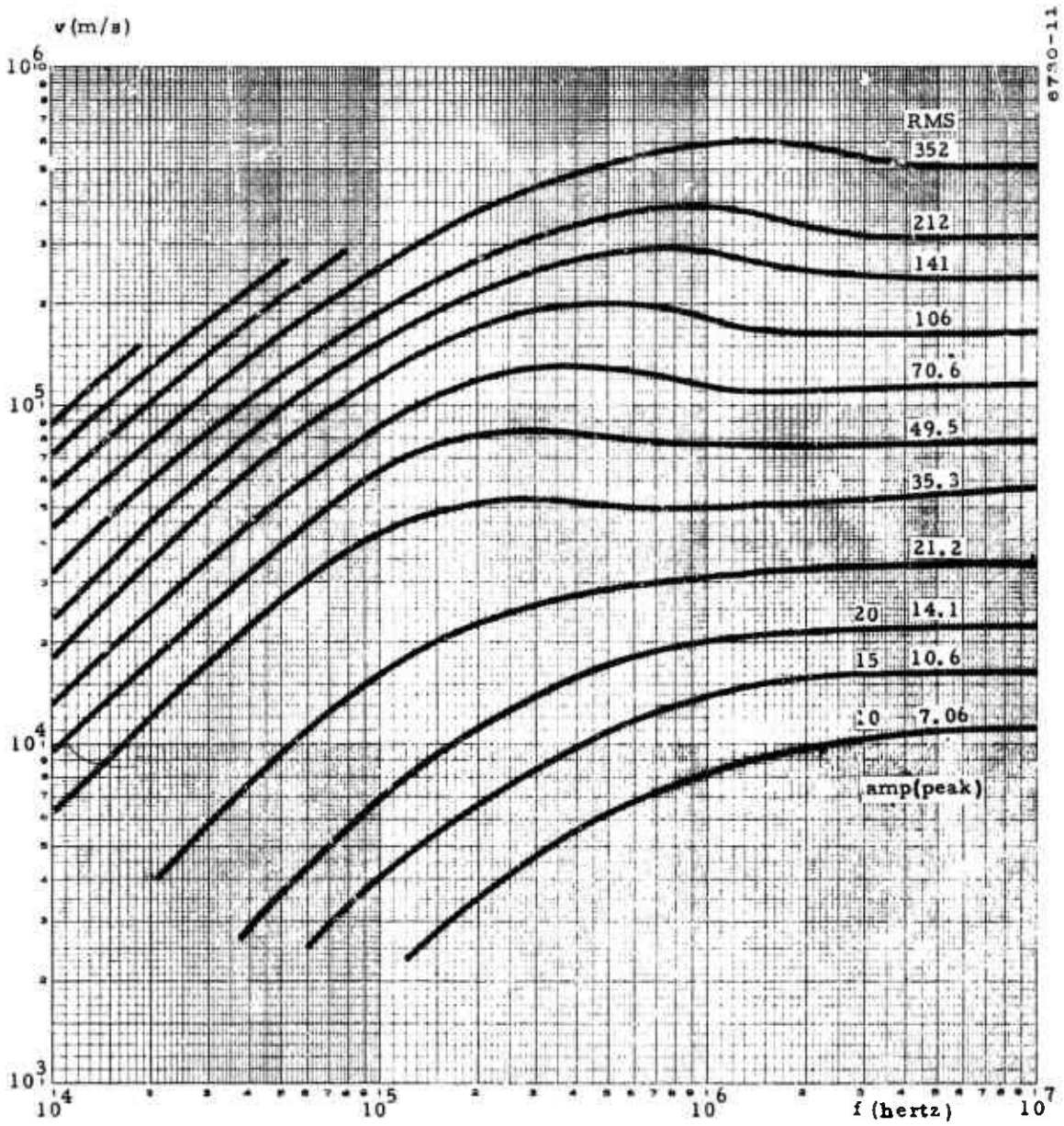

Figure 2-11. Current vs Terminal Velocity and Frequency (T = 1.0 newton)

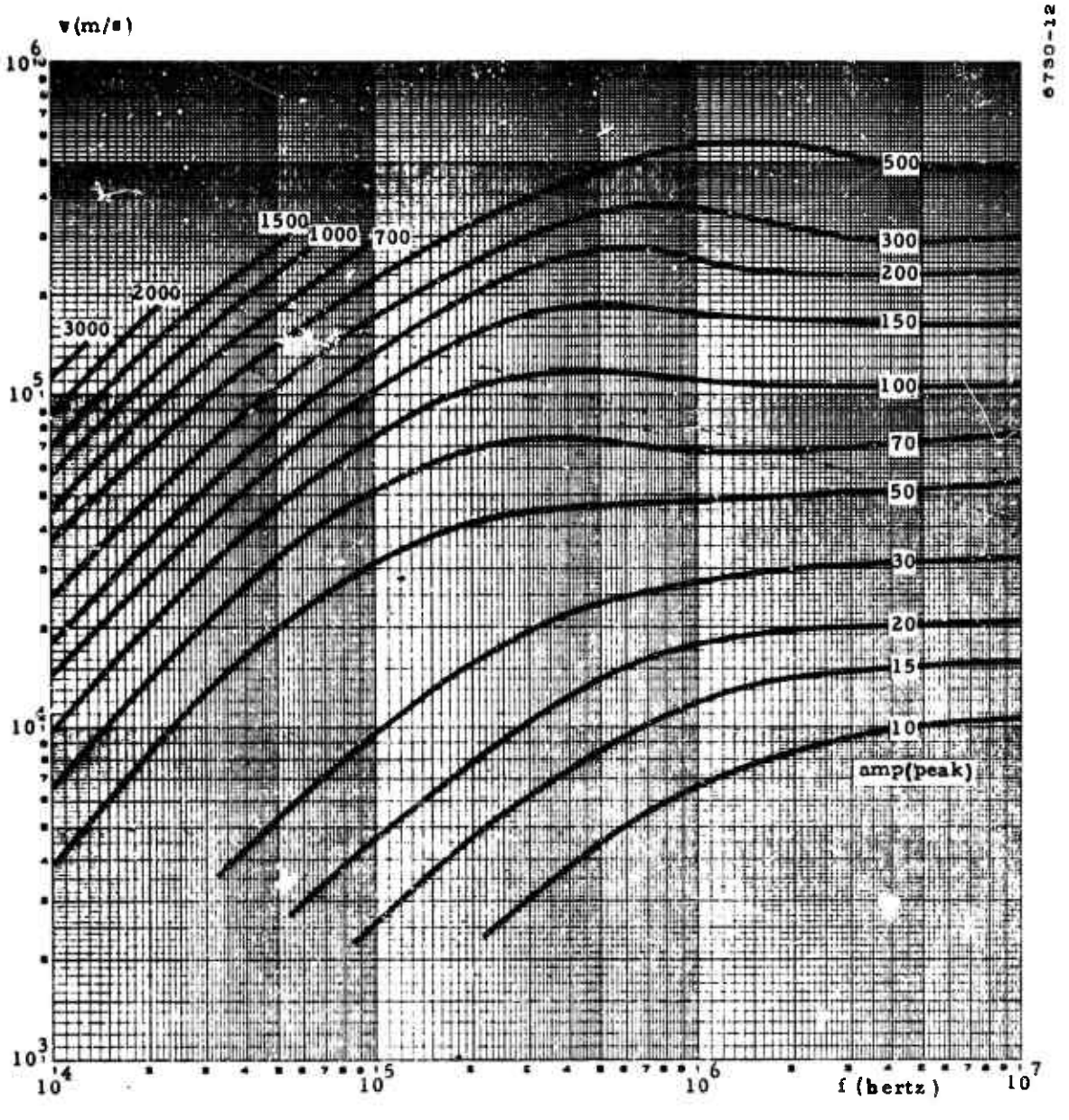

Figure 2-12. Current vs Terminal Velocity and Frequency (T = 1.5 newton)

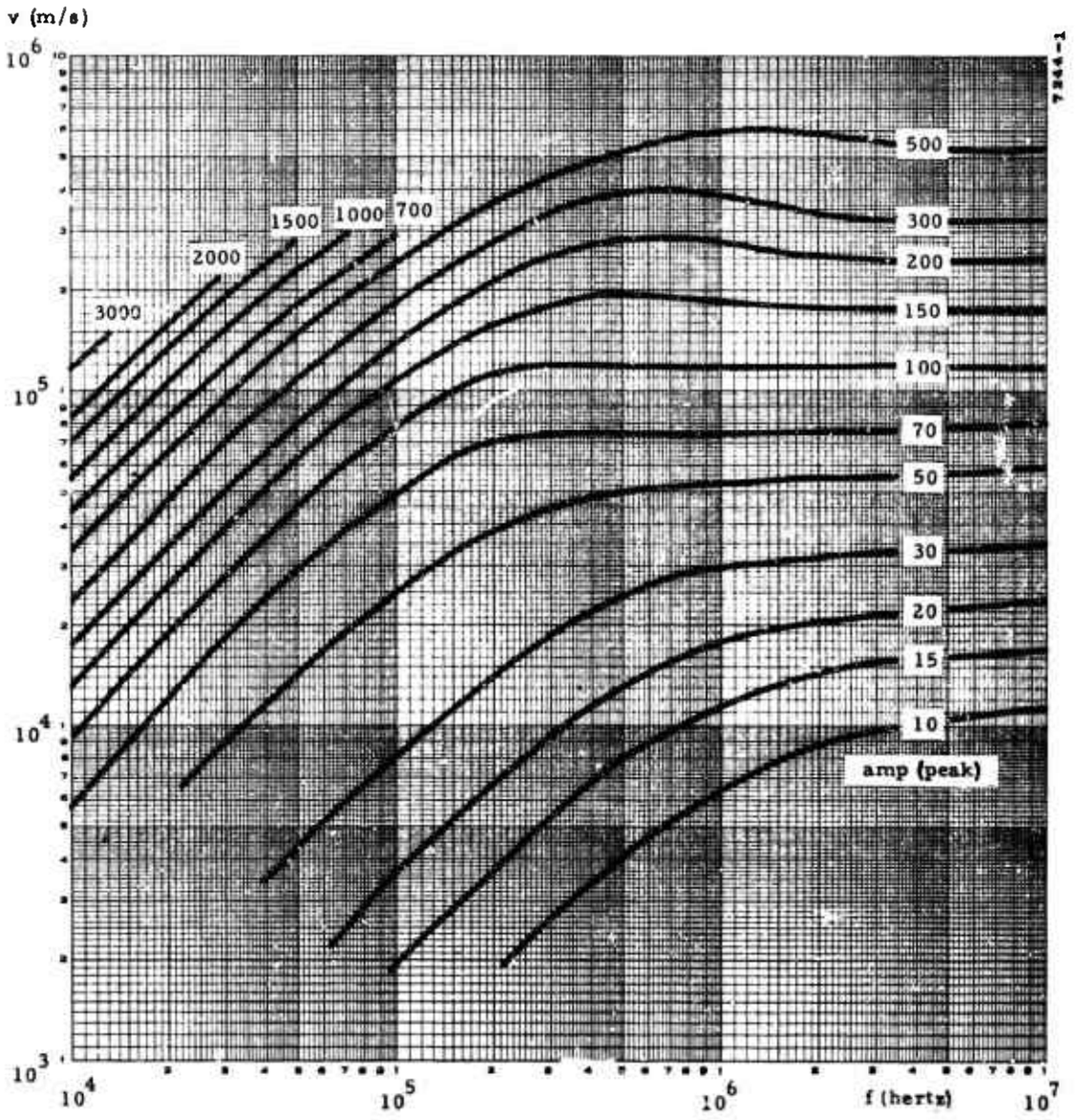

Figure 2-13. Current vs Terminal Velocity and Frequency (T = 2.0 newton)

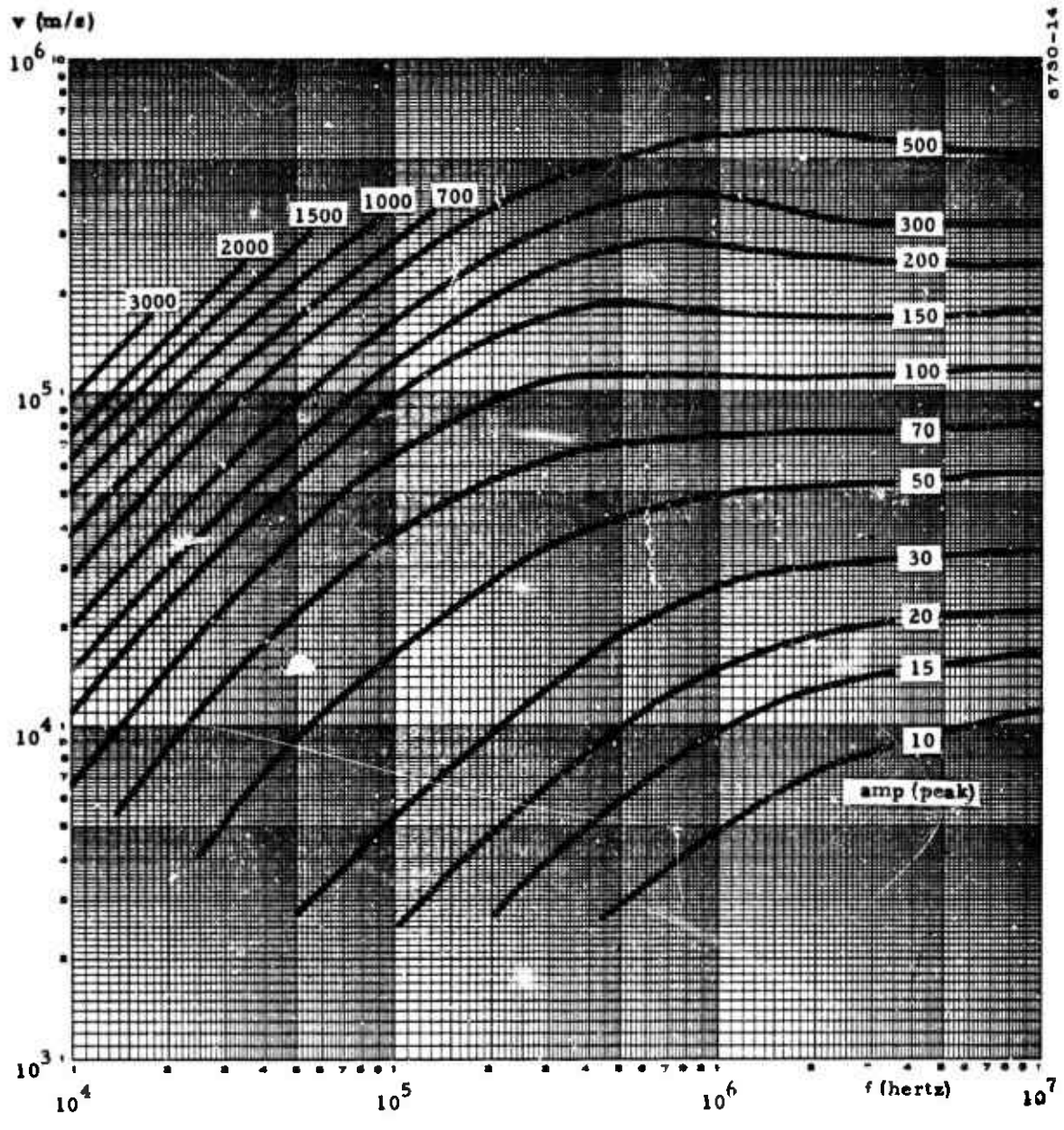

Figure 2-14. Current vs Terminal Velocity and Frequency (T = 3.0 newton)

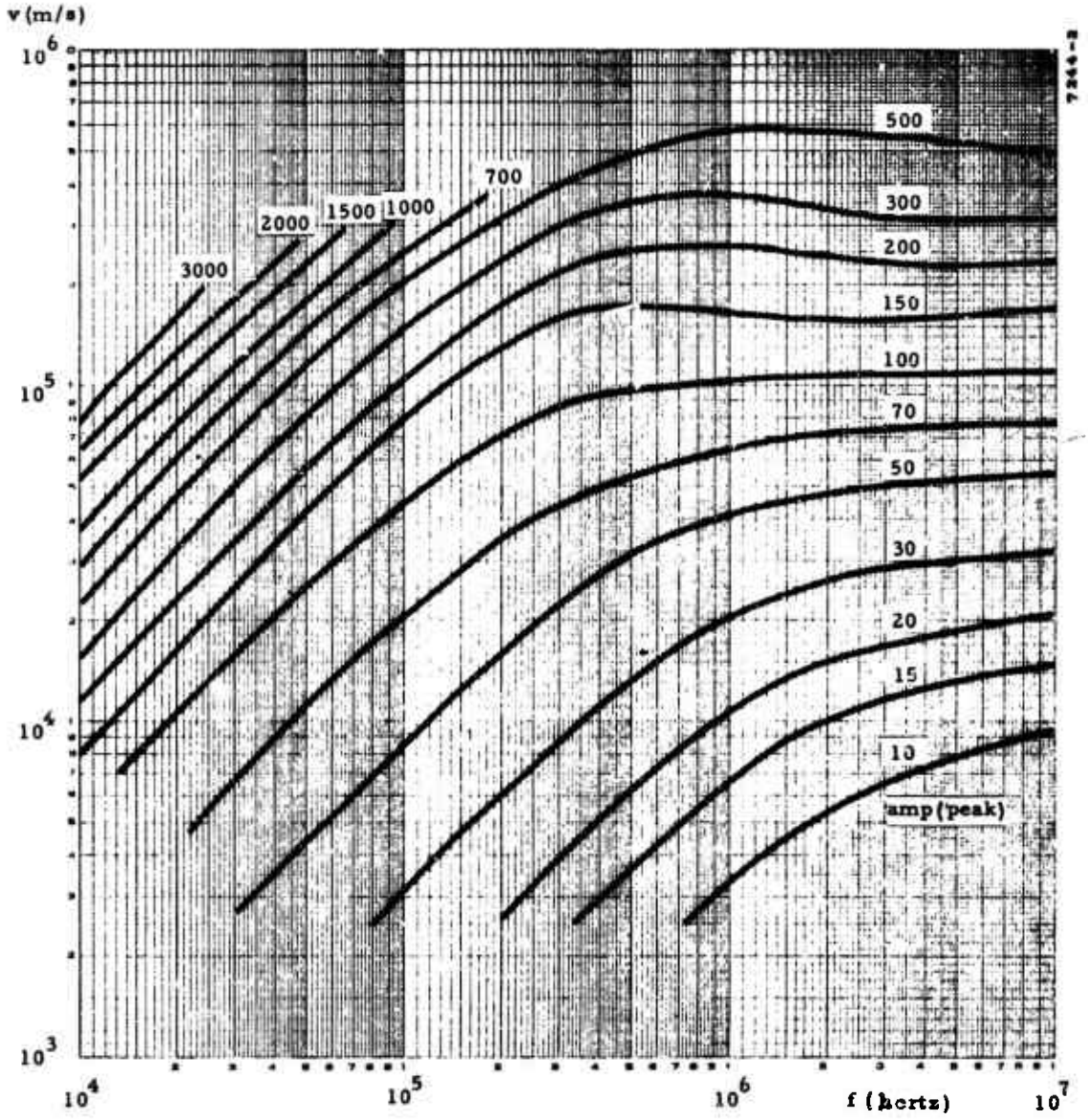

Figure 2-15. Current vs Terminal Velocity and Frequency (T = 5.0 newton)

The power dissipated in the coil by the I^2R losses can be computed if the value of the coil resistance is known as a function of frequency. This was computed by the standard skin-resistance formula in which the resistivity of the copper was taken to be 2.5 times that at room temperature in accordance with the experimental results of section 5.2. The total resistance of a coil having the dimensions shown in the analog plots of Figures 2-1 and 2-2, built of copper tube 1/8" in diameter and operated at 550°C is given by

$$R = 0.229\sqrt{f}$$

where f is the frequency of operation in Megahertz. The power dissipated is therefore

$$W = \frac{R}{2} I_c^2 = 0.1145\sqrt{f}\, I_o^2$$

where I_o is the peak coil current in amperes. Using this and the performance curves of Figure 2-4 through 2-15 a new set of curves was derived, showing power loss in the coil as a function of frequency, exhaust velocity and thrust. These are presented in Figure 2-16 through 2-27. The series of figures from Figure 2-28 through 2-35 is the same information in which lines of constant power are plotted in a thrust-velocity plane for a series of frequencies ranging from 30 Kilohertz to 1 megahertz. These graphs illustrate the predicted performance of the thrustor at constant frequency. From these it is possible to compare the dissipated power, W_r, with the beam power $W_k = Tv/2$ where T is the thrust and v the exhaust velocity. We define an ohmic efficiency η_r by

$$\eta_r = \frac{W_k}{W_r + W_k}.$$

The series of figures from Figure 2-36 through 2-43 show lines of constant η_r in the thrust-velocity plane for a series of frequencies. There are several points to be noted concerning this last set of curves.

a. The efficiency η_r is calculated on the basis of a coil assumed to be operating at a constant temperature of 550°C. Because of the dependence of resisitivity on temperature the coil will be cooler

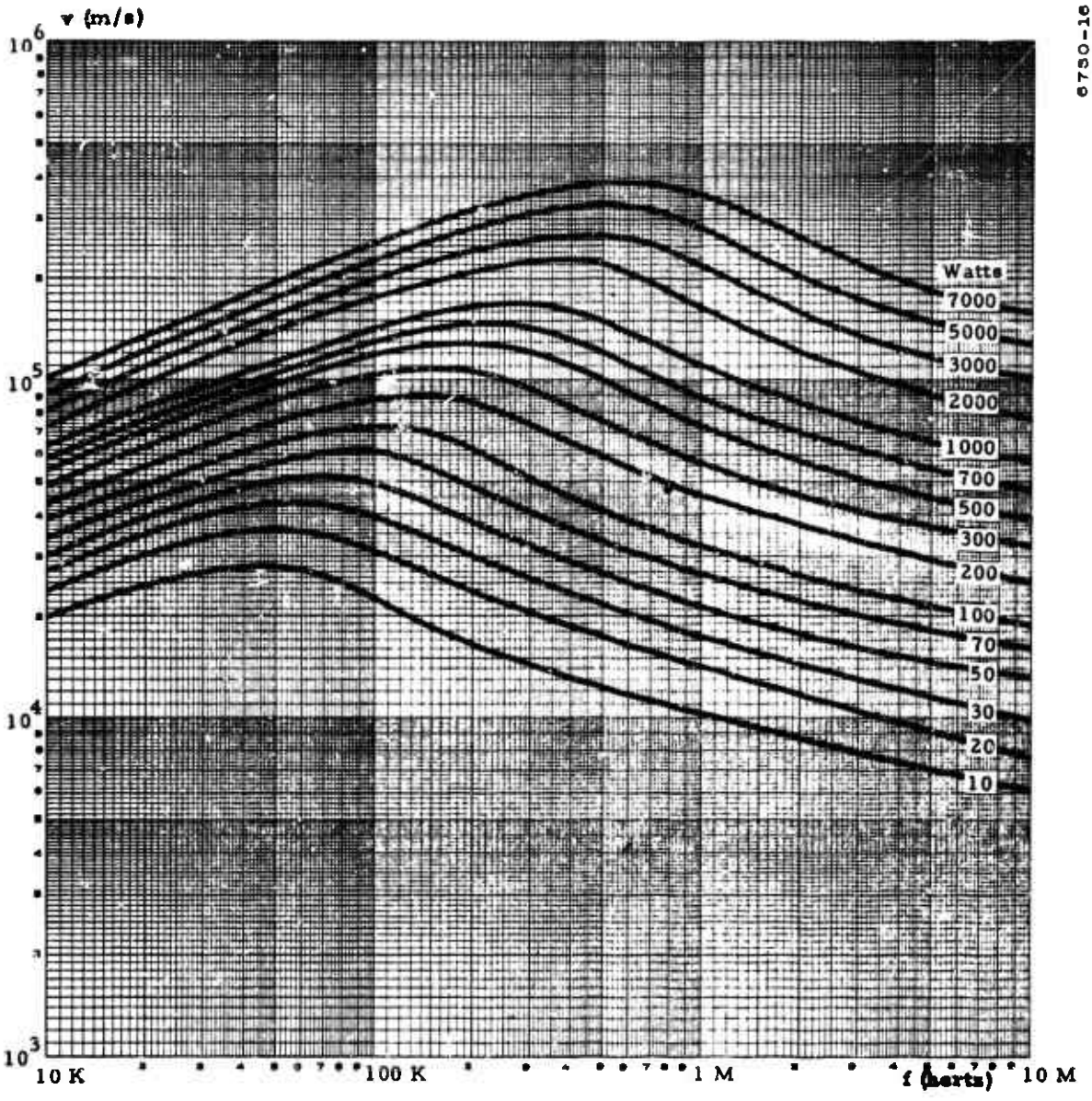

Figure 2-16. Ohmic Power Loss in Coil vs Terminal Velocity and Frequency (Zero Loading: T = 0)

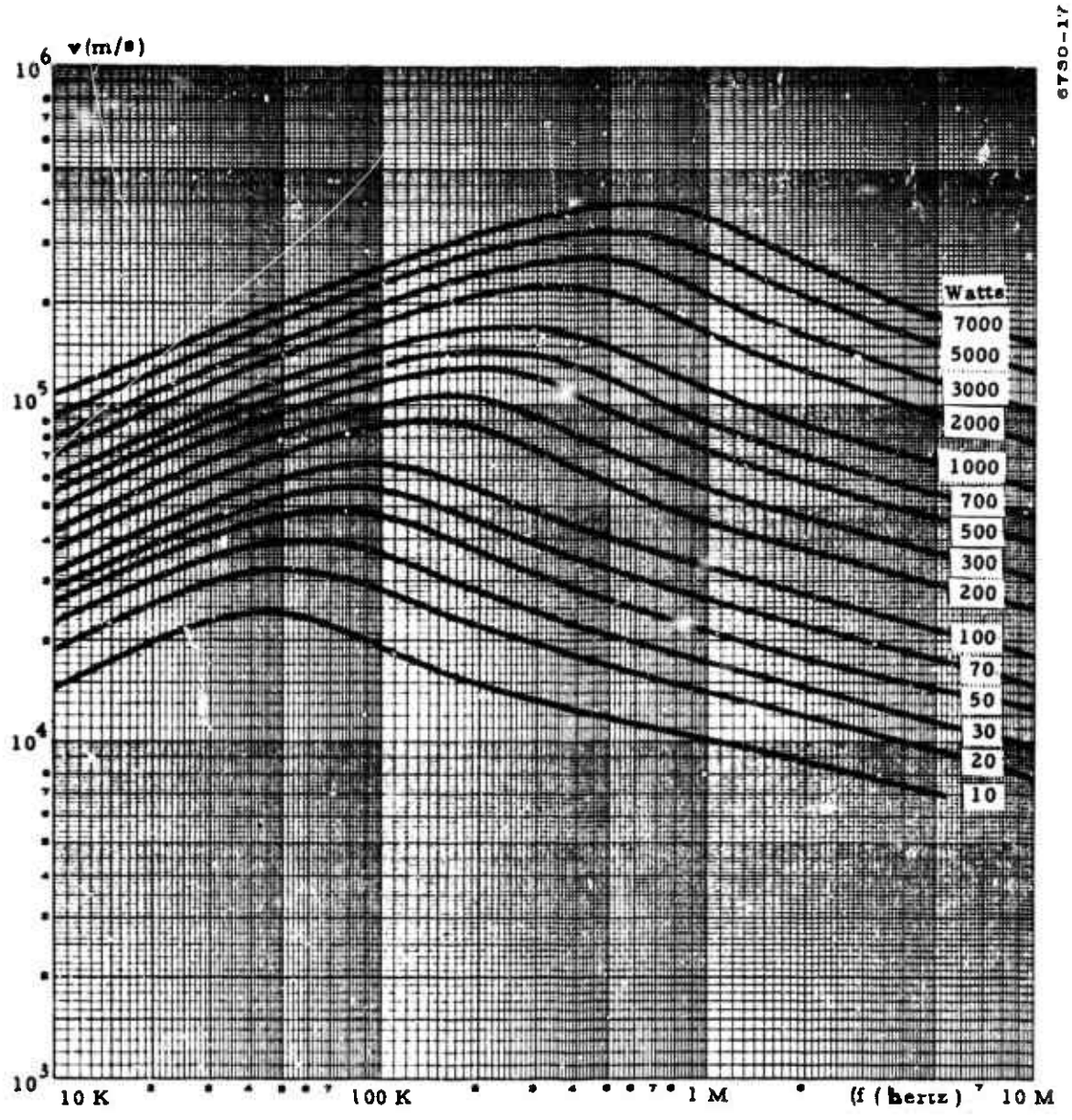

Figure 2-17. Ohmic Power Loss in Coil vs Terminal Velocity and Frequency (T = 0.05 newton)

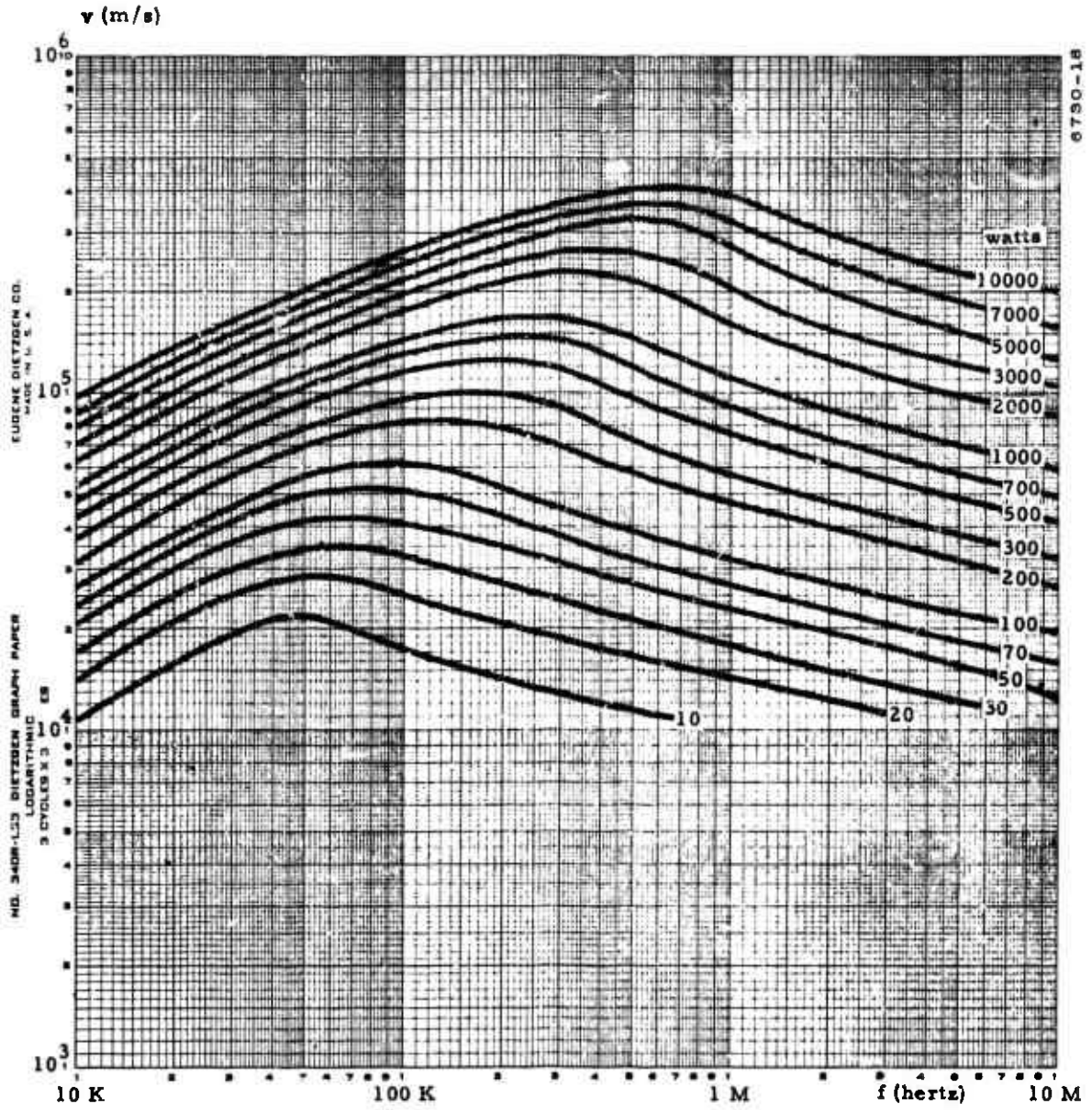

Figure 2-18. Ohmic Power Loss in Coil vs Terminal Velocity and Frequency (T = 0.1 newton)

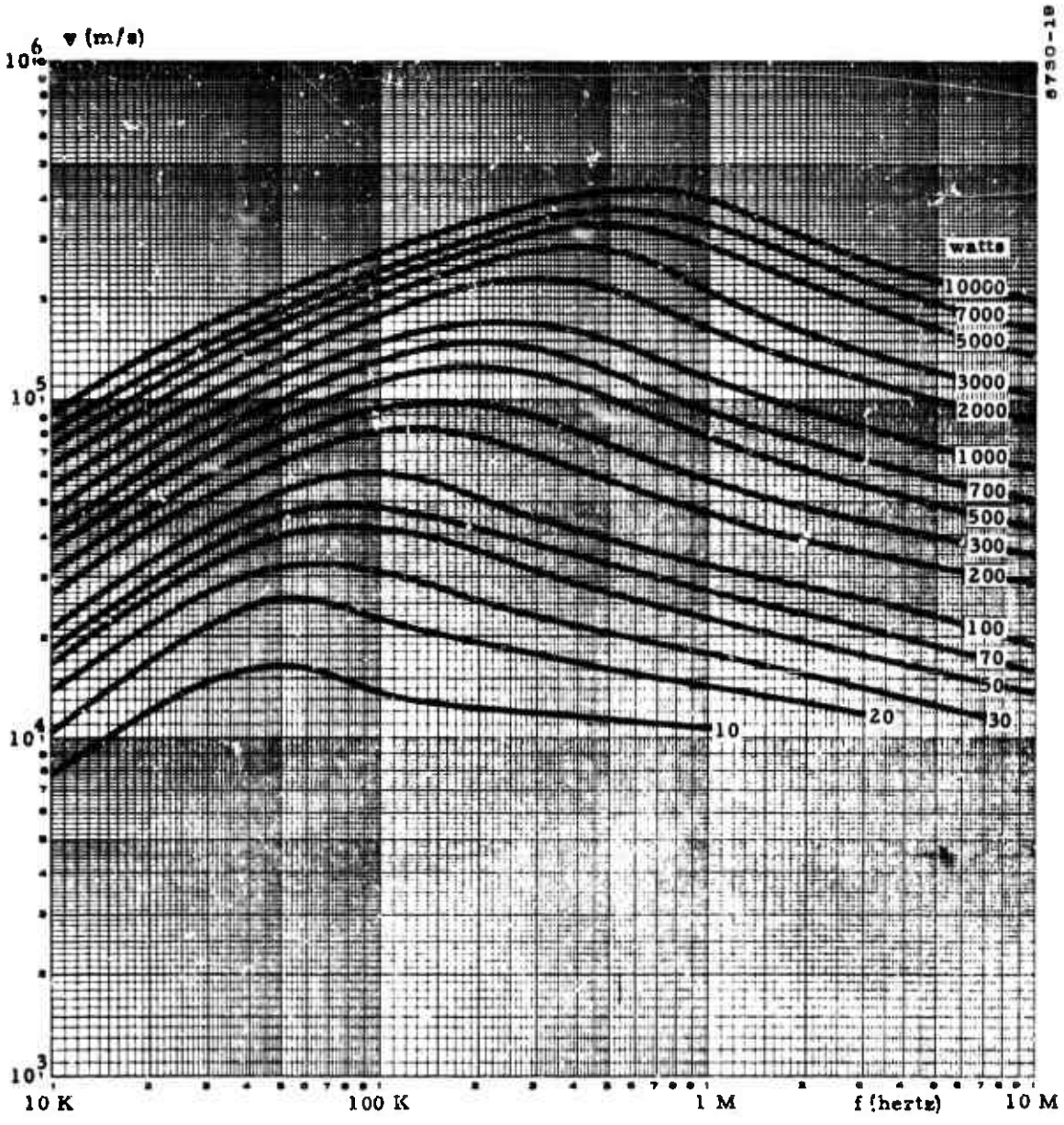

Figure 2-19. Ohmic Power Loss in Coil vs Terminal Velocity and Frequency (T = 0.2 newton)

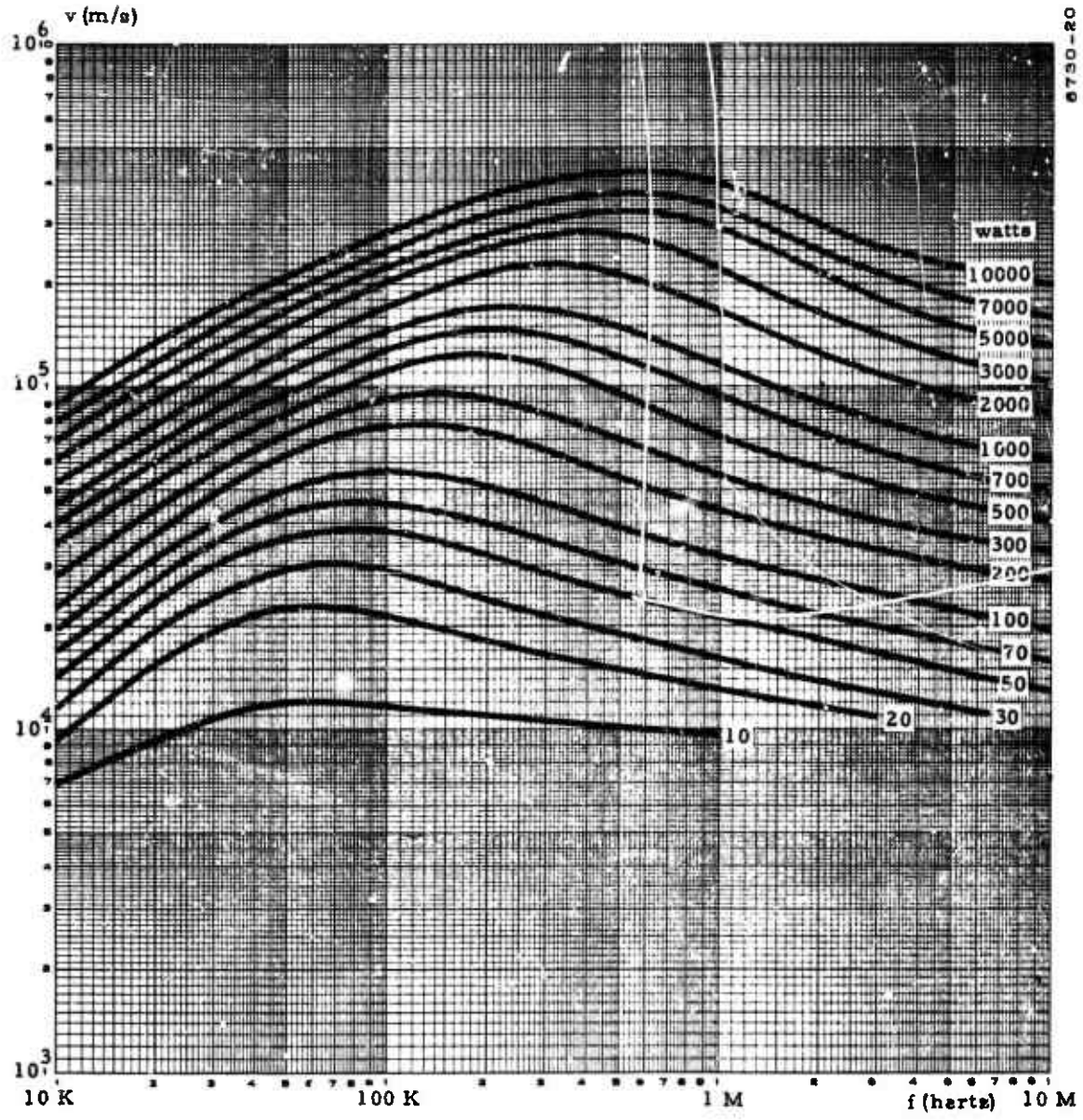

Figure 2-20. Ohmic Power Loss in Coil vs Terminal Velocity and Frequency (T = 0.3 newton)

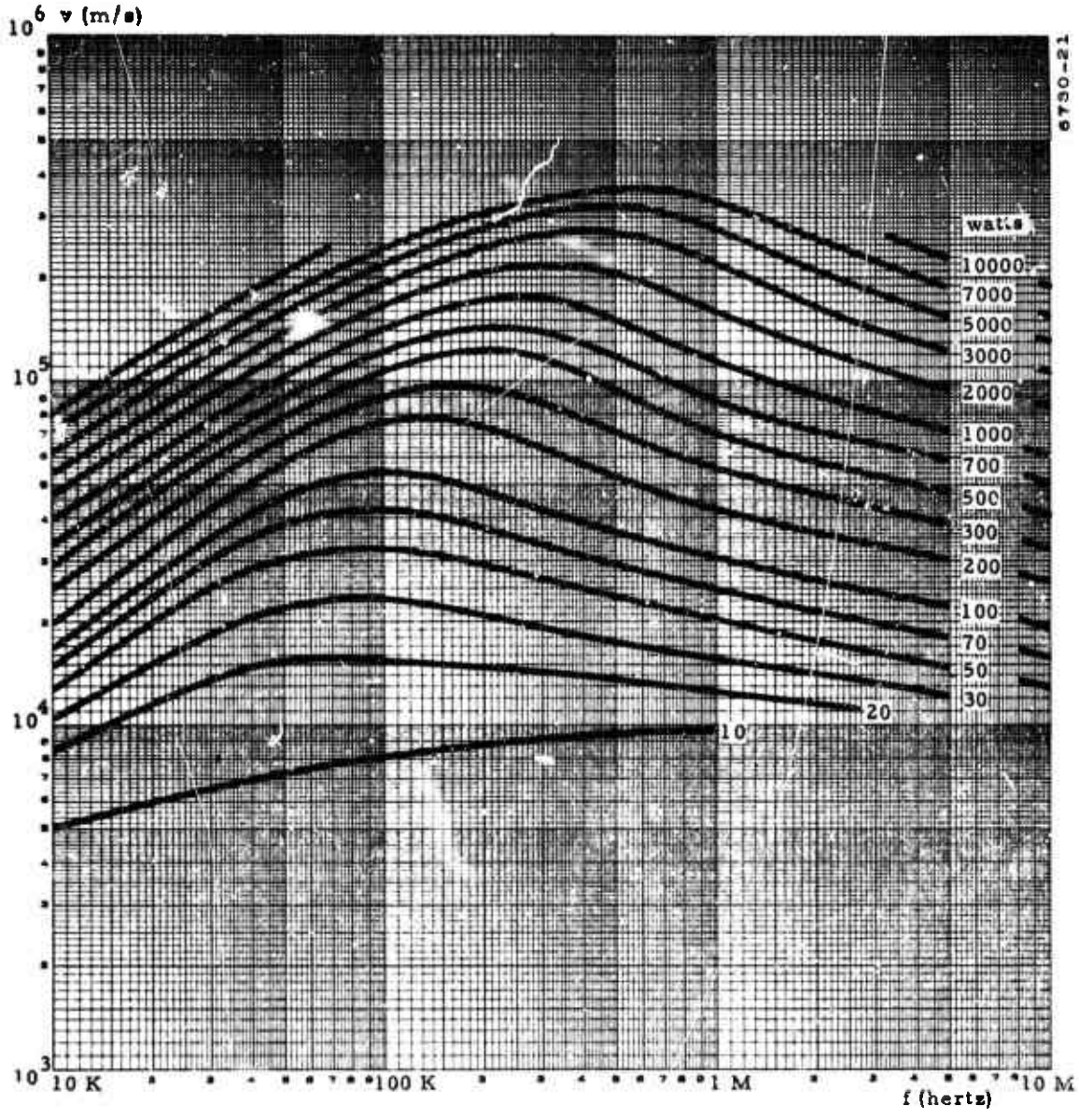

Figure 2-21. Ohmic Power Loss in Coil vs Terminal Velocity and Frequency (T = 0.5 newton)

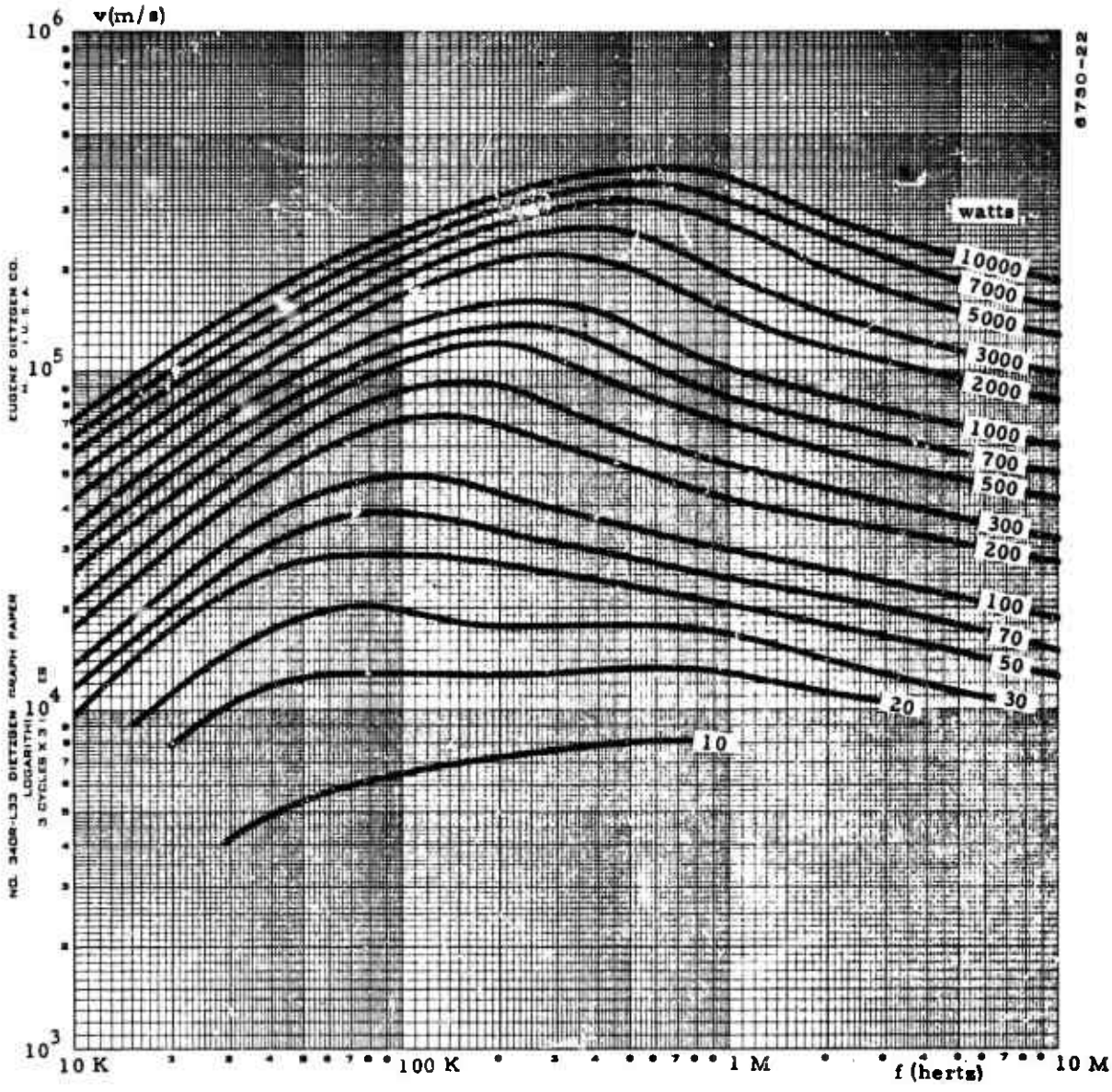

Figure 7-22. Ohmic Power Loss in Coil vs Terminal Velocity and Frequency (T = 0.7 newton)

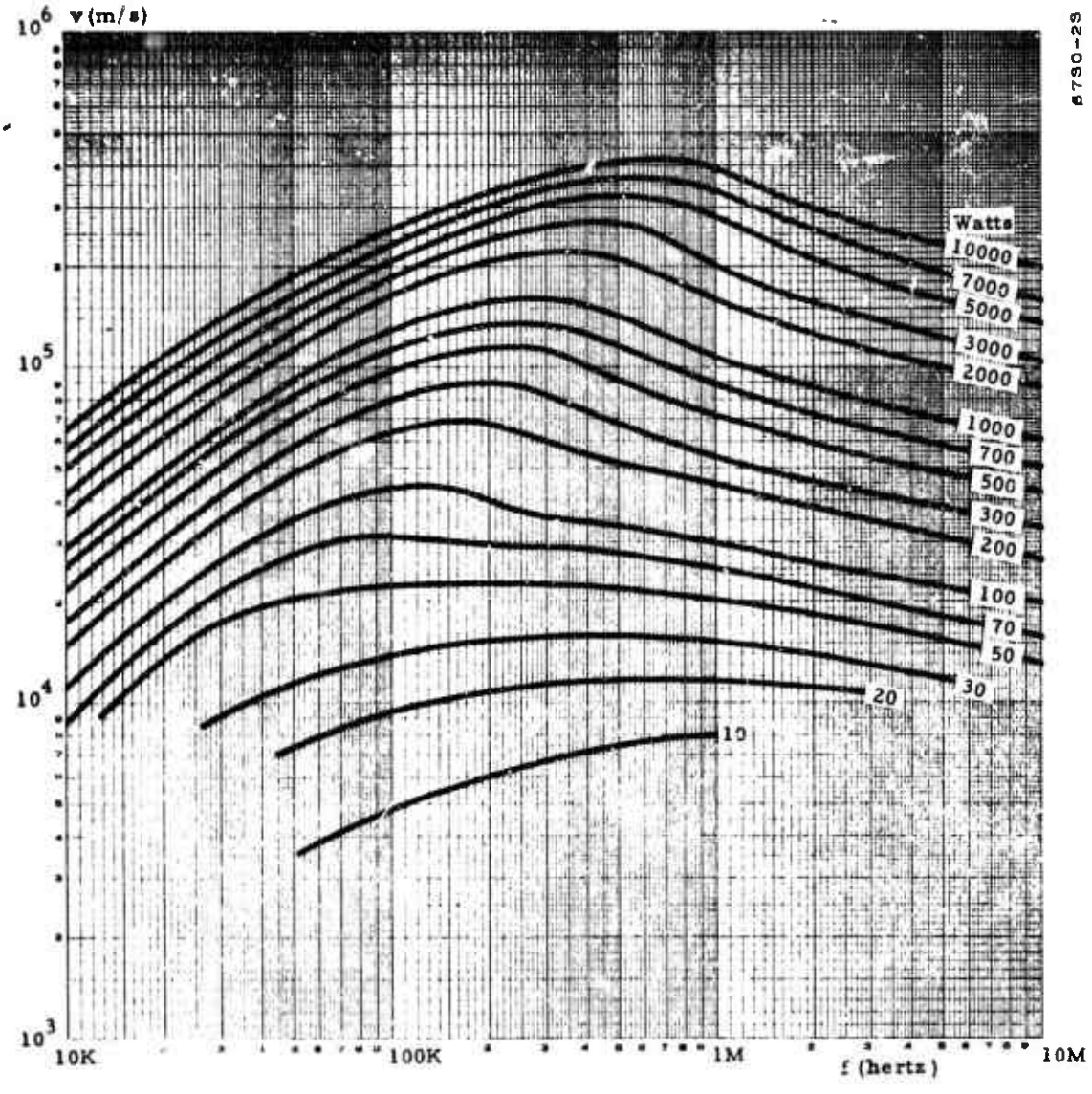

Figure 2-23. Ohmic Power Loss in Coil vs Terminal Velocity and Frequency (T = 1.0 newton)

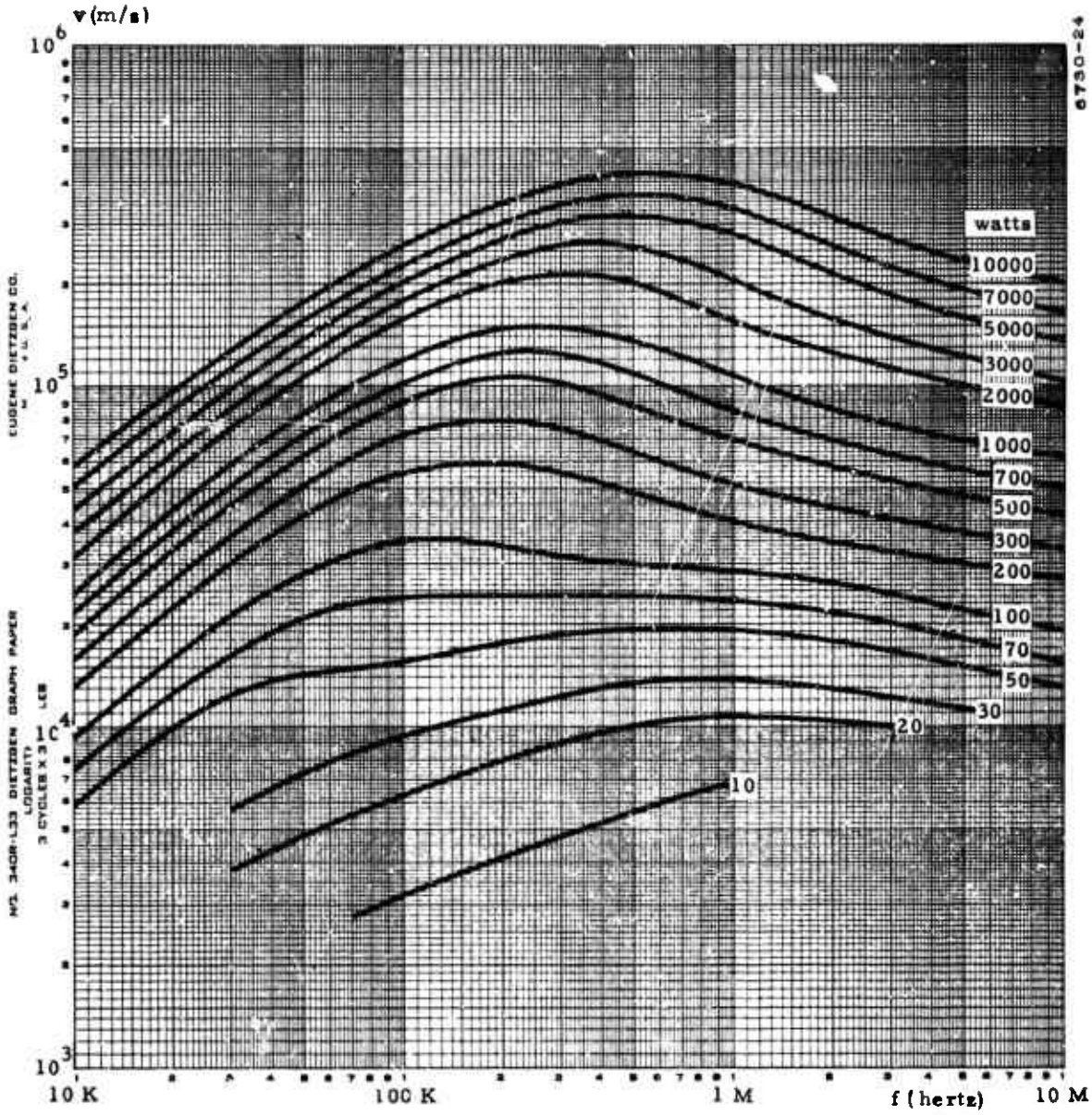

Figure 2-24. Ohmic Power Loss in Coil vs Terminal Velocity and Frequency ($T = 1.5$ newton)

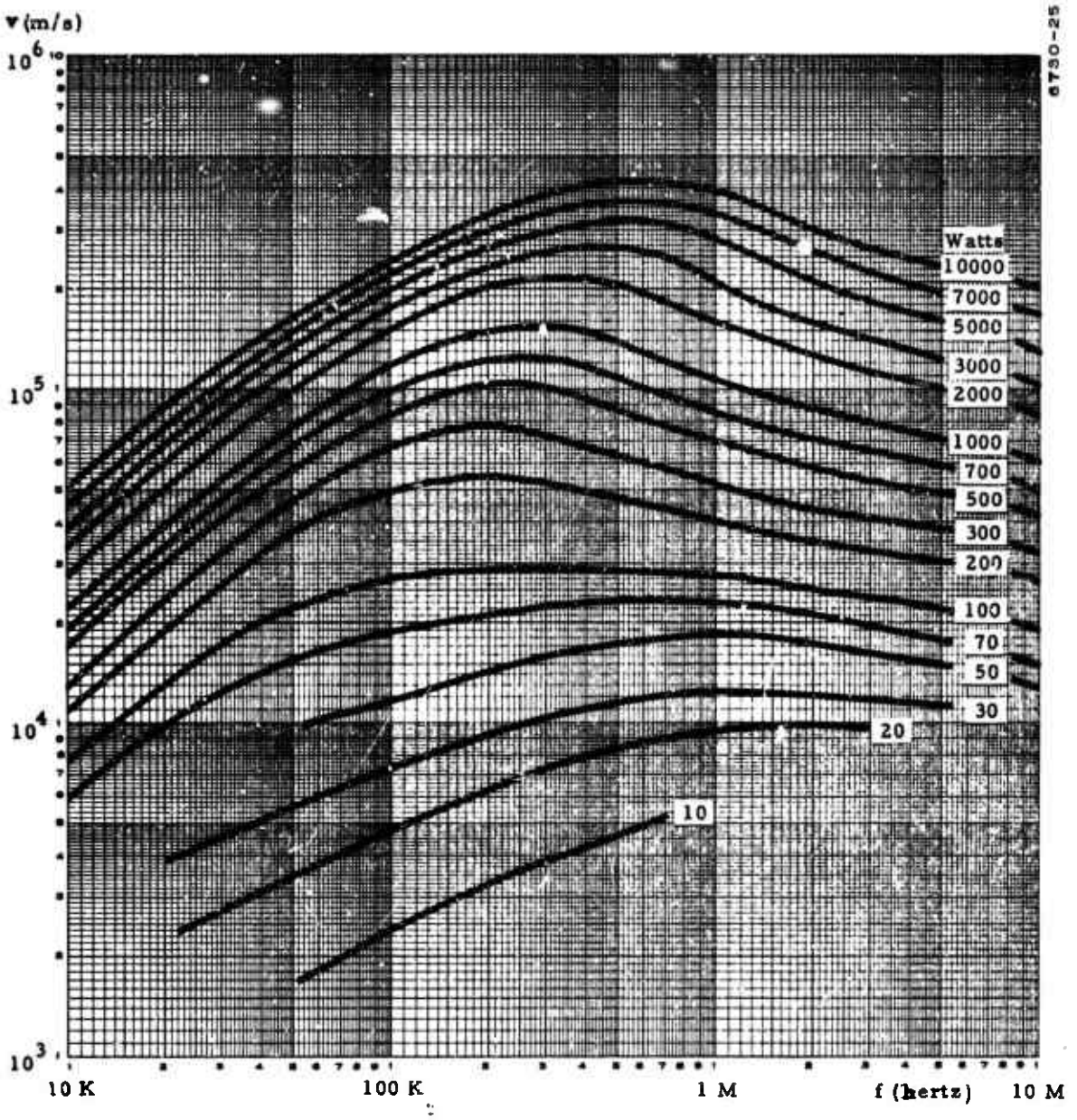

Figure 2-25. Ohmic Power Loss in Coil vs Terminal Velocity and Frequency (T = 2.0 newton)

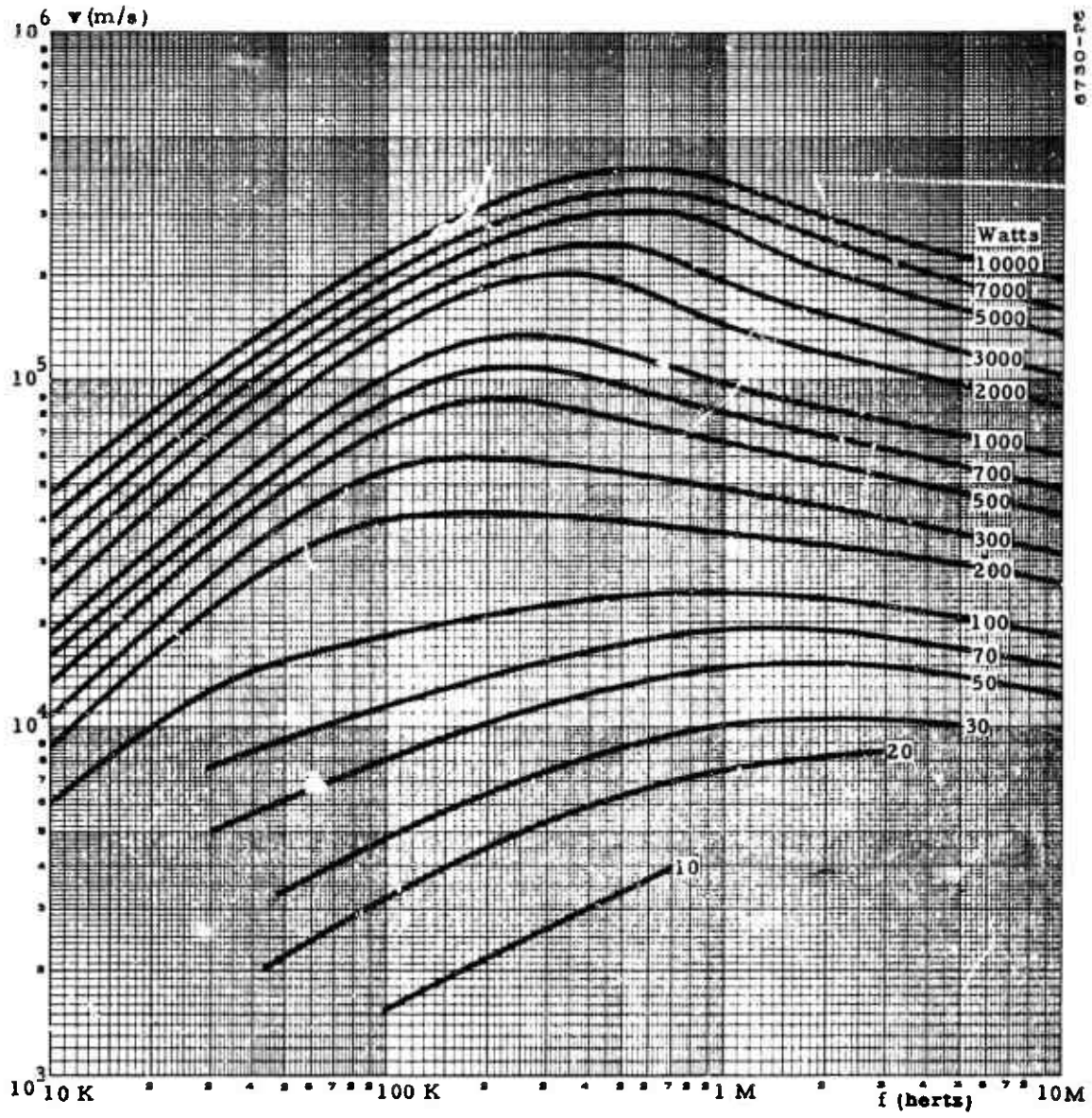

Figure 2-26. Ohmic Power Loss in Coil vs Terminal Velocity and Frequency (T = 3.0 newton)

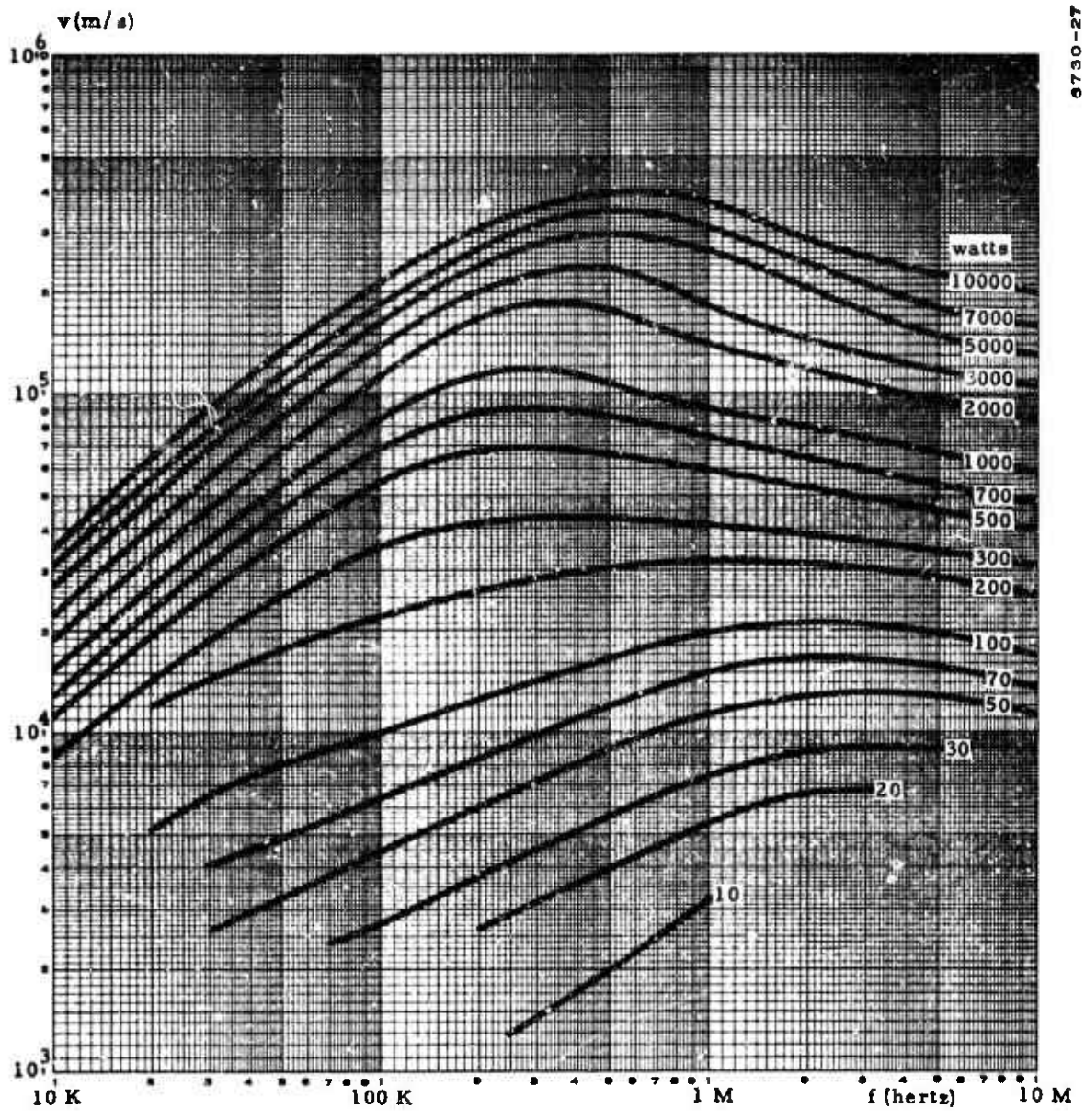

Figure 2-27. Ohmic Power Loss in Coil vs Terminal Velocity and Frequency (T = 5.0 newton)

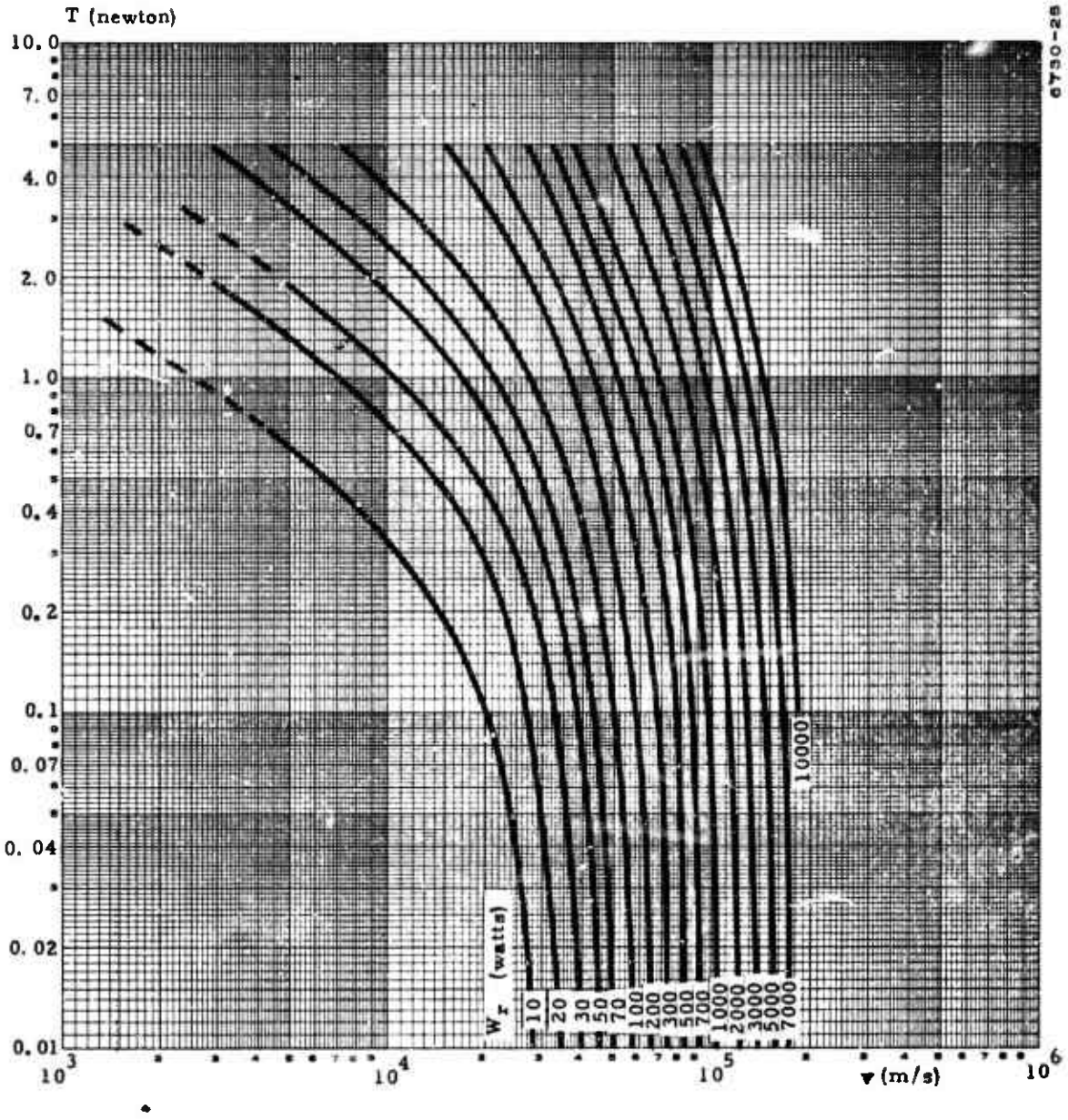

Figure 2-28. Ohmic Power Loss in Coil vs Thrust and Terminal Velocity at Constant Frequency (f = 30 Kilohertz)

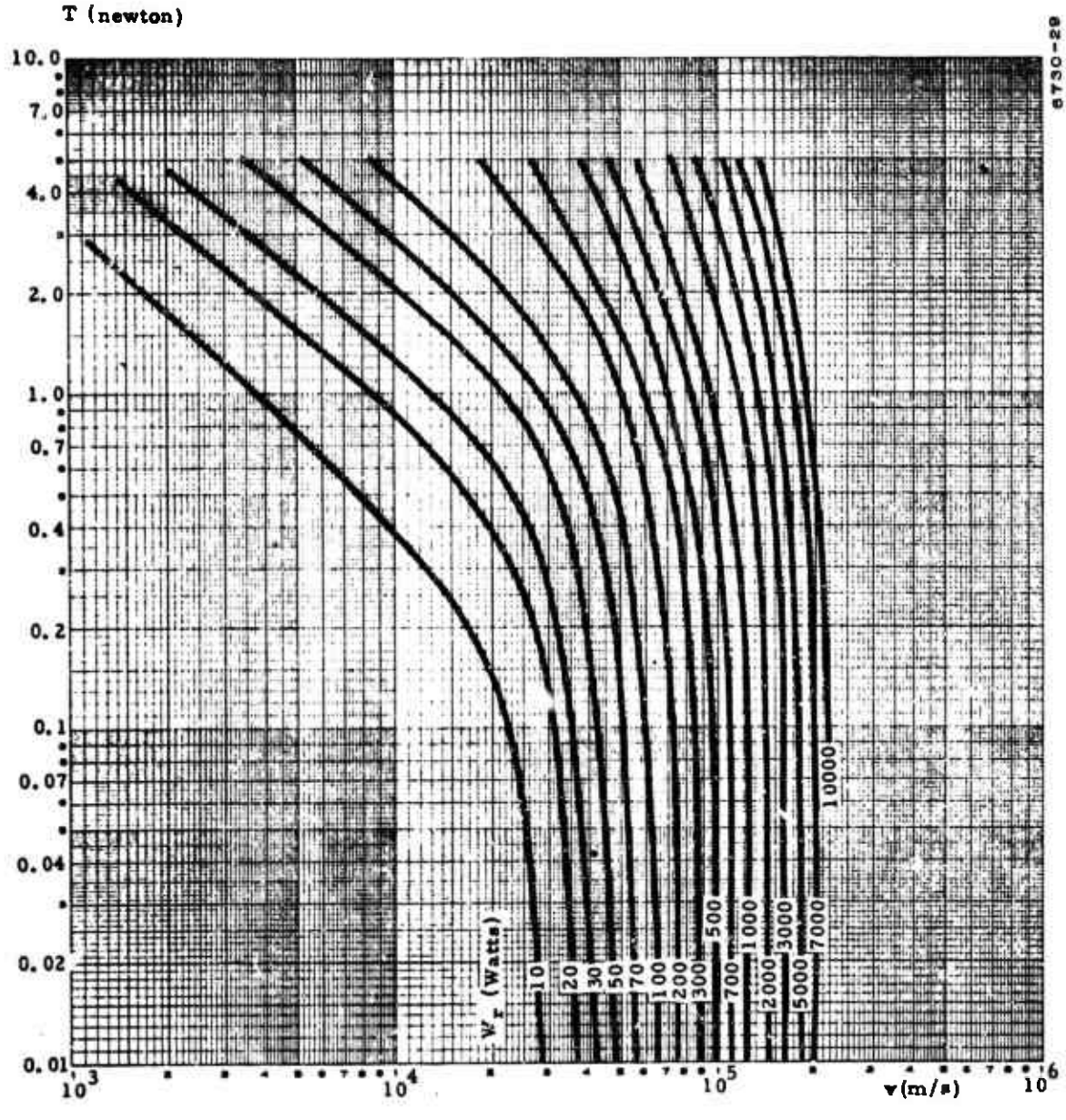

Figure 2-29. Ohmic Power Loss in Coil vs Thrust and Terminal Velocity at Constant Frequency (f = 50 Kilohertz)

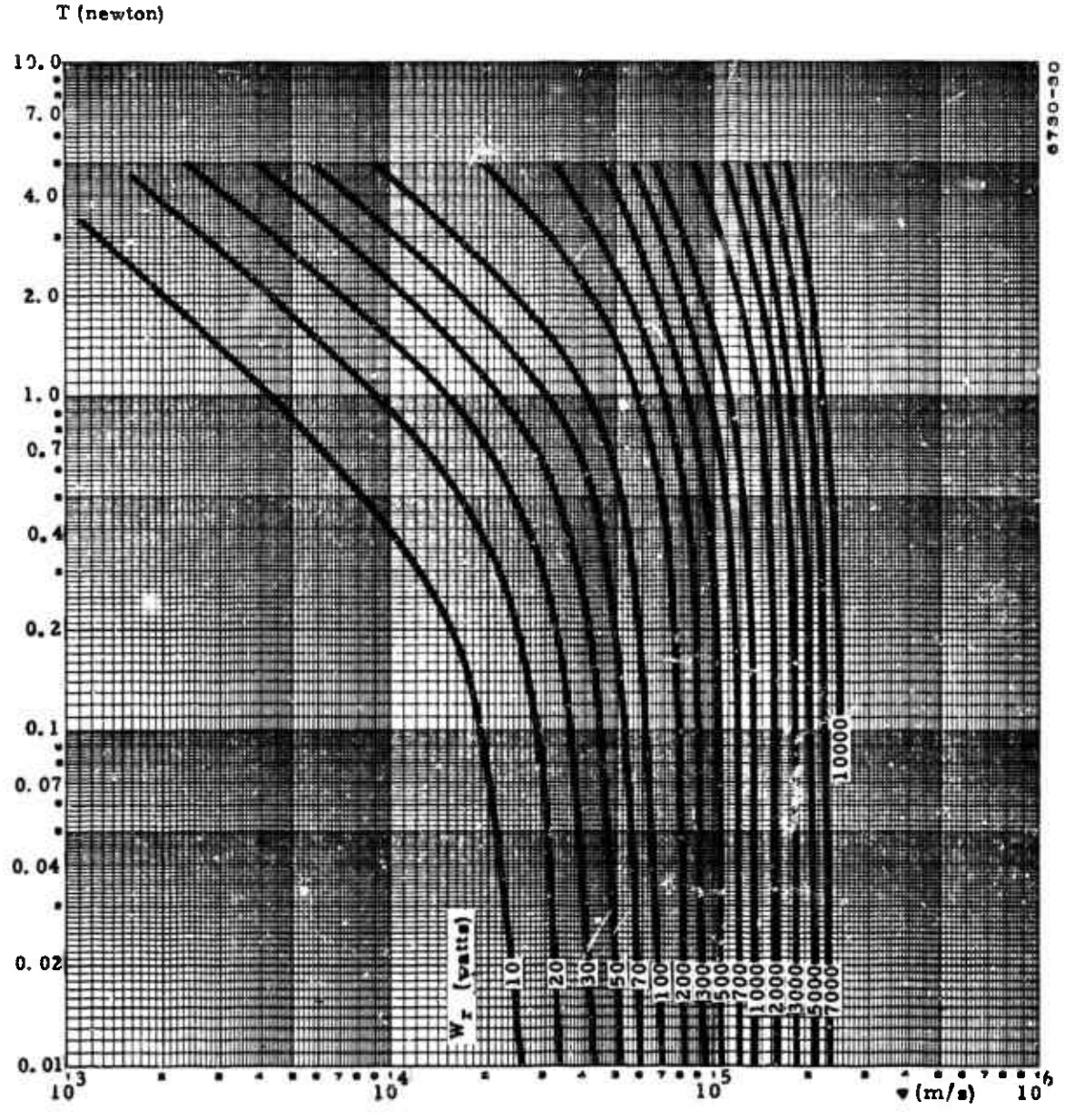

Figure 2-30. Ohmic Power Loss in Coil vs Thrust and Terminal Velocity at Constant Frequency (f = 100 Kilohertz)

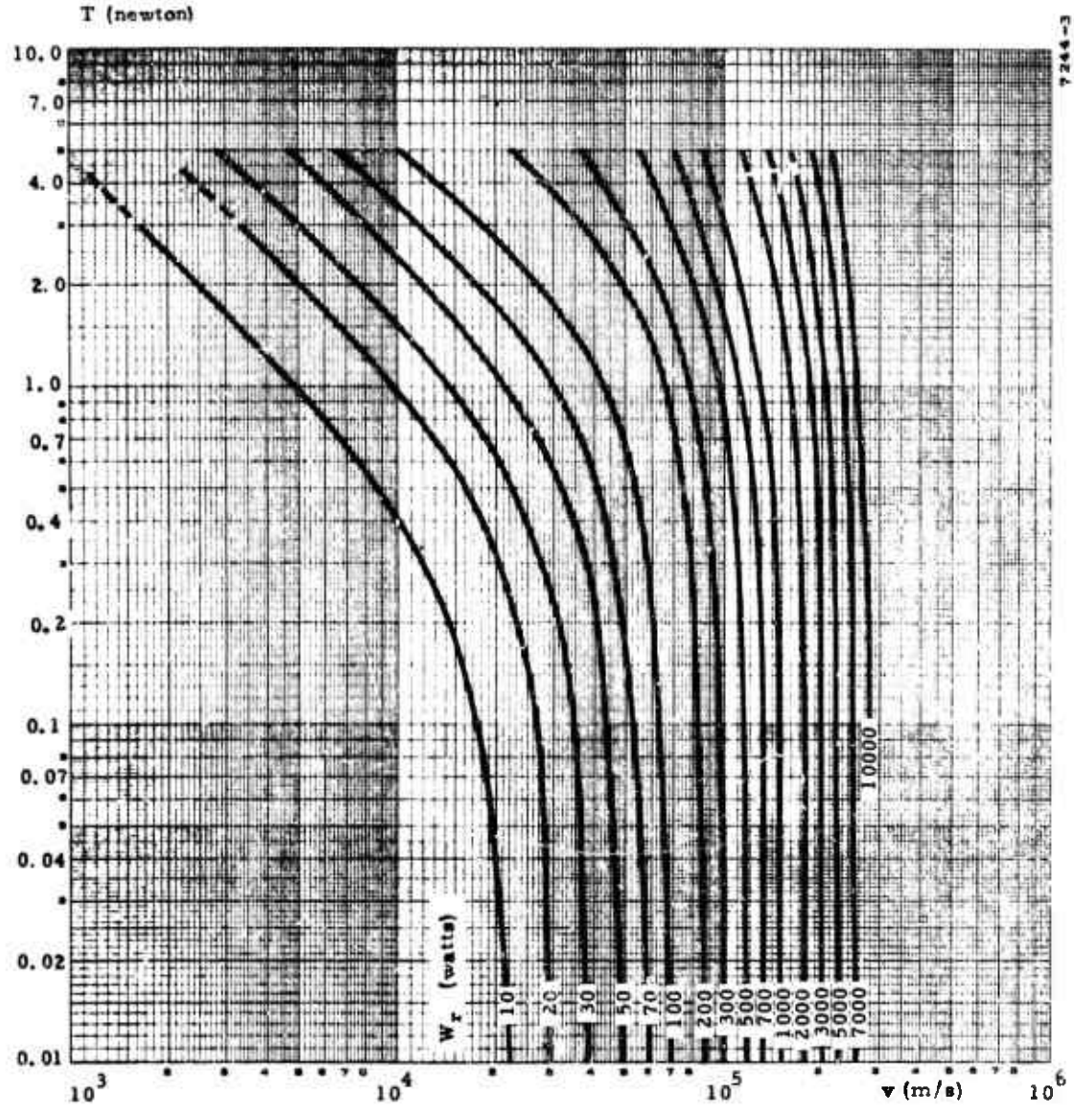

Figure 2-31. Ohmic Power Loss in Coil vs Thrust and Terminal Velocity at Constant Frequency (f = 240 Kilohertz)

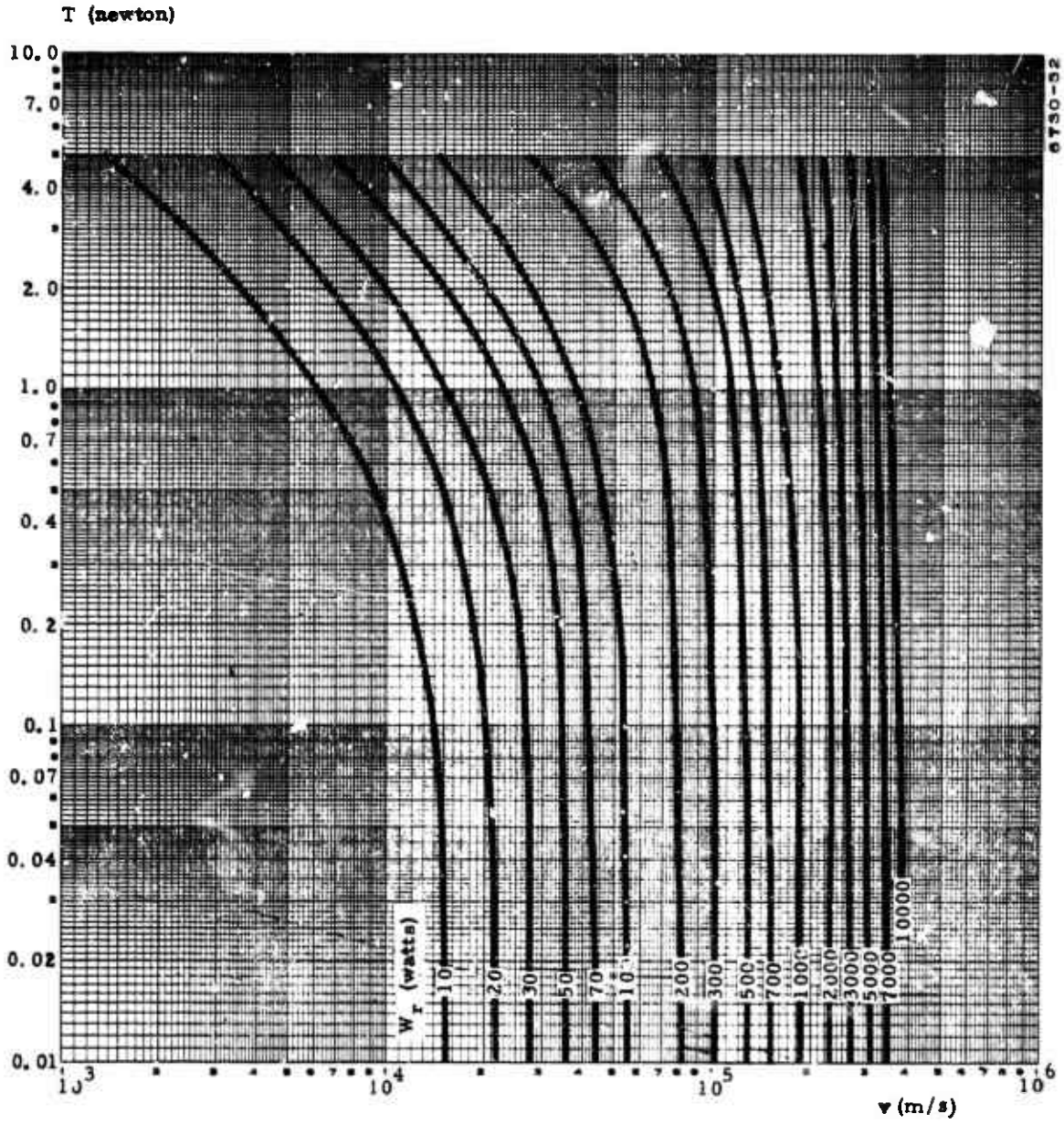

Figure 2-32. Ohmic Power Loss in Coil vs Thrust and Terminal Velocity at Constant Frequency (f = 300 Kilohertz)

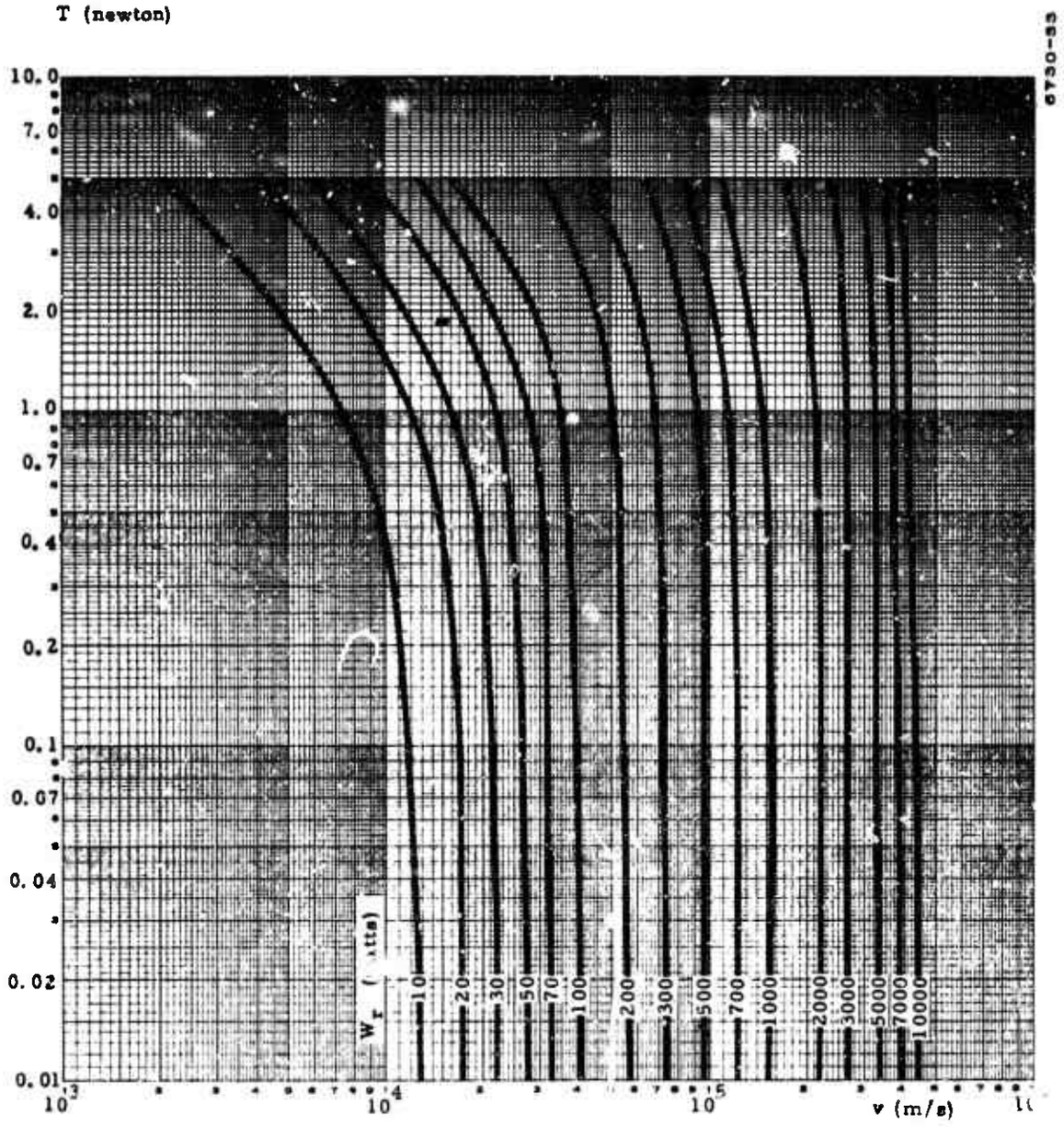

Figure 2-33. Ohmic Power Loss in Coil vs Thrust and Terminal Velocity at Constant Frequency (f = 500 Kilohertz)

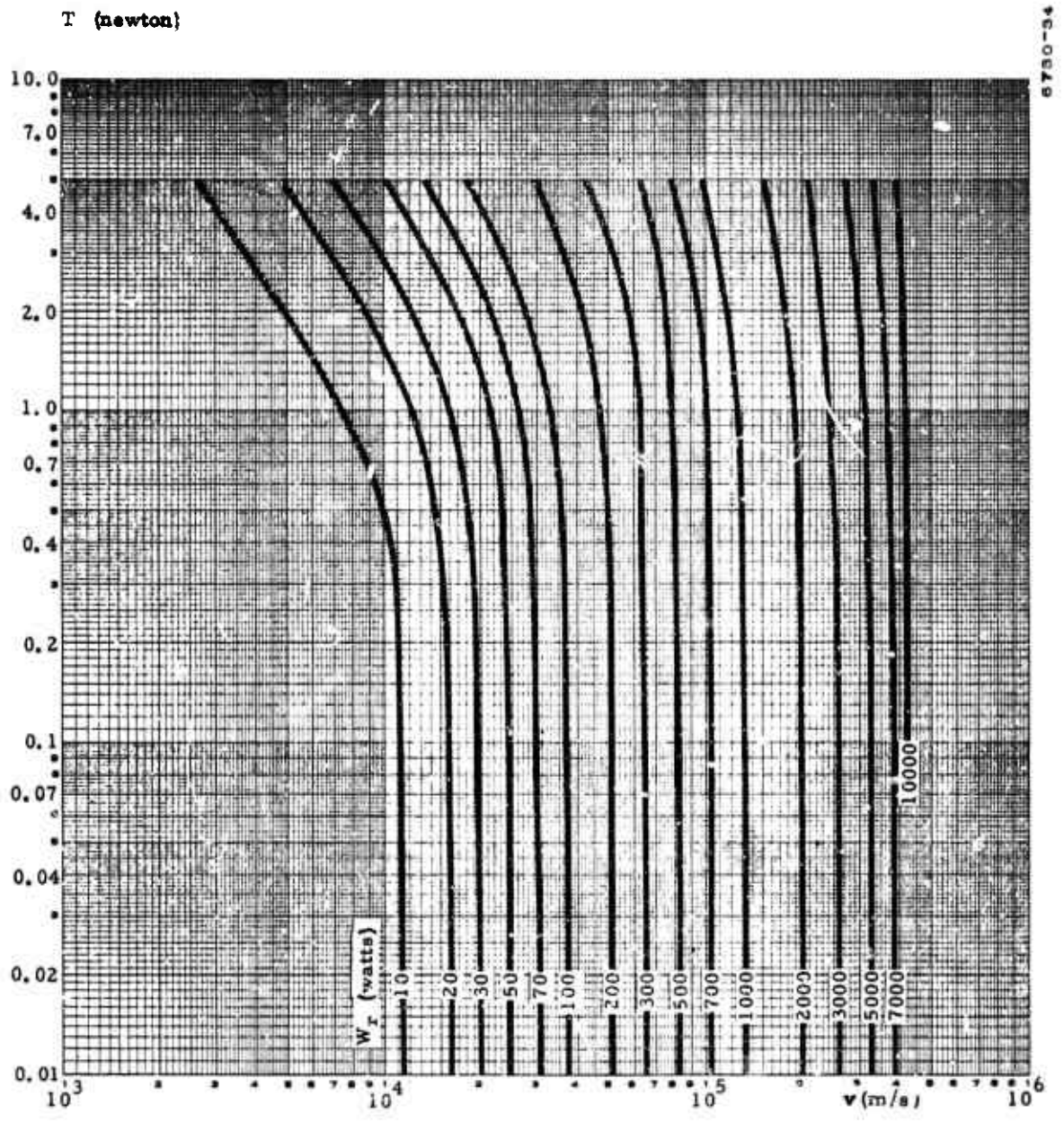

Figure 2-34. Ohmic Power Loss in Coil vs Thrust and Terminal Velocity at Constant Frequency (f = 700 Kilohertz)

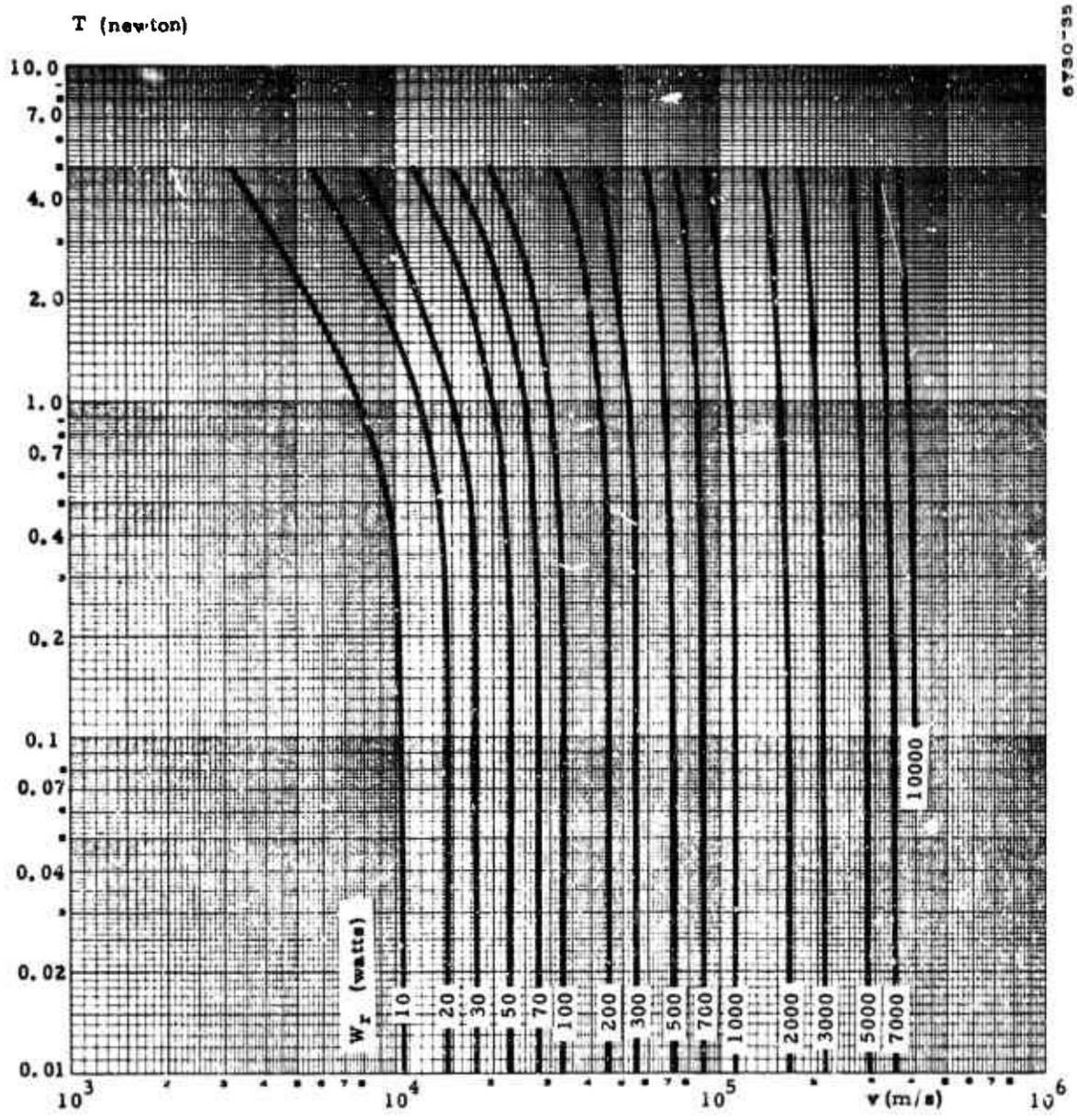

Figure 2-35. Ohmic Power Loss in Coil vs Thrust and Terminal Velocity at Constant Frequency (f = 1 Megahertz)

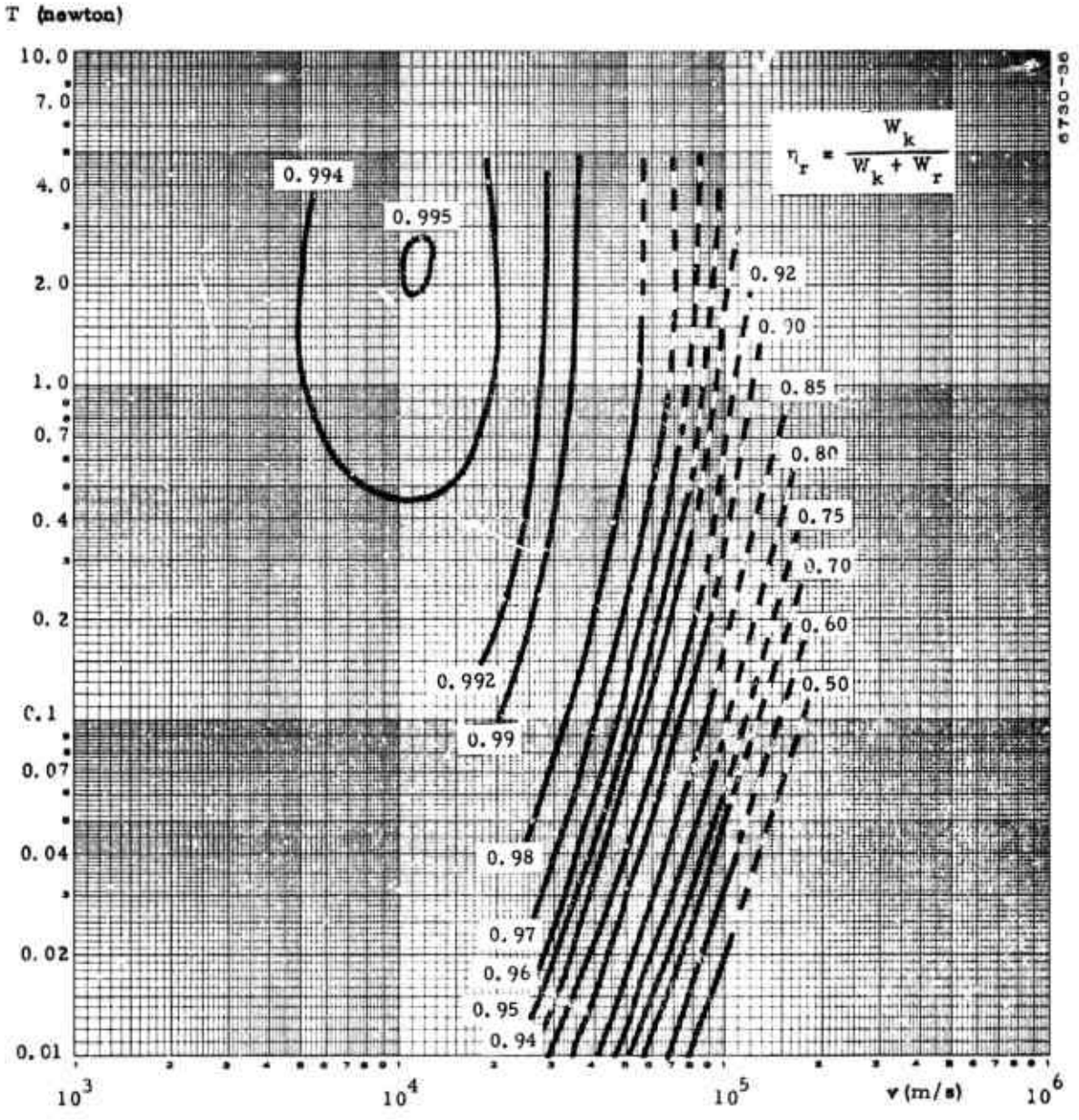

Figure 2-36. Ohmic Efficiency of Coil vs Thrust and Terminal Velocity at Constant Frequency (f = 30 Kilohertz)

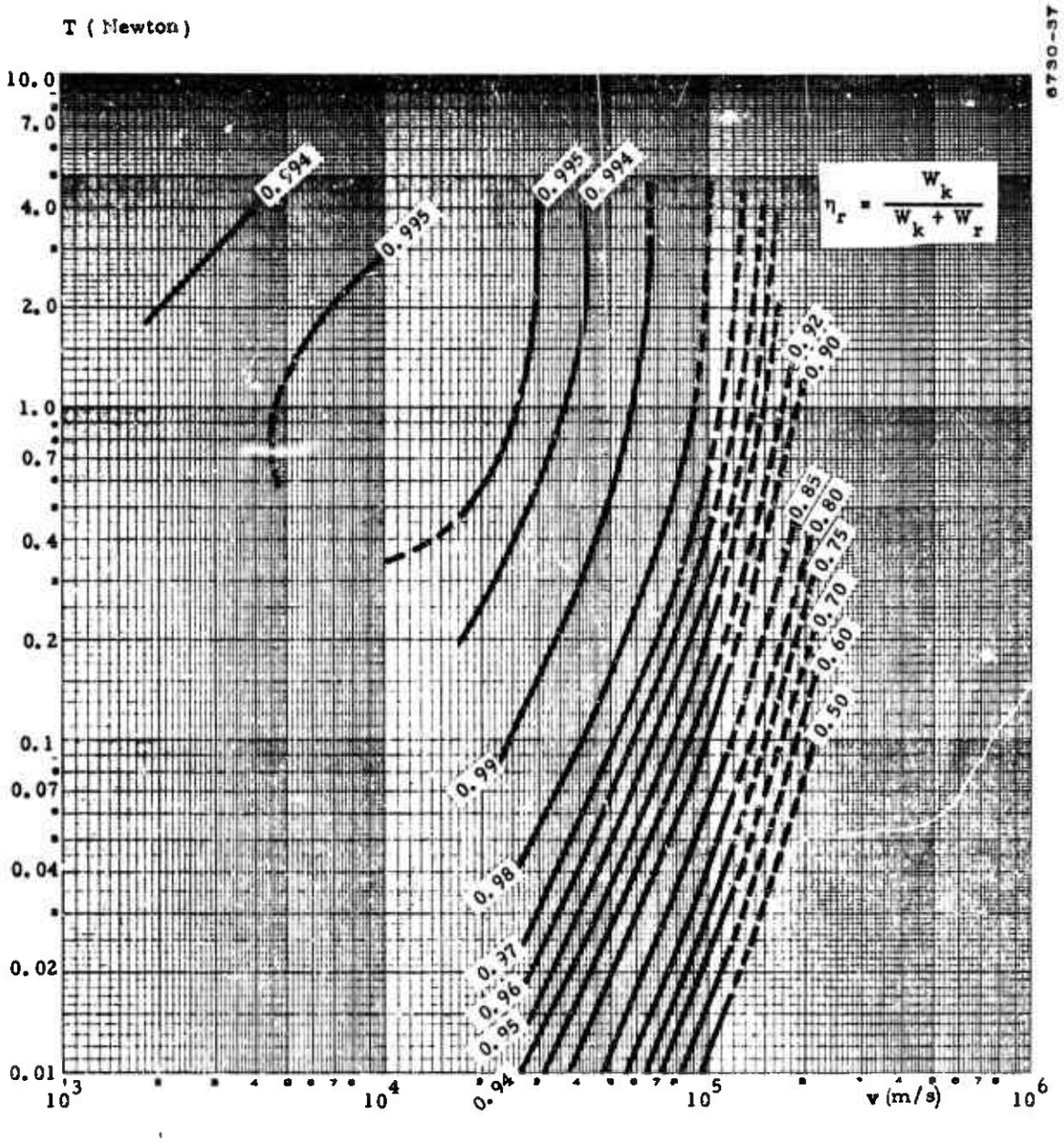

Figure 2-37. Ohmic Efficiency of Coil vs Thrust and Terminal Velocity at Constant Frequency (f = 50 Kilohertz)

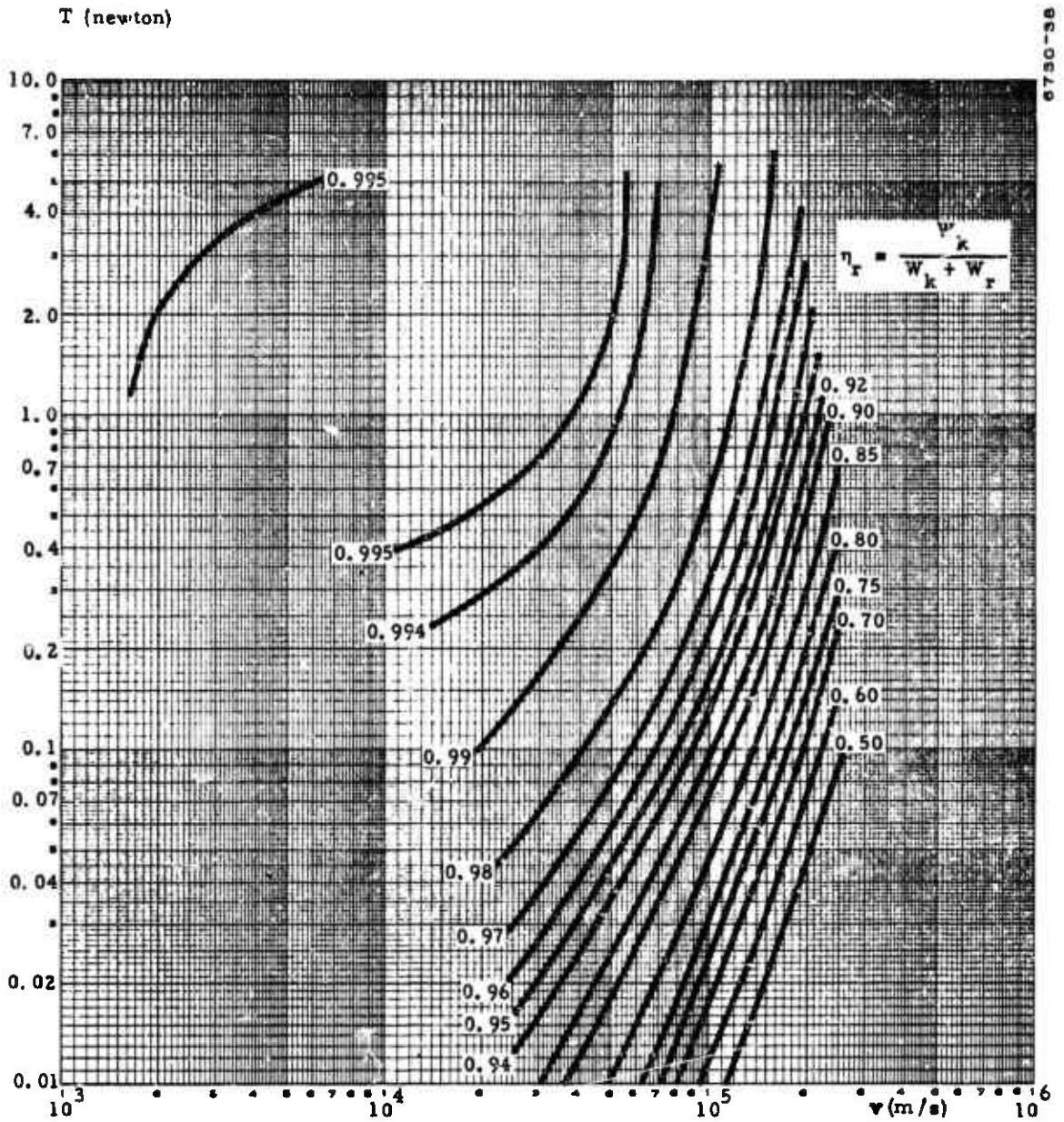

Figure 2-38. Ohmic Efficiency of Coil vs Thrust and Terminal Velocity at Constant Frequency (f = 70 Kilohertz)

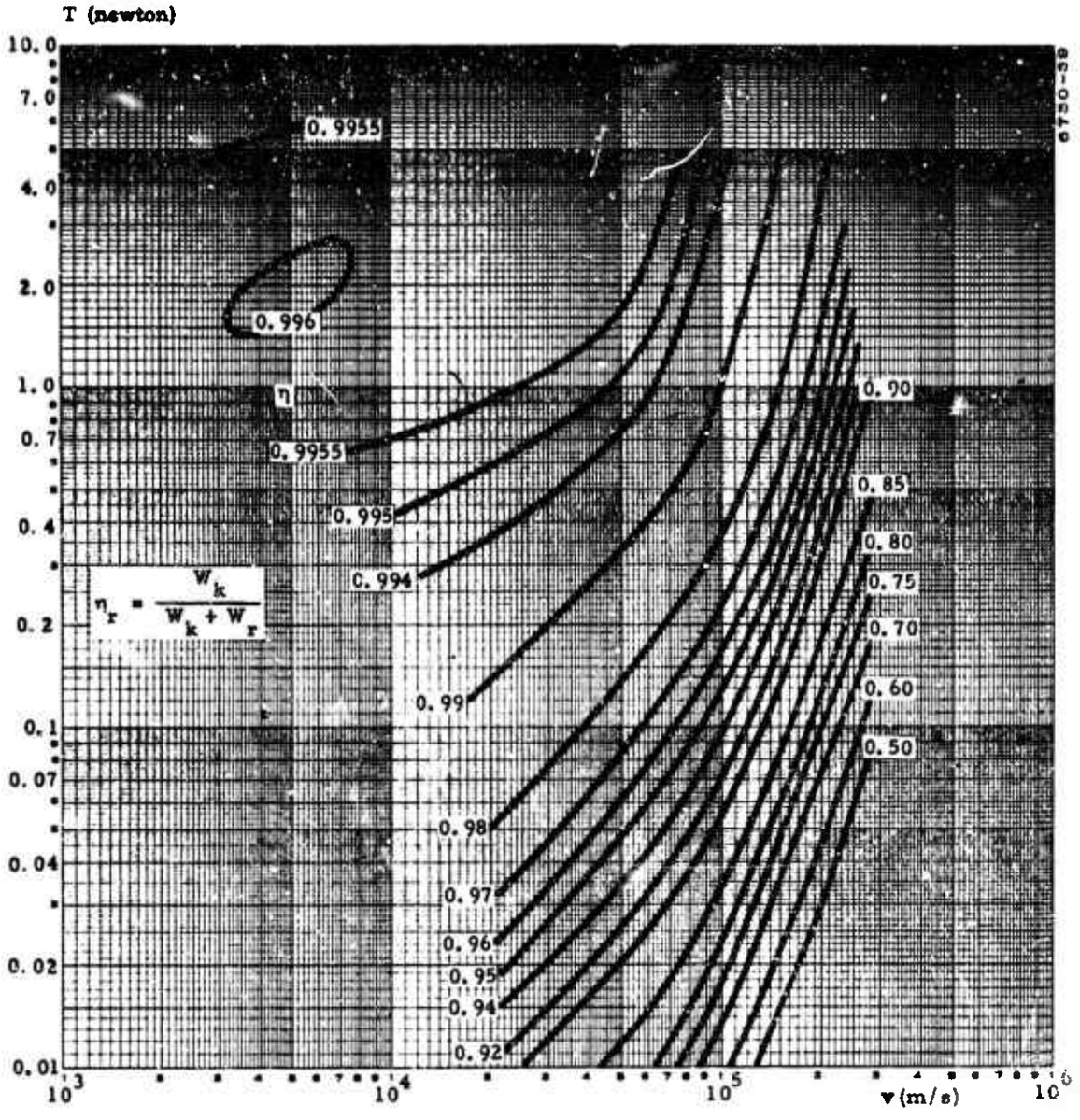

Figure 2-39. Ohmic Efficiency of Coil vs Thrust and Terminal Velocity at Constant Frequency (f = 100 Kilohertz)

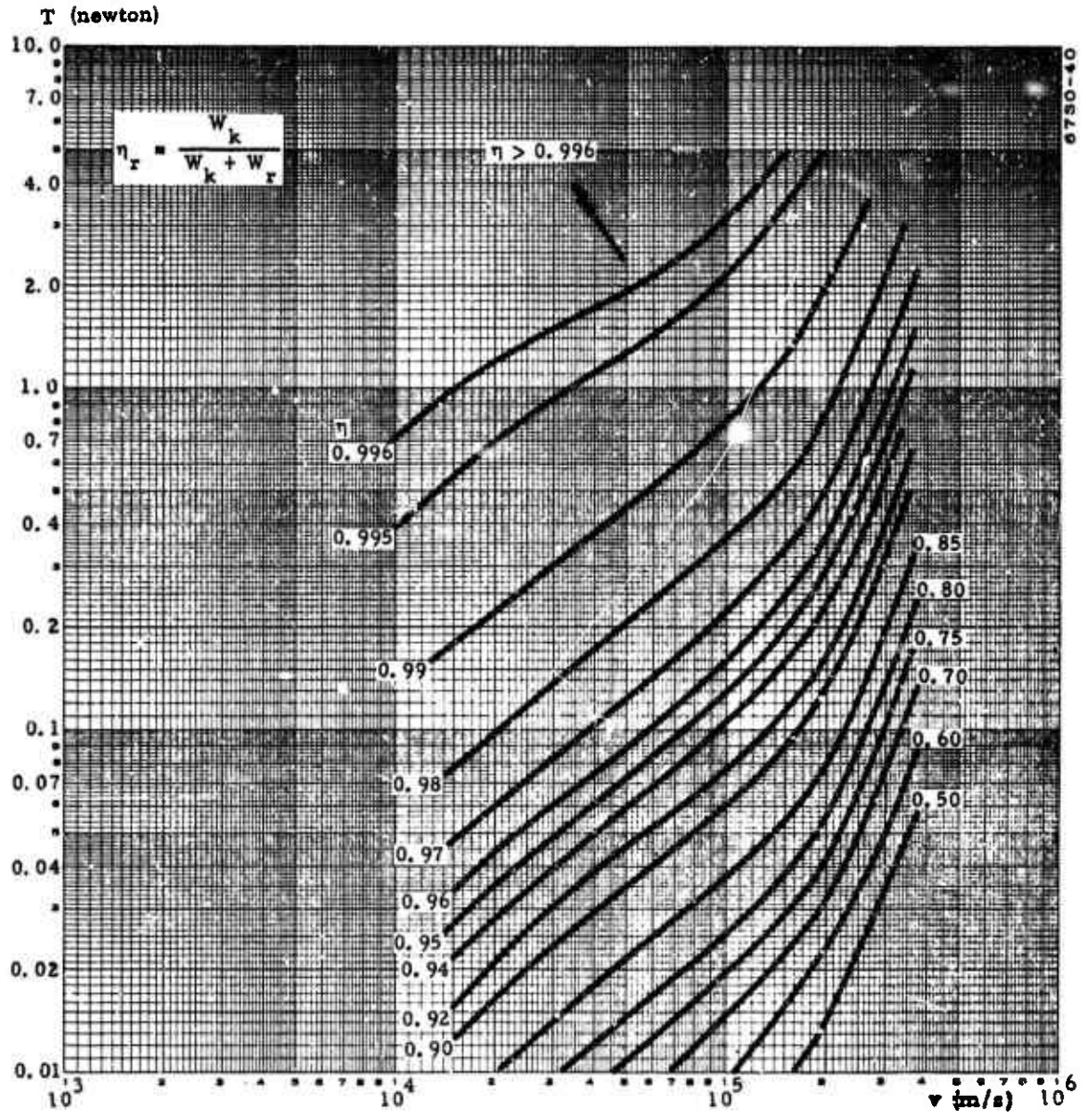

Figure 2-40. Ohmic Efficiency of Coil vs Thrust and Terminal Velocity at Constant Frequency (f = 240 Kilohertz)

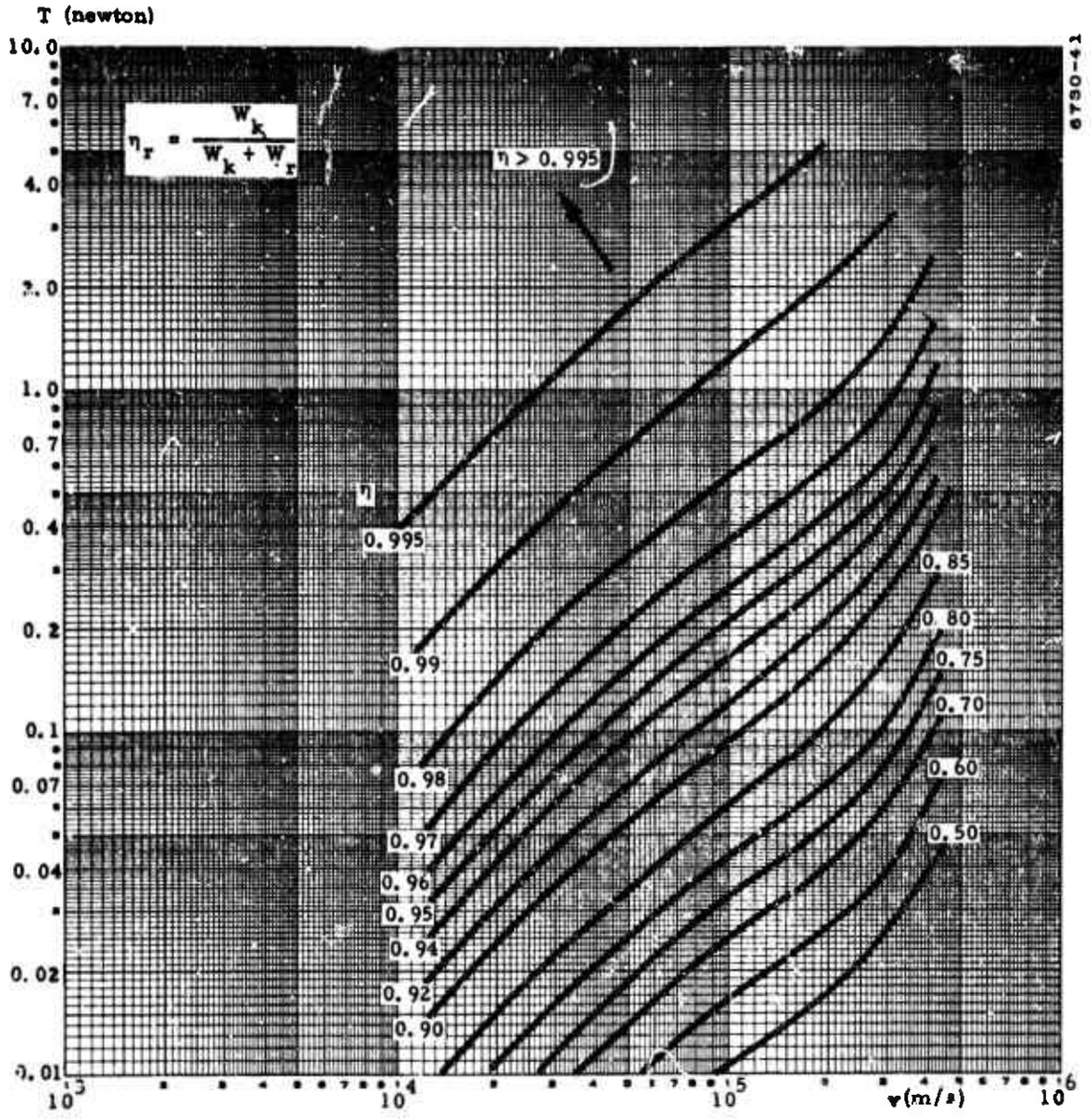

Figure 2-41. Ohmic Efficiency of Coil vs Thrust and Terminal Velocity at Constant Frequency (f = 500 Kilohertz)

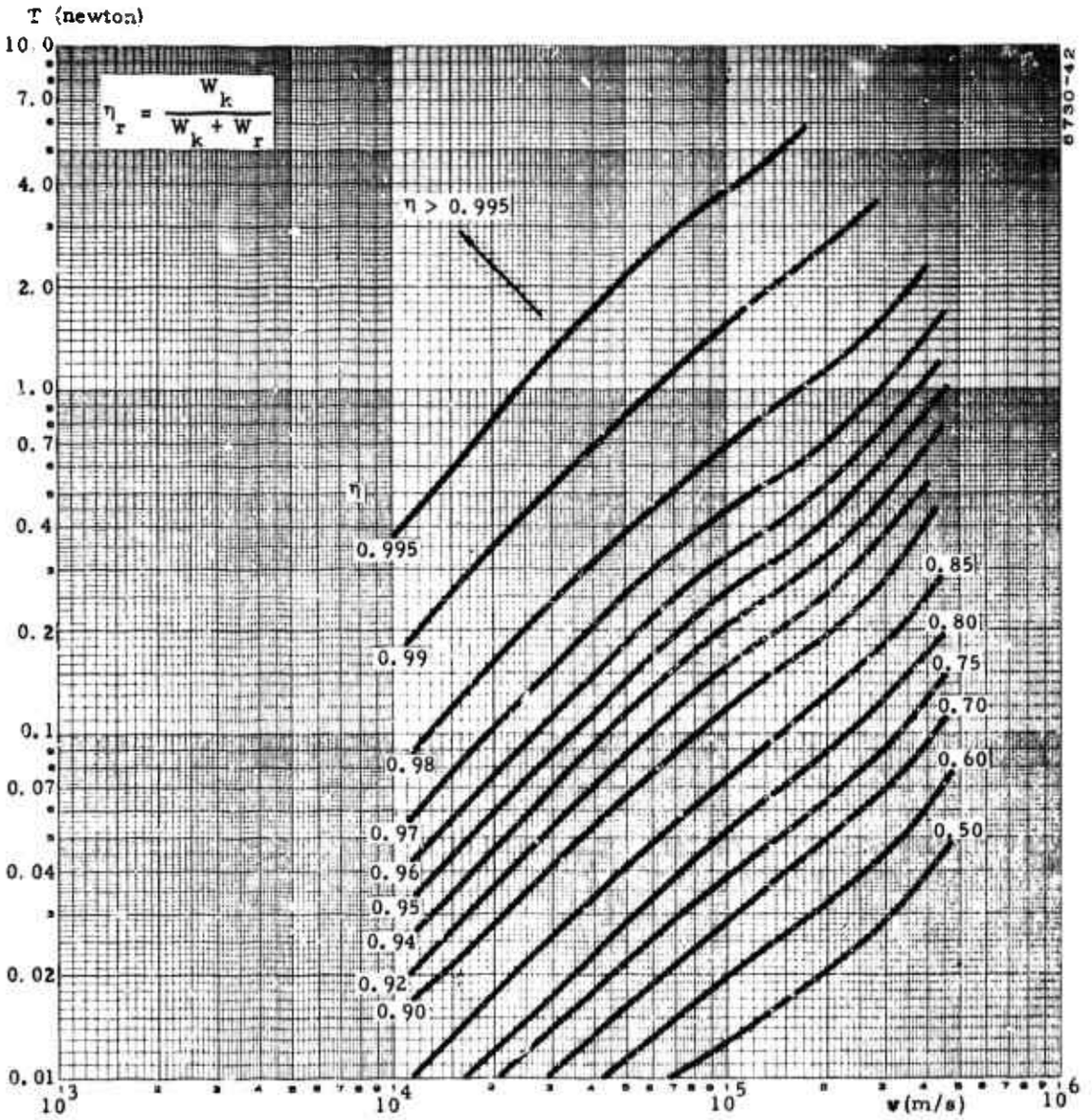

Figure 2-42. Ohmic Efficiency of Coil vs Thrust and Terminal Velocity at Constant Frequency (f = 700 Kilohertz)

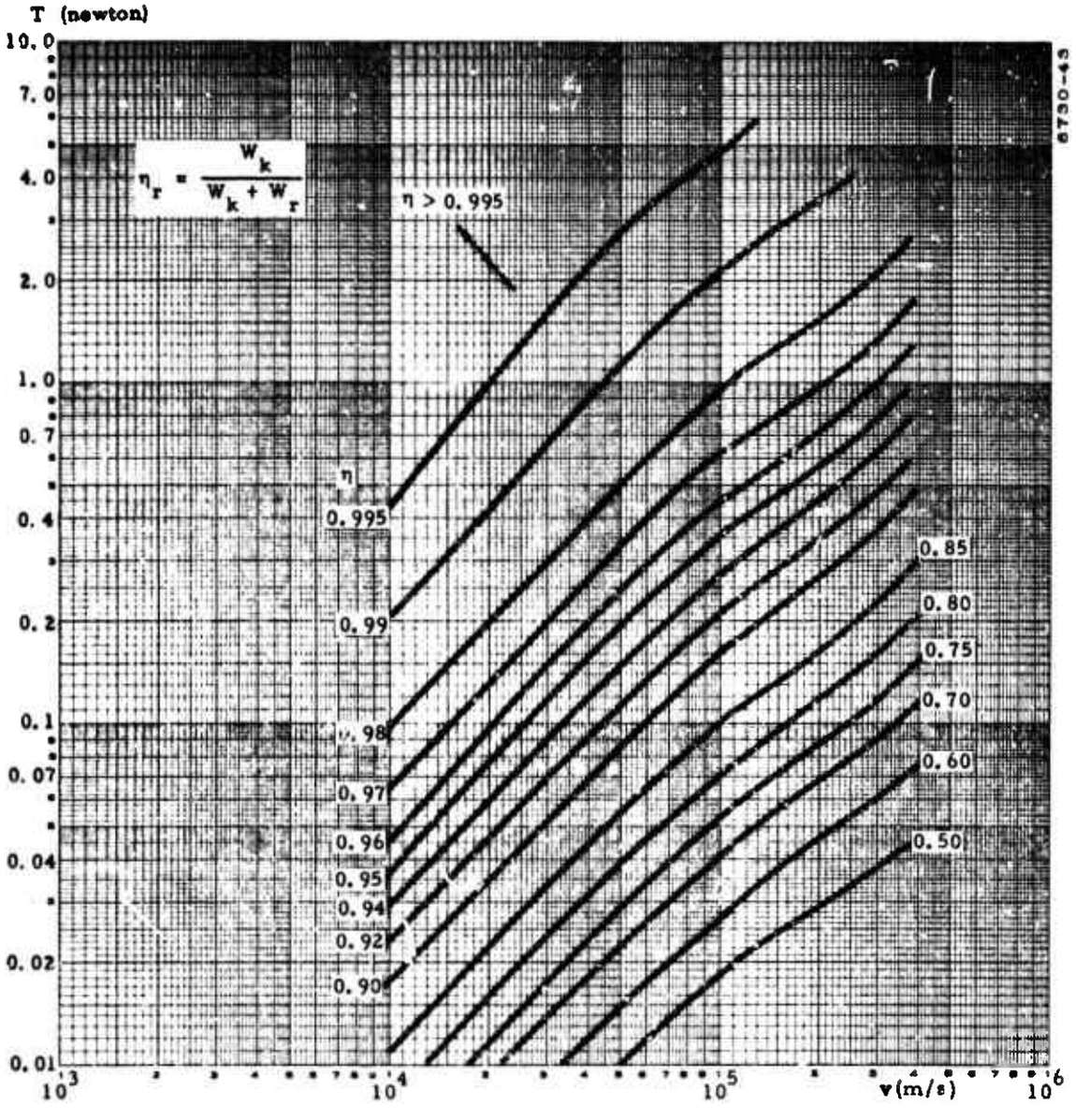

Figure 2-43. Ohmic Efficiency of Coil vs Thrust and Terminal Velocity at Constant Frequency (f = 1 Megahertz)

and therefore more efficient at lower dissipation levels, say ≤ 1000 watts. For power ≥1000 watts the temperature will be higher, and the losses relatively more severe which would probably result in thermal coil damage. For this reason the curves are shown dotted for ≥1000 watt.

b. The only losses considered in the definition of η_r are the I^2R losses in the coil; η_r does not include ionization losses or the mass utilization efficiency. Therefore it is not a suitable overall efficiency, but it was computed for the radiation-cooled coil since the I^2R losses are relatively more important than in the water-cooled coil and these losses should be minimized regardless of the presence of other loss mechanizms.

c. From the performance curves (Figure 2-5 through 2-15) it can be seen that performance generally peaks between 100 Khz and 1 Mhz. Since the instrumentation developed under the previous contract was designed for 240 Khz it was decided that the frequency should remain the same. It is not a trivial job to change instrumentation and re-calibrate for a different frequency; this would only be done if results significantly better would be expected.

Figure 2-44 is a performance curve at 240 Khz in the T-v plane where the lines of constant coil current are given in rms amperes.

2.3 THRUSTOR MODELS

The performance computed in Section 2.2 is based on the assumption that the thrust is generated by the acceleration of ionized mass under the action of an electromagnetic field. The current needed to generate the field is known, and the I^2R losses can be computed for a given coil geometry. To these losses one must add the amount of power needed to ionize the gas. The ionization energy of mercury is 10.4 electron volts, but in general more electron volts are required to generate an ion pair; typically several hundred electron volts. An efficient ionization mechanism must ionize a large fraction of the number of atoms present, and spend few electron-volts per ion to do it. One cannot predict accurately in advance what fraction will be ionized in the thrustor, nor how much power will be used in doing it; it is possible however to arrive at some estimates of the effects on the predicted efficiency of either loss mechanism.

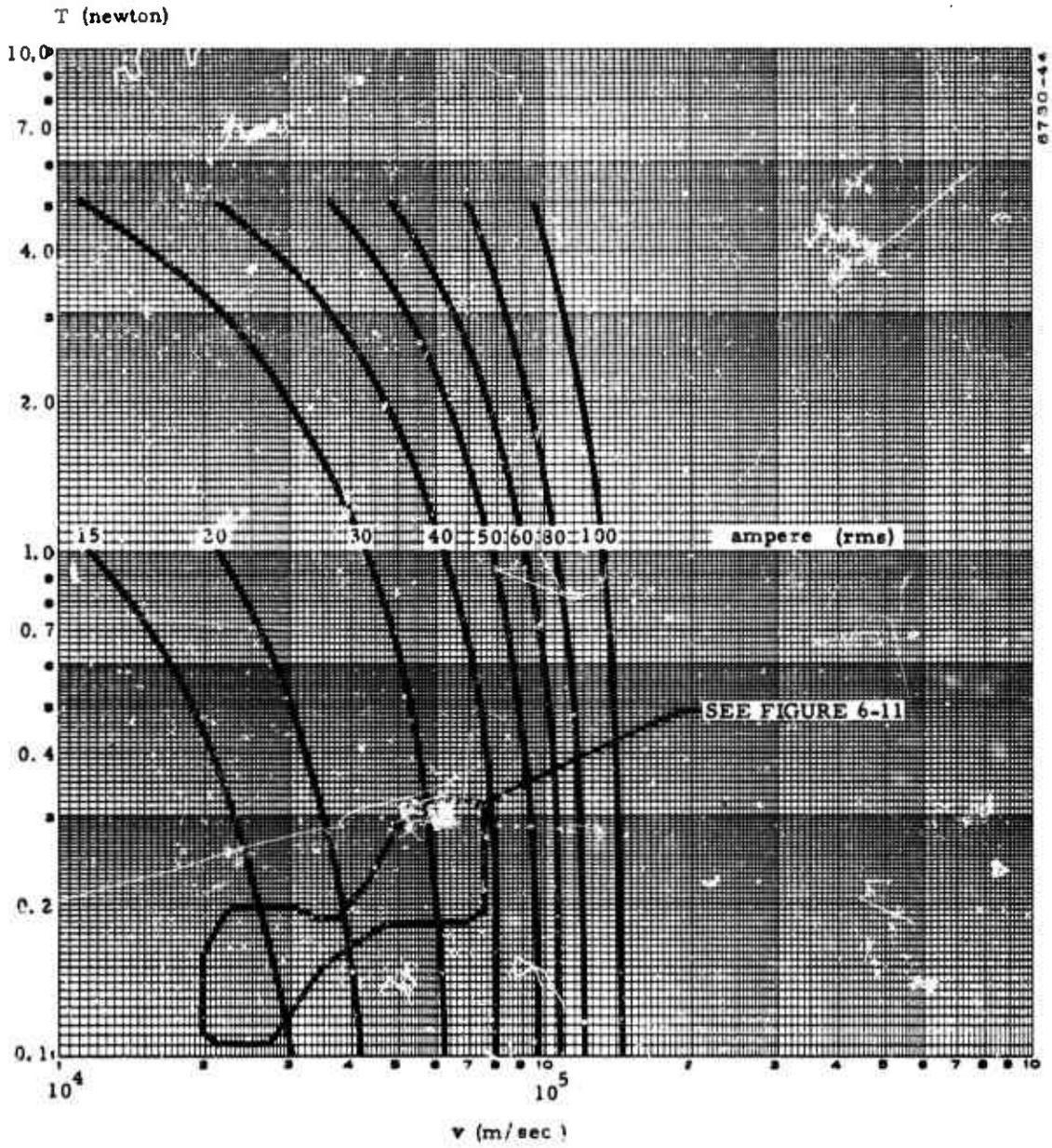

Figure 2-44. Coil Current vs Thrust and Terminal Velocity (f ~ 240 Kilohertz)

If the effluent mass is only partially ionized, and the ionized fraction is accelerated to the predicted velocity, the neutral fraction may be partially dragged along by collisions and charge-exchange processes. The effect will be strong if the mean free path is short compared with the dimensions of the accelerating region, weak otherwise. In the limit, when the mean free path is very large, the effect will be negligible and the entire thrust will be due to the ionized fraction accelerated to the full exhaust velocity, while the neutral fraction will contribute nothing. In this limiting case, since the effective velocity is computed dividing the measured thrust by the total mass flow, the observed effective velocity $\bar{v}$ will be decreased by the ratio of ionized mass to the total mass, i.e., by the mass utilization η_m, and similarly for the power efficiency

$$\bar{v} = T/\dot{m} = \eta_m \bar{v}_*$$

$$\eta = T^2/2\dot{m} W_e = \eta_m \eta_*$$

$$\eta_m = \dot{m}_*/\dot{m} = \dot{m}_i/\dot{m}$$

where the asterisk refers to the ionized portion only. This model can be called the zero-coupling model, and can be expected to be valid at a very low value of mass flow, when the density in the interaction region is low. It is therefore important to compute the particle density in the interaction region as a function of mass flow. Figure 2-45 shows the computed density (particles per cubic meter) as a function of axial distance, z (cm) from the nozzle, under the following assumptions:

a. A line source at the location of the nozzle

b. Exit velocity equal to sonic (thermal) velocity at the expected temperature of the nozzle (260 m/s)

c. Cosine distribution with angle from the axis

Superimposed on the graph is a duplication of Figure 2-3, redrawn to the new axial scale z, showing the inductive potential and indicating the extent of the region over which the acceleration forces are effective. Also shown are (dashed) lines relating particle density to charge-exchange mean free path for three values of ion velocity[2]; mean free path lengths are read in centimeters on the abscissa. It can be seen that the mean

[2]Hasted, J.B. "Physics of Atomic Collisions", Washington 1964, p. 416

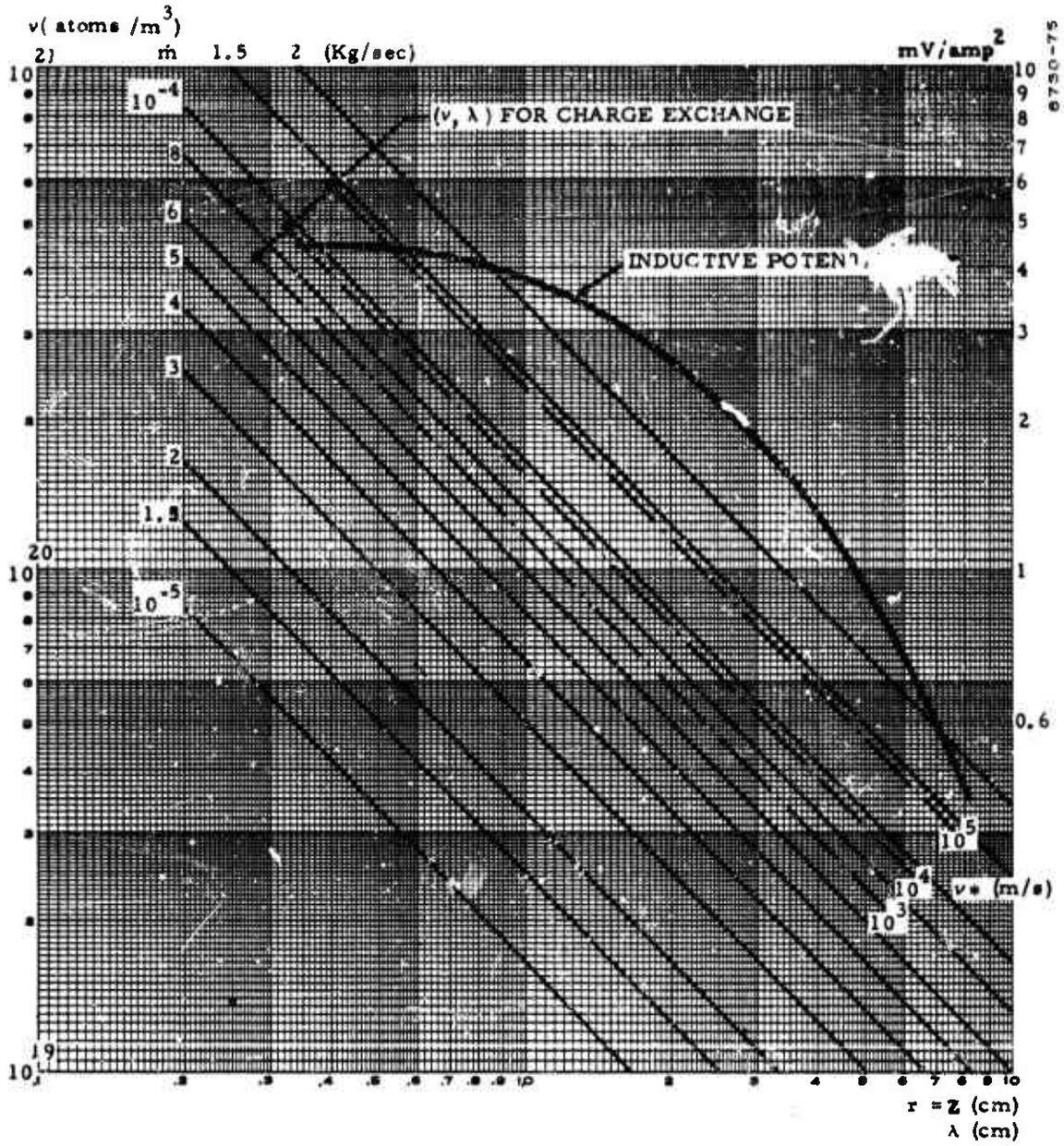

Figure 2-45. Particle Density in Interaction Region

free path is of the order of the dimensions of the interaction region for all values of mass flow of interest, so that the zero-coupling model may provide a reasonably good approximation for the operation of the thrustor. To be sure, collisions and charge exchange processes will occur but will not be dominant; and comparison with the experimental results will show their relative importance.

A consequence of this situation is that the operating efficiency is directly proportional to the fraction of ions produced, and any mechanism that can increase it will correspondingly improve the efficiency. There are three main mechanisms for ion production:

a. The induction field, where the loop voltage V is equal to the flux rate of change $d\Phi/dt$ and the electric field strength E_θ is equal to $V/2\pi R$. From Figure 2-1 we have, at 240 Khz and 1 cm from the plane of the coil,

$$E_\theta = 8.8\, I_L$$

where E_θ is in volt/meter and I_L is ampere.

b. The field due to the end-to-end voltage of the coil. This field may be locally stronger than E_θ and may provide some of the ionization, but it also provides a mechanism for ion removal since it can drive electrons into the walls of the coil. Since these electrons then tend to neutralize the field, and since the maximum path length available to this field is short for the prevailing density (the conditions are far up the low-pressure branch of Paschen's curve), the contribution of this field is probably minor.

c. The pre-ionization of the effluent gas from the nozzle. This derives from back-streaming electrons and is always present during normal operation of the thrustor. The gas coming out of the nozzle is strongly luminous and appears ionized on the spectrograph. The contribution of this source amounts probably to a few percent.

The only mechanism capable of producing massive ionization is the first one. Sudden and large improvement of performance, observed in other electrodeless induction devices, were traced to the dominance of this mechanism when the E_θ field becomes sufficiently strong and causes an avalanche increase of ionization around the loop of plasma. It is

therefore important to estimate the range of parameters over which avalanche ionization can take place.

Under steady state operation the rate of production of ions must be equal to the rate of removal, and both must be uniform around the plasma ring; the electron density (equal to the ion density) must be sufficient to insure that more electrons are made under the influence of the E_θ field. The number of electrons that one electron makes per unit length is proportional to the number of neutral atoms available (and therefore to the density and, in the case of the thrustor, to the neutral mass flow). In the usual case this is written as

$$\frac{dn_e}{dx} = \alpha n_e (n - n_e)$$

where α is known as Townsend's first coefficient and n is the initial atom density. In the case of the thrustor the rate of electron production is equal to the rate of ion ejection flow per unit length. By indicating time rates with the usual dot we have

$$n_e = n_i$$

$$\dot{n}_e = \dot{n}_i$$

$$\frac{d\dot{n}_i}{dx} = \alpha \dot{n}_i (n - n_i).$$

Now the rate of ion ejection per unit length of plasma ring, being uniform, is equal to the total rate of ion ejection divided by the total length of the ring; multiplying by the mass of the ions we have

$$\frac{\dot{m}_i}{2\pi R} = \alpha \dot{m}_i (n - n_i);$$

to this we may add a small term b which represents the contribution of other sources. We have already noted that the density n is proportional to the mass flow, as illustrated in Figure 2-45, say

$$n = c\,\dot{m}, \quad \dot{n}_i = c\,\dot{m}_i$$

we have then

$$\frac{\dot{m}_i}{2\pi R} = c\, a\, \dot{m}_1 (\dot{m} - \dot{m}_i) + b$$

$$\frac{\eta_m}{2\pi R} = c\, a \eta_m \dot{m} (1 - \eta_m) + \frac{b}{\dot{m}}$$

$$\eta_m^2 + \left[\frac{1}{2\pi R\ ca\dot{m}} - 1\right]\eta_m - \frac{b}{ca\dot{m}^2} = 0$$

If no other sources of electrons are present, so that b = 0, η_m will be larger than zero if

$$2\pi R ca\dot{m} > 1,$$

otherwise the plasma will not sustain ionization under the action of the E_θ field. If b is not zero there will be some ionization for lower values of the E_θ field, but the transition to high density will occur when the E_θ avalanche takes over. Since a is a function of E and n (or c $\dot{m}$), taking the published values[3] of a it is possible to compute the boundary for

$$2\pi R\ ca\dot{m} = 1$$

as a function of I_L and $\dot{m}$. This is shown in Figure 2-46. The curve is probably more nearly correct for $\dot{m}$<0.1 grams/sec, where the mean free path approaches the dimensions of the interaction region and the zero-coupling model is more nearly verified. The location of the avalanche threshold becomes more uncertain for larger mass flows, but the general shape of the curve is probably correct. For comparison, the dashed line on the same graph shows the location of the threshold for the thrustor with ferrites used in Contract AF 33(657)-8697, subject to the same type of uncertainty. The value of b cannot be predicted a priori except to the extent that it is likely to be small, so as to yield values of η_m between 0.05 and 0.10 in the region below the avalanche boundary to conform with the experimental evidence.

[3] Brown, S. C., "Basic data of Plasma Physics" Wiley, New York 1959, p. 129

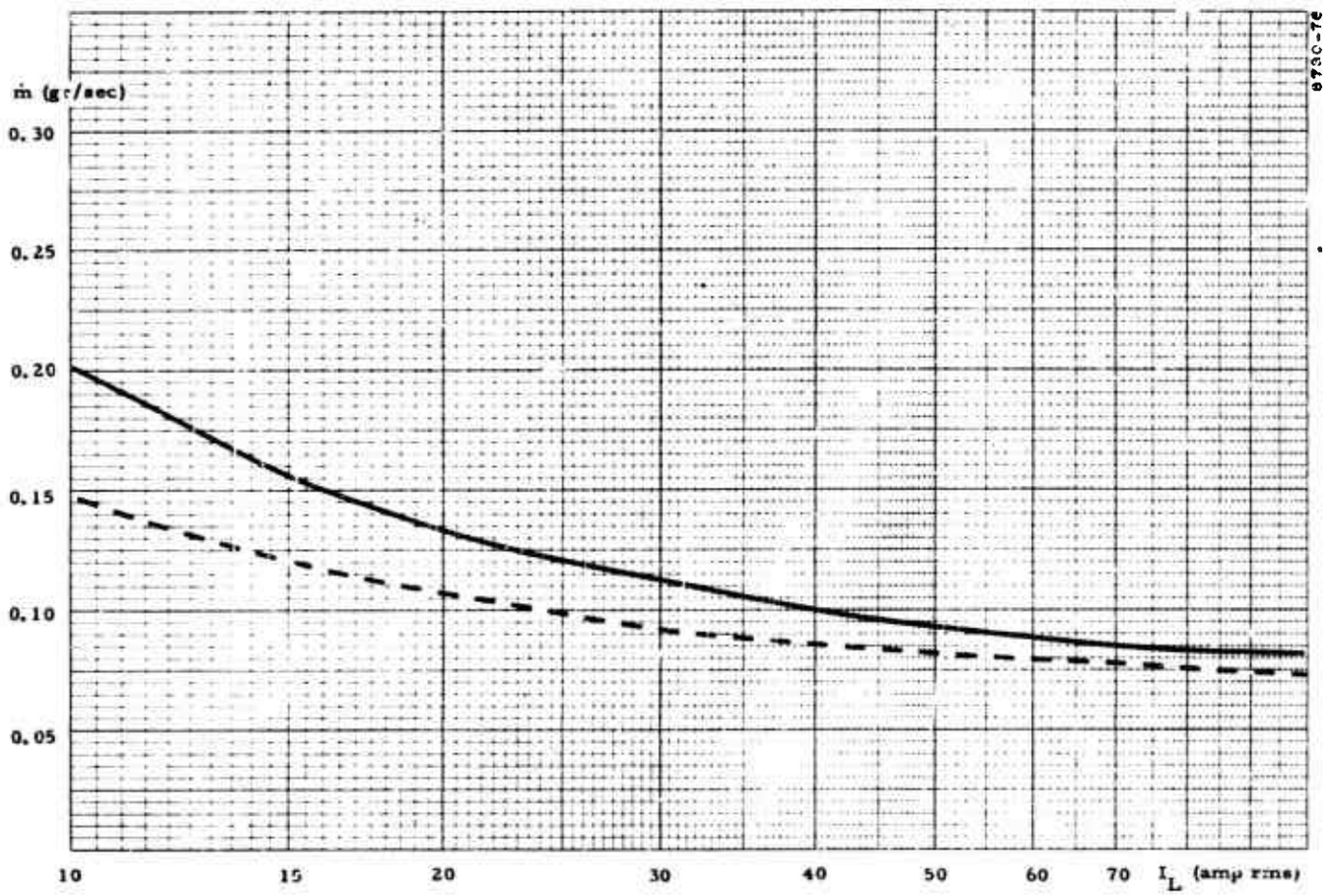

Figure 2-46. Probable Boundary of High Performance Area

Figure 2-47 is a plot of thrust/current vs $\dot{m}$ derived from the theoretical curves for the thrustor at 240 khz. The curve labeled $\eta_m = 1$ is the curve directly derived from the theory. The lines fanning out from the band are labelled by the thrust; these variations are due to the loading factor, i.e. the Lenz's law effect of the plasma currents on the field producing them. The other curves (abbreviated to the range of the present data) are derived by assuming that the same thrust is generated by the same number of particles accelerated for different values of added neutral mass flow, so they are labelled by mass utilization efficiencies. The graph is reproduced in Section 6.2 with the experimental points added, where the η_m are interpreted as degrees of ionization and the zero-coupling data reduction is presented.

2.4 CONSIDERATION OF THE THRUSTOR AS A PULSED DEVICE

In the previous contract period it was shown that the thrustor can reach quite high efficiencies at high power levels. In certain applications the total developed thrust is not necessary but the high efficiencies are attractive. This leads one to consider the possibility of using the thrustor in a pulsed mode where full thrust is developed for short times; i.e., a duty cycle which gives the desired average thrust, but with an efficiency commensurate with the high peak thrust values.

We consider here the use of a pulsed mercury vapor feed system and we choose one which is presently undergoing development since pulsed vapor systems are not easy to come by and this one appears to be promising. The thrustor has never been operated in the mode investigated here so some broad assumptions are implicit in these considerations, namely that we may pick out performances in the steady-state and apply them to the pulsed mode. The particular operating conditions are those shown in Figure B-12 of the Report. The pulsed feed system is that under development at the General Electric Space Sciences Laboratory[4]. The device (called the Exploded Liquid Metal (ELM) Injector) produces a pulsed mercury vapor stream and has been tested over a range of duty cycles and with variable mass/pulse. Estimates have been made of the actual length in time of the vapor pulse by probing downstream of the output nozzle. The parameters to be chosen are

a - mass/pulse

[4]Gorowitz B., Karras T., Cook C., and Gloersen P.. Summary Report Research and Development on the Pulsed Plasma Accelerator, April 1967. Contract NAS3-8906.

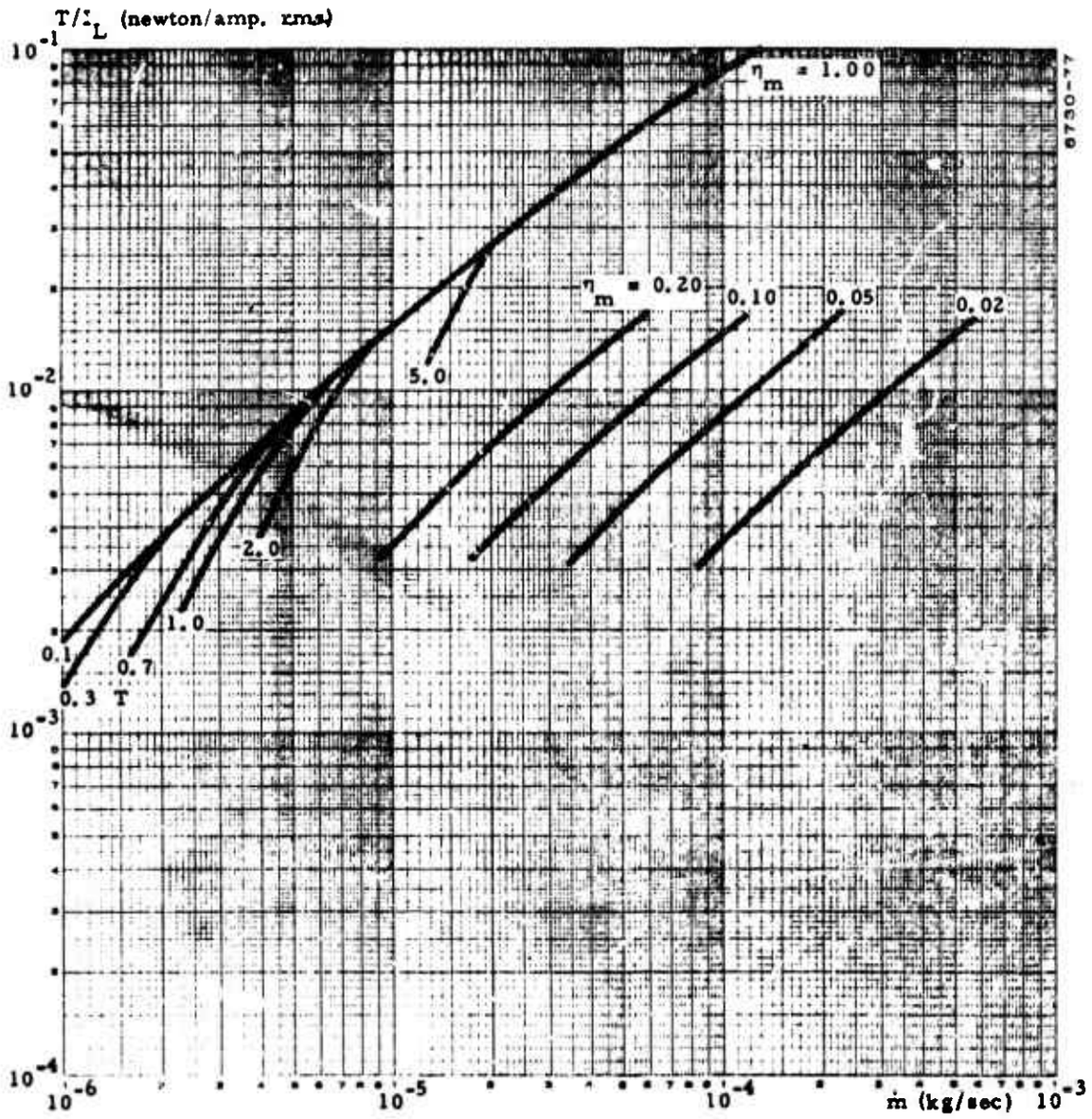

Figure 2-47. Mass Utilization

b - repetition rate

c - number of injectors

d - pulse length

Since we wish to use the data of Figure B-12 we must choose among the parameters in a reasonable way to get the instantaneous mass flow rate of that data. Table VII of the GE report gives us the following:

a - mass/pulse = 1.5×10^{-9} Kgm

b - Repetition Rate = 167 PPS

The thrustor requires a good degree of azimuthal symmetry in the mass flow pattern and the simplest way is to use an appropriate number of injectors in an azimuthal array. A reasonable number for the present thrustor size is around ten injectors.

c - number of injectors = 10

The pulse length is estimated in the report as "a few tenths of milliseconds" so

d - pulse length = 0.2×10^{-3} seconds.

Combining a, c, and d we have

$\dot{m}$ = average mass flow rate during the pulse on-time

$$\dot{m} = \frac{1.5 \times 10^{-9}}{.2 \times 10^{-3}} \times 10 = 7.5 \times 10^{-5} \text{ Kgm/sec}$$

The data of B-12 was taken at 7.6×10^{-5} Kgm/sec. The pulse on-time of 0.2×10^{-3} sec is about 50 cycles of the RF at the present operating frequency of 240 Kilohertz and this seems long enough to assume steady operation of the thrustor. The instantaneous mass flow rate for the ELM will differ from the average during the on-time and actually the thrustor will slide through its performance curve from higher I_{sp} than that computed from the average to lower but since the time-shape of the mass flow rate is not known, the average $\dot{m}$ (averaged only over the on-time) will be used.

The thrustor operating point is chosen to be at an efficiency of 70% and therefore, from Figure B-12, an output velocity of 2.5×10^4 m/sec. The instantaneous power input is 33 KW (23 KW beam power) and an instantaneous thrust of 1.9 newton. The duty cycle, D, of the ELM at a repetition rate of 167 PPS is .033.

The average thrust <T> is given by

$$\langle T \rangle = DT \quad \text{where T is the instantaneous thrust}$$

$$\langle T \rangle = .063 \text{ newton } (.014 \text{ lbs})$$

The average power <P> depends on whether or not the RF is pulsed. To see whether it is feasible to leave the RF on continuously (avoiding switching circuits) we define an average efficiency $\langle \eta \rangle$ by:

$$\langle \eta \rangle = \frac{T^2}{2\langle \dot{m} \rangle \langle P \rangle}$$

where these averages are taken over the duty cycle:

$$\langle P \rangle = PD + P_R (1-D)$$

where P is the instantaneous power, and P_R is the coil ohmic dissipation. Writing

$$P_R = \alpha P \qquad \text{we have}$$

$$\langle \eta \rangle = \frac{T^2}{2\dot{m} P} \left[\frac{D}{D + \alpha (1-D)} \right]$$

$$= \eta \frac{D}{D + \alpha (1-D)} \qquad \text{where } \eta = 70\% \text{ at the operating point and } \alpha \simeq .07,\ D = .033$$

Therefore $\langle \eta \rangle = \frac{\eta}{3} \simeq 23\%$

This appears to be a large penalty to pay in order to avoid pulsed RF. Using pulsed RF the average efficiency can be almost as high as the instantaneous efficiency.

For example if the RF is pulsed on for a half on-time before the vapor pulse and left on for a half on-time after the pulse then:

$$\langle \eta \rangle = \eta \frac{1}{1 + a}$$

and since $a \ll 1$

$$\langle \eta \rangle = \eta (1 - a)$$

In this case then $\langle \eta \rangle = 65\%$ and the average power $\langle P \rangle$ would be given by

$$\langle P \rangle = PD (1 + a) = 1.2 \text{ KW}$$

The average thrust can be lowered by lowering the repetition rate (the other parameters are being held fixed at the known values which work) as can the average power. Since the repetition rate used here is the highest one reported it would not be realistic to discuss raising it.

To summarize these sample calculations we have

$\langle T \rangle = .063$ newton

$I_{sp} = 2500$ seconds

$\langle \dot{m} \rangle = 2.5 \times 10^{-6}$ Kgm/sec

$\langle P \rangle = 1.2$ KW

$\langle \eta \rangle = 65\%$

3. THRUSTOR VACUUM CHAMBER

3.1 GENERAL

The major changes made in the thrustor chamber system was the installation of a KDH-130 forepump and a completely new system of water baffles. Otherwise, the chamber is as described in the Report.

3.2 VACUUM SYSTEM

The chamber pumping system consists of a number of freon-cooled baffles for pumping mercury vapor and an MHG-900 mercury diffusion pump and associated forepumps. During the past contract it was seen that experiments were being affected because the diffusion pump became foreline-pressure limited during the experimental runs. At the beginning of this contract a Kinney KDH-130 pump was installed in parallel with the original KD-15. No further problem of foreline limitations were encountered. In addition, the increased speed substantially decreased the pumpdown time. Figure 3-1 is a chamber pumpdown curve.

3.3 WATER BAFFLES

The middle water baffle system shown in the Report (Figure 4-31) was scrapped and a new system built. The new system better protects the chamber ports from direct radiation and impingement of hot gas (one chamber port cracked in an extended run during the previous contract period) and permits a calorimetric power measurement over the entire chamber surface. The baffles are shown in the photograph of Figure 3-2. The barrel baffle containes four iris baffles which act as radiation and impingement barriers and the five sections are connected in series. The chamber water systems are shown in Figure 3-3. The No. 3 system cools the upper baffle alone. The No. 2 system supplies the catcher, lower barrel and middle barrel-iris combination, all connected in series. The triangles of Figure 3-3 indicate thermocouple

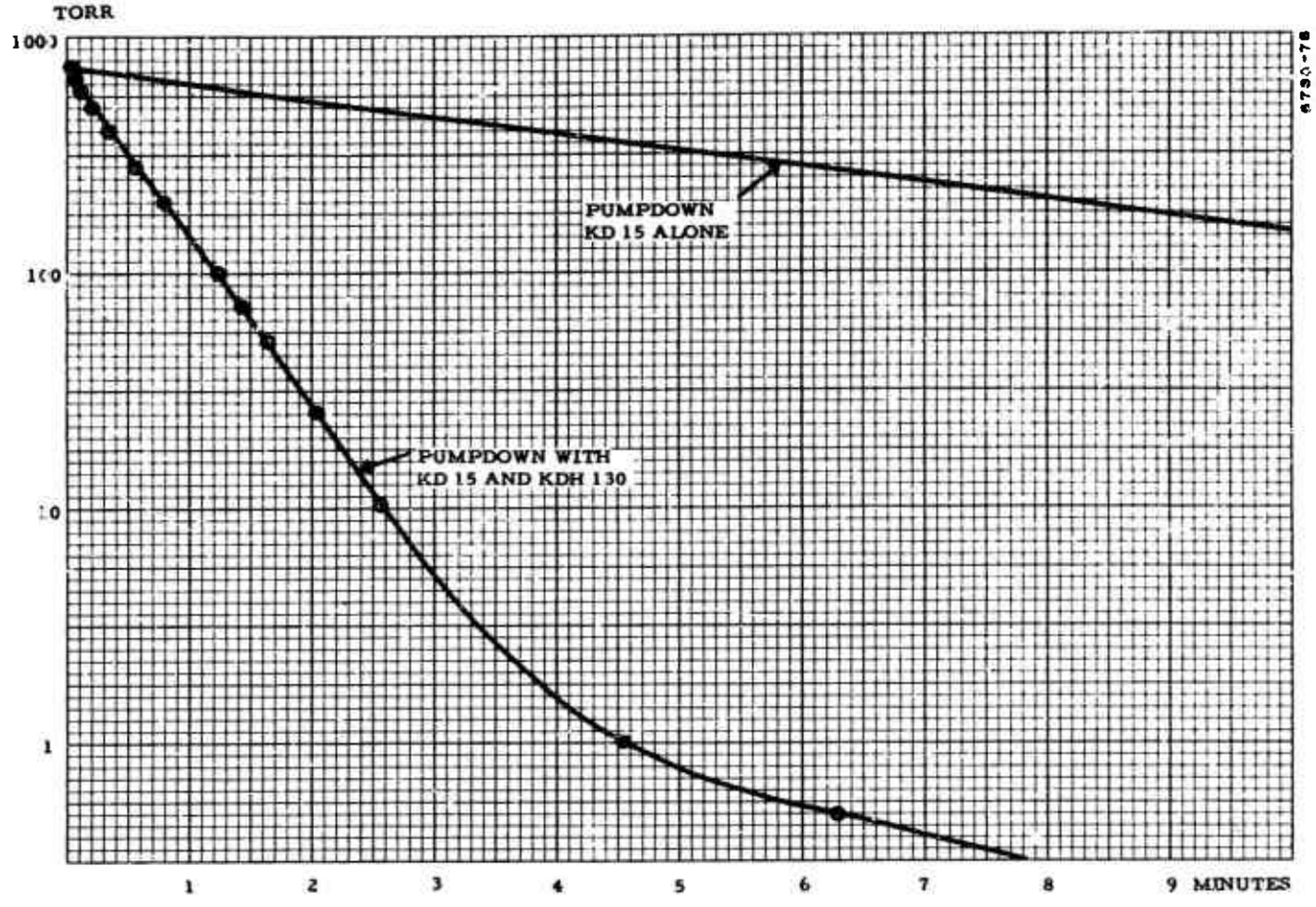

Figure 3-1. Pumpdown Curve of Chamber with KDH 130 Pump

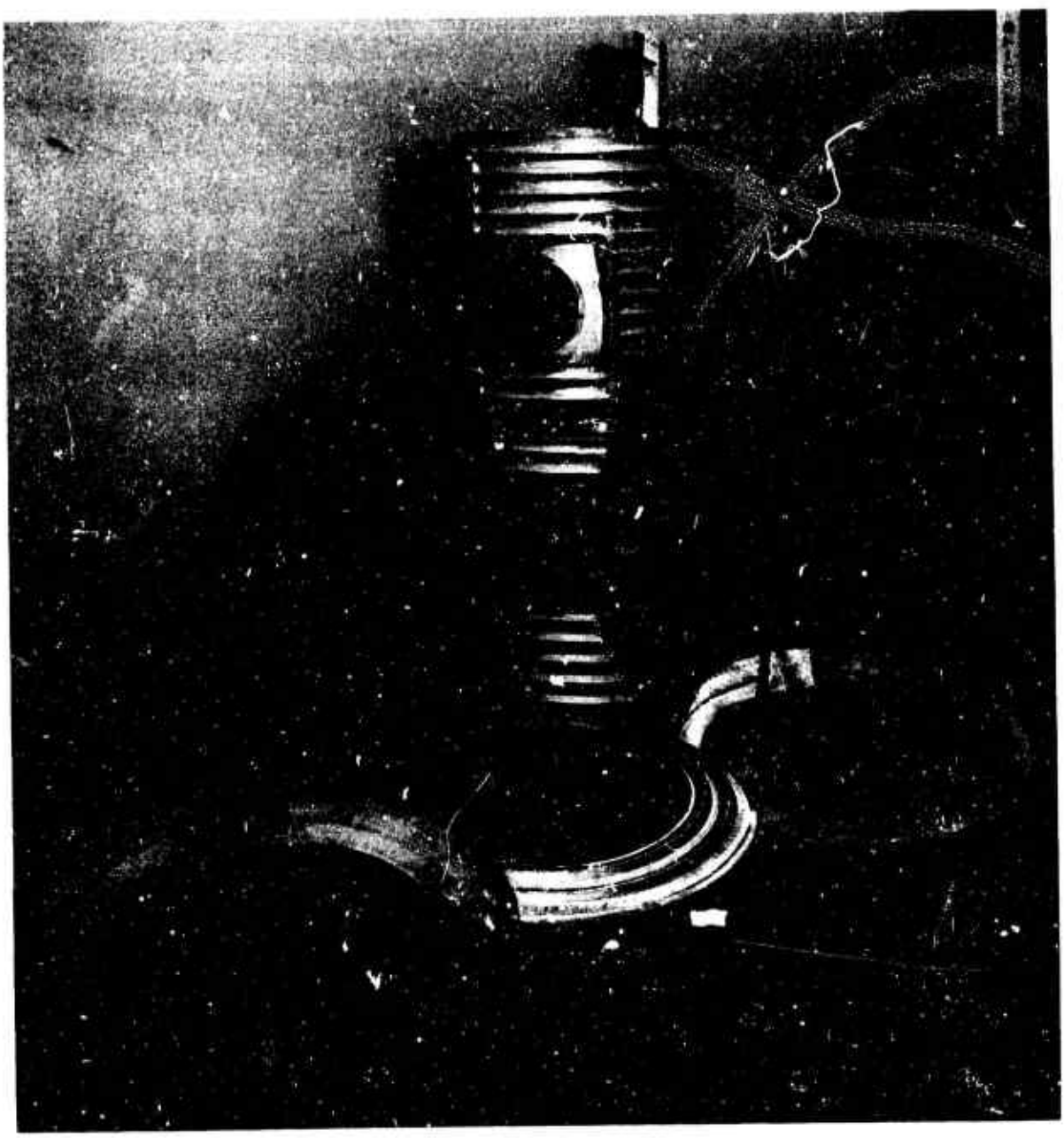

Figure 3-2. New Water Baffles

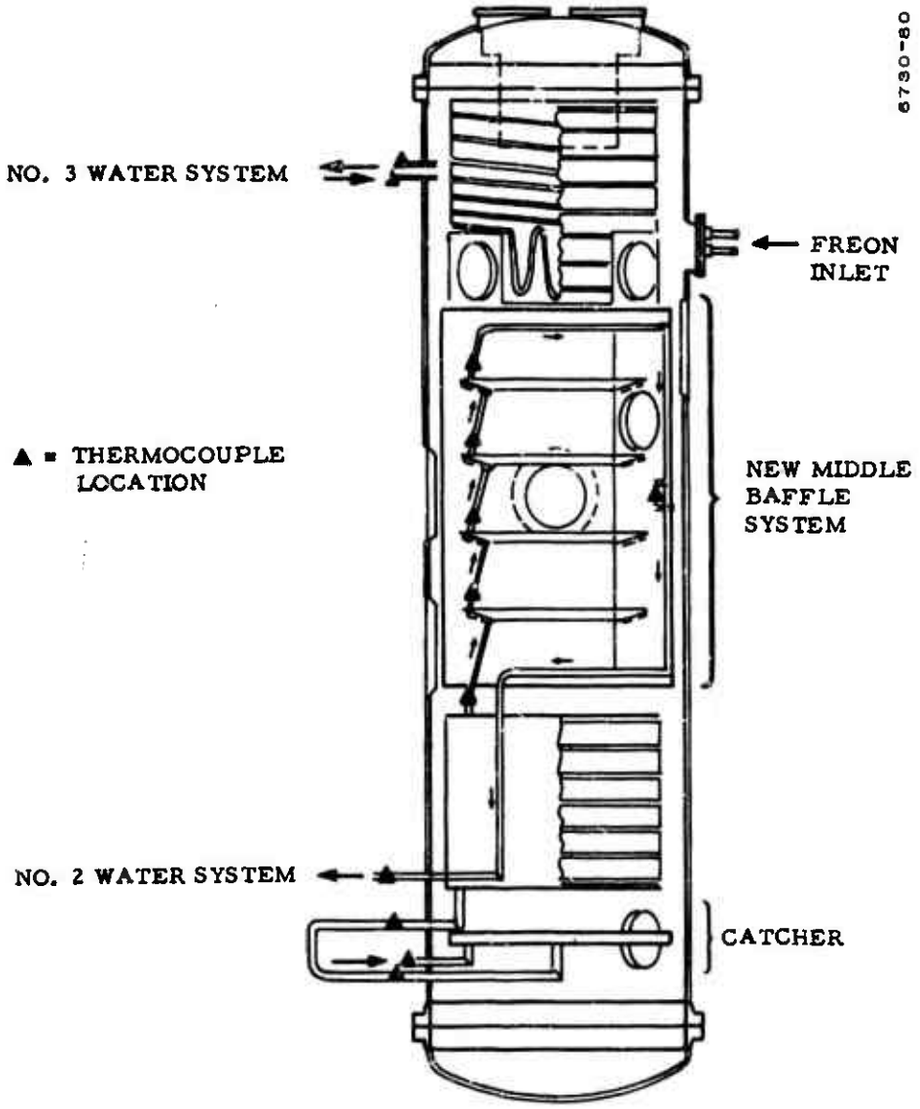

Figure 3-3. Thermocouple Locations in Water System

locations. The thermocouples are connected to measure the temperature drops across the various elements. The flow in the water system is measured by diverting the flow into containers where the time to fill a fixed volume is measured.

The pressure in the system was continuously monitored by an ion gauge connected to one channel of the Sanborn recorder.

4. INSTRUMENTATION AND CALIBRATION

4.1 GENERAL

The primary parameters that describe the performance of the accelerator are thrust, mass flow, and electrical input power. At the end of Contract AF33(657)-8697 the instrumentation for the control and measurement of mass flow was entirely satisfactory, but that for the measurement of thrust and electrical power could still be improved. Accordingly, both systems were redesigned at the beginning of the contract period. The thrust platform was redesigned on the basis of the operational experience with the previous system. A new power measuring system was designed on the basis of the principles developed under AFOSR Contract AF49(638)-1251.

4.2 THRUST STAND

The test facility for the thrustor development was originally designed to accommodate a thrustor firing in a vertical attitude, with the thrust vector pointing up. The evolution of the thrust stand retained this configuration which provides two important advantages:

1. Effective balancing against the effect of mechanical noise (vibration) on the thrust measurement.
2. Ease and precision of calibration.

The element of the suspension mechanism are shown in Figure 4-1.

The thrustor is attached to the bottom surface of the platform proper and transmits the thrust to the strain gauge cell by means of an axial steel rod guided by the two ball bushings. The static weight of the thrustor, platform and any suspended accessories is balanced by three counterweights (one is shown in Figure 4-1 where a three-fold symmetry about the axis is implied). Exact balance can be obtained by adjusting the position of the fulcrums, mounted on three sliding carriages that can be simultaneously moved with smoothness and precision from outside

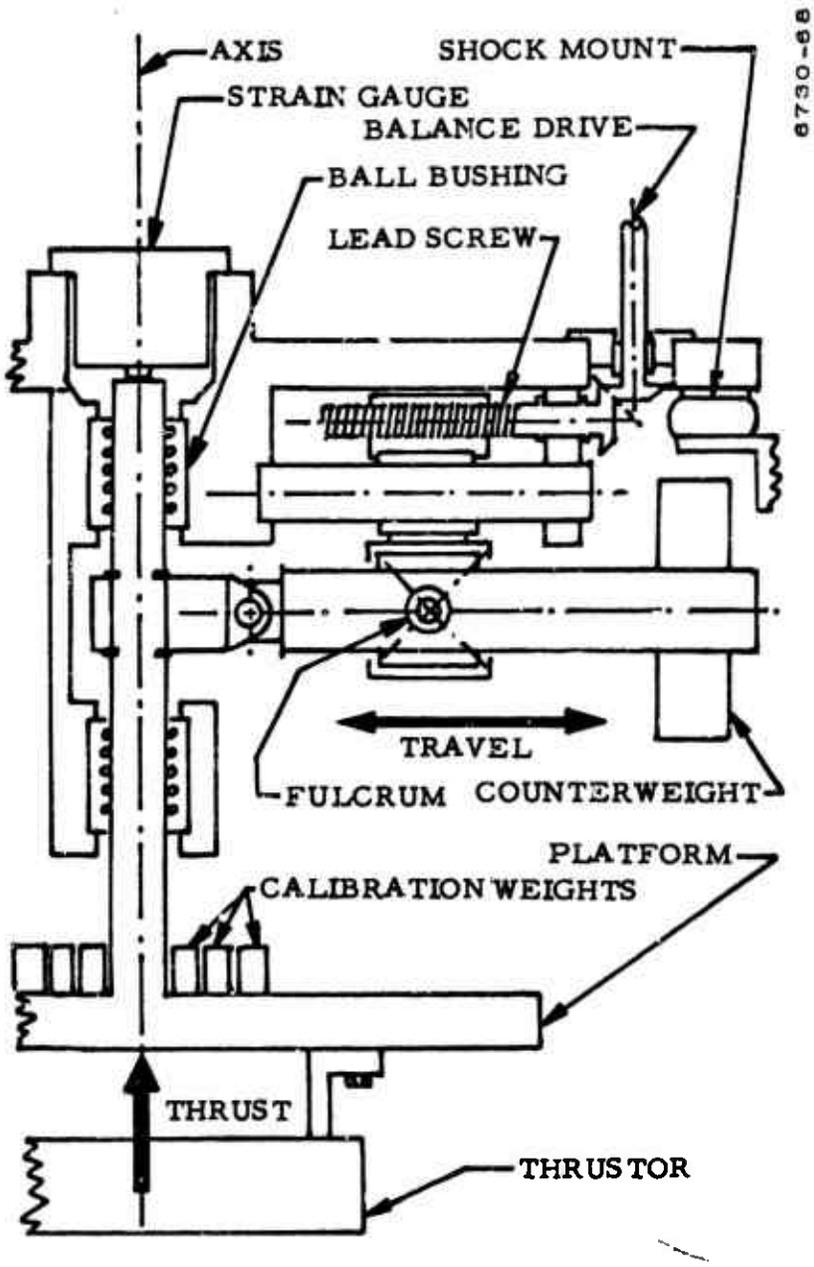

Figure 4-1. Elements of the Platform Suspension Mechanism

of the vacuum envelope. It is clear that when the platform is statically balanced it is also balanced against vibration, because the moments about the fulcrum(s) are equal whether they are due to the acceleration of gravity or to any other linear acceleration of the suspension, except for the possible elastic flexing of the structure. This is avoided by making the structure very rigid and by shock mounting the entire thrust stand: the resonant frequency of the total mass on the shock mounts is distinctly different and much lower than the resonant frequency of the balanced mass on the fulcrum(s), so that the vibration of the vacuum chamber, due to pumps, refrigerators, people walking about, etc., is attenuated to an entirely acceptable level by the time it causes any forces to be applied to the strain gauge cell. Typically, the residual detected noise is of the order of 0.003 newton rms when measuring a thrustor of the order of 0.5 newton with a suspended thrustor mass of 5 Kg.

The strain gauge cell (Daytonic 152-A) was found to give very accurate and reproducible readings when operated in the hostile environment of the chamber, which normally contains mercury vapor at a pressure of the order of 10^{-4} torr. The cell is in direct thermal contact with a water jacket which keeps the strain gauge cell at a constant temperature. Water cooling of strategic elements of the thrust stand prevents the generation of drifts of the indicated zero thrust due to the thermal expansion of the suspension and balance system even when the thrustor components attached to the platform are at temperatures in excess of 600°C.

A complex problem is presented by the flexible leads which must carry the power and the cooling water to the thrustor without generating any spurious forces on the thrust platform. The difficulty of the problem can be appreciated if one considers the various requirements:

1. Current capacity to 100 ampere rms at 240 KHz
2. Voltage insulation to 5 KV rms when immersed in a rarefied conductive hot plasma.
3. Internal pressure to 80 psi of cooling water
4. Indifference to thermal expansion and local electromagnetic forces

The basic structure of the flexible leads is shown in Figure 4-2.

The current-carrying, pressure-containing elements are beryllium copper bellows which provide the required flexibility. They are brazed

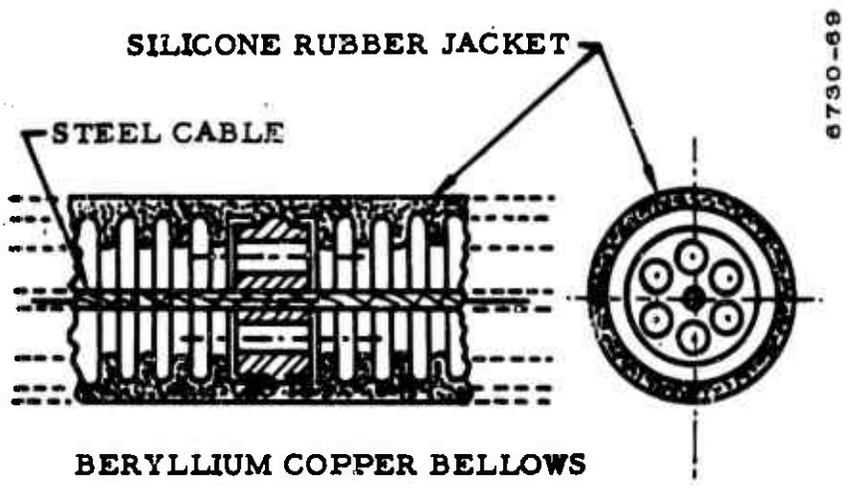

Figure 4-2. Basic Structure of Flexible Leads

to intermediate copper cylinders which are perforated in a hexagonal pattern to permit the passage of the water through six holes and the passage of a thin stainless steel cable in the center. The axial steel cable absorbs the axial tensile stress due to the internal pressure; the bellows are stabilized against snake instability by proper choice of length/diameter ratio as well as by the molded silicone rubber jacket which also supplies the needed electrical insulations.

Changes of temperature of the cooling water cause changes of length of the assembly which could be translated into spurious thrust if the resulting forces have a component parallel to the sensitive axis of the platform. This is avoided by orienting the axis of the leads perpendicular to the axis of the platform, as shown in Figure 4-3. If this precaution is not observed, the indicated thrust is subject to a small drift with a time constant corresponding to the thermal constant of the water-cooled portion of the thrustor, the drift becoming noticeable when the thrustor is fired periodically on and off. Figure 4-4 is the reproduction of two traces of the thrust channel on the Sanborn recorder under similar firing conditions (about 50 percent duty cycle, one minute period, 3 to 4 kilowatt). One trace was taken with the leads slightly misadjusted a small angle from the perpendicular, the other with the leads properly adjusted.

The strain gauge is calibrated by lifting small weights which normally rest on the upper surface of the thrust platform (see Figure 4-1). The weights are in the form of concentric rings nesting around the central vertical rod of the platform, so that their center of gravity is coincident with the axis of the rod. They are lifted by remote actuators so that exactly known amounts of equivalent thrust can be introduced at any time during a test run, whether the thrustor is firing or not. The weights are machined to provide exact calibration forces of 0.1, 0.2, 0.5, 1.0, 2.0 and 5.0 newtons; by lifting two together 0.3, 0.7, 3.0 and 7.0 newtons can be generated. Calibration over the entire range shows that the response of the strain gauge cell is extremely linear so that intermediate values can be read with confidence. The maximum probable total error in any thrust reading is estimated to be less than 0.007 newtons.

The thrust platform, once balanced, does not suffer from measurable zero drift. The zero drift attributable to mechanical vagaries of the platform is less than 0.01 newton in 24 hours, and is verifiable at any time by a built-in, remotely actuated locking mechanism which locks the platform with zero force applied to the strain gauge cell. The drift of the baselines as recorded on the Sanborn trace is attributable to the electronic

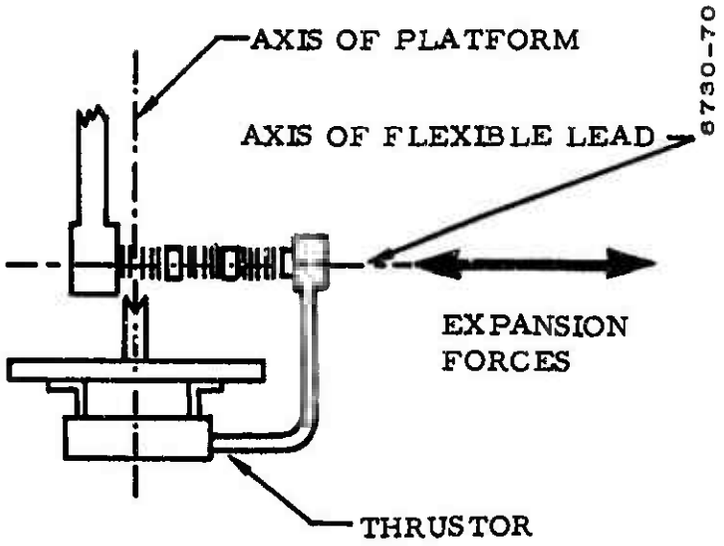

Figure 4-3. Flexible Lead Geometry

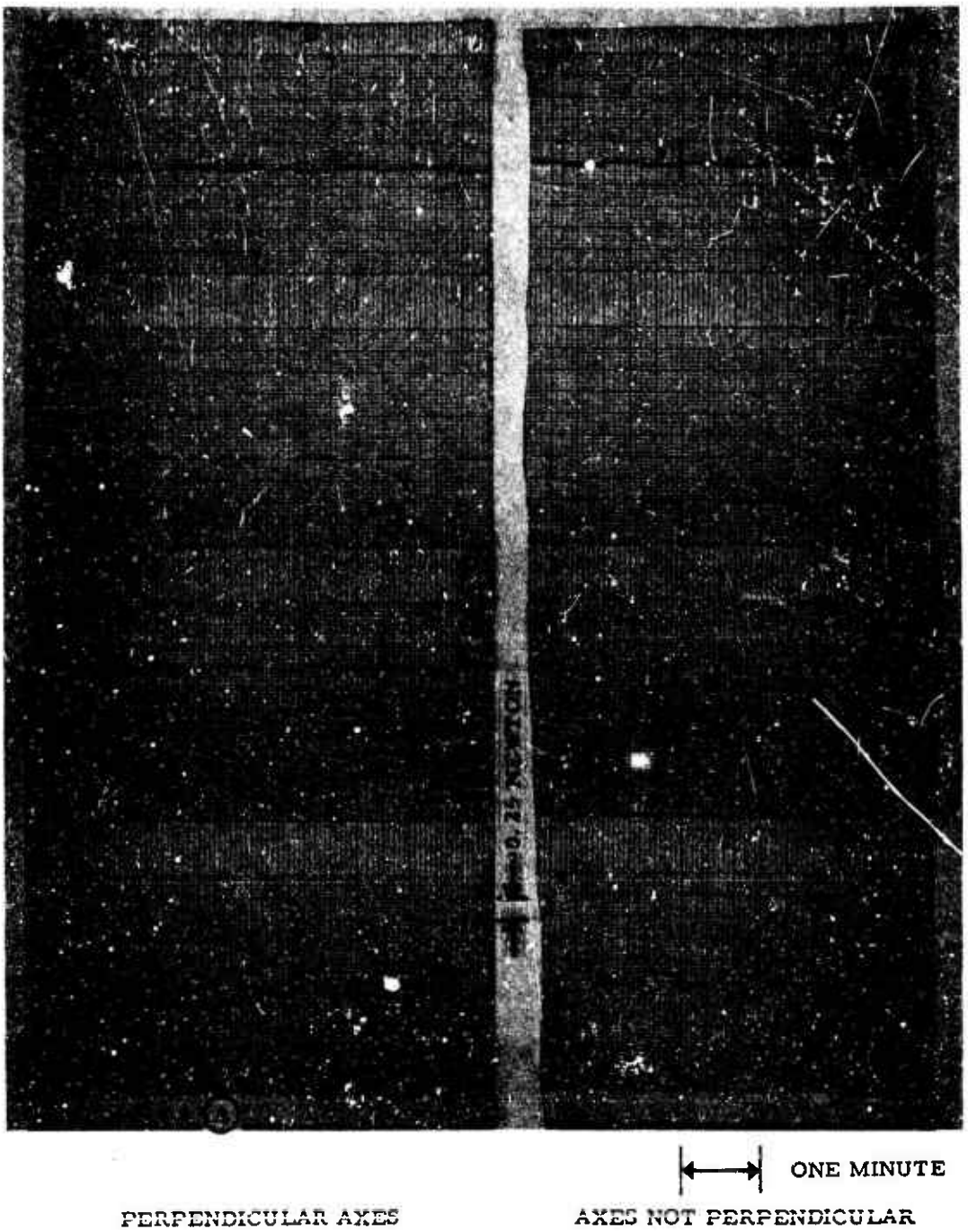

Figure 4-4. Sanborn Recorder Traces of Thrust Baseline Drift

circuits which read the strain gauge output, and can be calibrated out by use of the zero-force platform lock. The drift rate of the electronic circuits is of the order of 1 newton/24 hours and is somewhat sensitive to ambient temperature. However, no difficulty results in obtaining accurate readings, because the operation of the thrustor is automatically interrupted for two seconds every minute, thus providing a current zero baseline for all recorded quantities.

4.3 POWER MEASURING SYSTEM

The electric circuit of the thrustor is a simple inductor coupled to the plasma circuit as shown in Figure 4-5, where the equivalent resistance R represents a power sink: the power delivered to the plasma is used to ionize the gas, heat it, and accelerate it. The effect of the mutual inductance M is to reduce the effective inductance of the thrustor coil as well as to couple in a resistive component R' which appears in series with the inductance.

The operation of the thrustor depends on the variable magnetic field generated by the coil, and is therefore strongly dependent on the current flowing in the coil. It is convenient to cancel the reactance of the coil by means of a series capacitance so that, at resonance, an adequately heavy current can be made to flow in the circuit. The capacitor must be variable to tune the circuit as the effective inductance of the coil changes due to the plasma loading (as a function of mass flow and power level). The extent of the detuning caused by the plasma is reduced by adding an external inductor in series which the circuit, which acts as ballast. In addition, a small inductor is added for sensing the current flowing in the circuit. The complex circuit then appears as in Figure 4-6.

L_1 and R_1 indicate respectively the inductance and resistance of the current sensing inductor, L_2 and R_2 those of the thrustor, L_3 and R_3 those of the ballast inductor, while L and R represent the plasma loading coupled to the thrustor.

Voltage V_1 is used to measure the current I_L:

$$V_1 = R_1 I_L + j\omega L_1 I_L$$

Voltage V_2 is measured across the thrustor and contains an inductive component $j\omega L_2 I_L$ plus a resistive component, representing the ohmic

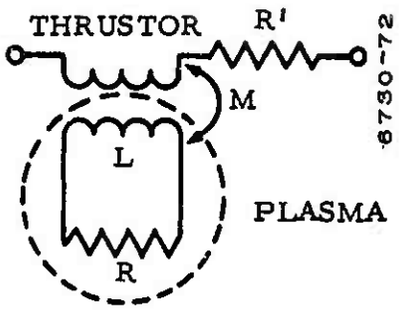

Figure 4-5. Circuit Diagram of Thrustor Inductively Coupled to Plasma

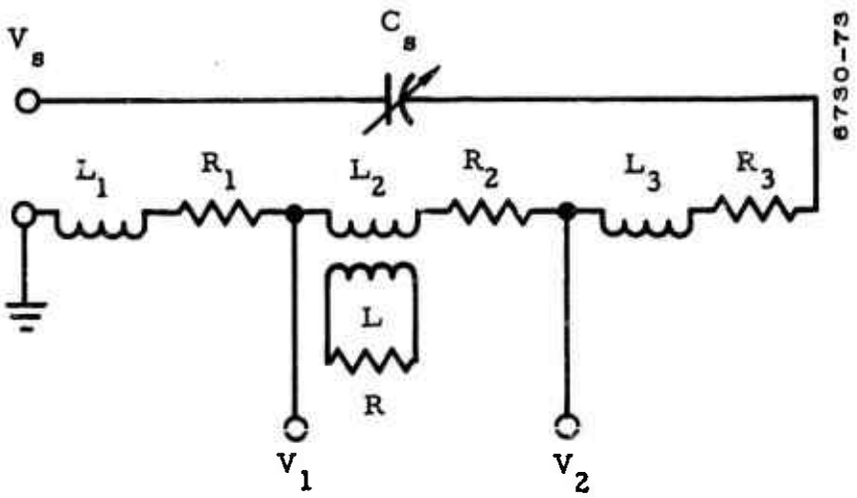

Figure 4-6. Thrustor Tuning Circuit

losses of the thrustor coils plus the power delivered to the plasma which appears as an equivalent resistance R':

$$V_2 = V_1 + j\omega L_2 I_L + I_L (R_2 + R')$$

The series resonant voltage V_S is the sum of all inductive and resistive voltages minus the voltage drop across the tuning capacitor, which cancels the inductive components, as indicated by the vector diagram in Figure 4-7. From this diagram it is clear that

$$V_S = I_L (R_1 + R_2 + R' + R_3)$$

when C_S is adjusted so that all inductive components are exactly cancelled. This condition is identified by two indications: the phase angle θ is 90°, and the absolute magnitude of V_S is a minimum. Then the power dissipated in the circuit is

$$W = V_S I_L = I_L^2 (R_1 + R_2 + R' + R_3).$$

Now R_1 is very small and negligible in comparison with the other resistance, R_2 and R' are the quantities of interest which must be measured, and R_3 (the resistance of the ballast coil) must be known and subtracted from the total to obtain the power actually delivered to the thrustor.

The value of R_3 at 240 KHz was accurately measured by a calorimetric method: the actual power dissipated in the coil was measured in the cooling water for a series of values of I_L up to 40 amperes, and the equivalent R_3 computed, with the result

$$R_3 = 0.281 \text{ ohm.}$$

Therefore, the power delivered to the thrustor is

$$W_S = V_S I_L - 0.281 I_L^2$$

It should be noted that the power dissipated in R_3 does not appear in the measurement of power with the $I_L V_L \cos \phi$ method, because the phase of V_L is measured at the terminal of L_2 and is not affected by R_3.

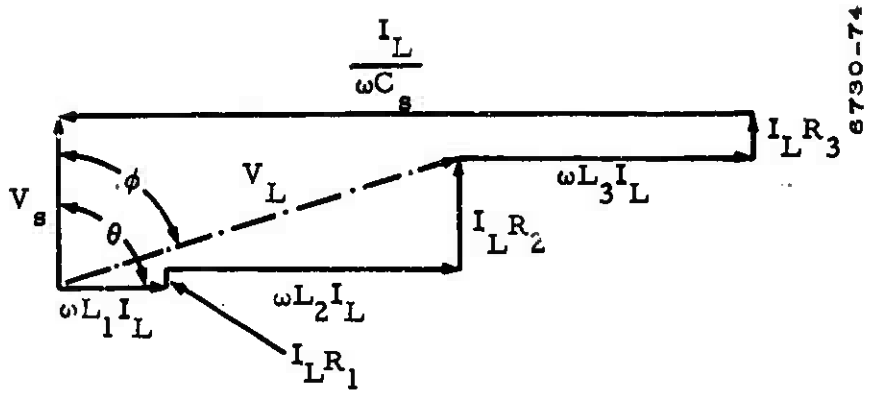

Figure 4-7. Vector Diagram of Voltages at Resonance

The most sensitive indicator of the correct tuning of C_S was found to be the phase angle θ. Both θ and ϕ are instrumented and recorded on two traces of a Sanborn recorder; a reading is considered valid only when θ is close to 90°.

4.4 ERROR ANALYSIS

Two independent methods are now available for the measurement of the power delivered to the load: the product of V_S and I_L, and the product of V_L, I_L, and cos ϕ. The current I_L is common to both methods, but the other quantities are separately measured by independent instruments. The probable accuracy of the power measurement can be computed as follows:

For the series resonant method we have, taking into account the correction for the resistance of the ballast inductor,

$$W_S = V_S I_L - 0.281 I_L^2$$

Accordingly, the absolute value of the expected maximum value of the error in W_S is

$$|\Delta W_S| = V_S |\Delta I_L| + I_L |\Delta V_S| - 0.562 I_L |\Delta I_L|$$

$$= (V_S - 0.562 I_L) |\Delta I_L| + I_L |\Delta V_S|$$

The electrical power is also measured as the product of the coil current, the coil voltage and the cosine of the phase angle

$$W_\phi = V_L I_L \cos \phi = V_L I_L \sin \psi$$

where $\psi = 90° - \phi$ is the angle actually measured by the phase meter as it is inserted in the circuit. In a similar manner, the absolute value of the expected maximum error in W_ϕ is

$$|\Delta W_\phi| = V_S \sin \psi |\Delta I_L| + I_L \sin \psi |\Delta V_L|$$

$$+ V_L I_L \cos \psi |\Delta \psi|$$

If equal weight is given to the two measurements of electric power, the most probable value is the mean of the two

$$\overline{W}_e = \frac{W_s + W_\phi}{2}$$

and the maximum probable error is the rms of the maximum expected contributions due to the independently measured parameters: V_S, V_L, I_L, ψ. Note that I_L is common to both expressions, whereas the other parameters are not. Therefore the contribution due to the maximum expected error in I_L is the mean of the contributions to the W_S and W_ϕ cases taken before squaring.

$$W_e = \frac{1}{\sqrt{2}}\left\{\left[I_L \sin\psi\,|\Delta V_L| + I_L V_L \cos\psi\,|\Delta\psi|\right]^2 + \left[I_L\,\Delta V_S\right]^2 + \left[(V_L \sin\psi + V_S - 0.562\,I_L)\,|\Delta I_L|\right]^2\right\}^{1/2}$$

The limits of measurement accuracy can be taken as:

$$|\Delta V_L| = 0.01\,V_L + 20 \text{ volt}$$

$$|\Delta V_S| = 0.01\,V_S + 2 \text{ volt}$$

$$|\Delta I_L| = 0.01\,I_L + 0.2 \text{ ampere}$$

$$|\Delta\psi| = 0.5 \text{ degrees}$$

and the true value of W_e can be expected to be between

$$\overline{W}_e - \Delta W_e < W_e < \overline{W}_e + \Delta W_e$$

ΔW_e is an upper limit to the error and can be taken as perhaps three times the standard deviation of the measurements. We can indicate for brevity the upper and lower limits of the measurements with

$$W_e^+ = \overline{W}_e + \Delta W_e$$

$$W_e^- = \overline{W}_e - \Delta W_e$$

and

$$W_e^- < W_e < W_e^+$$

$$W^{\pm} = \overline{W}_e \left(1 \pm \frac{\Delta W_e}{\overline{W}_e}\right)$$

Similarly we can compute the upper and lower limits for the measurement of the mean exhaust velocity $\bar{v}$, the beam kinetic energy W_k and the efficiency η:

$$\bar{v} = \Gamma/\dot{m}$$

$$\bar{v}^- < \bar{v} < \bar{v}^+$$

$$\bar{v}^{\pm} = \bar{v}\left[1 \pm \sqrt{\left(\frac{\Delta T}{T}\right)^2 + \left(\frac{\Delta \dot{m}}{\dot{m}}\right)^2}\right]$$

$$W_k = T^2/2\dot{m}$$

$$W_k^- < W_k < W_k^+$$

$$W_k^{\pm} = W_k\left[1 \pm \sqrt{\left(\frac{2\Delta T}{T}\right)^2 + \left(\frac{\Delta \dot{m}}{\dot{m}}\right)^2}\right]$$

$$\eta = T^2/2\dot{m}\, W_e$$

$$\eta^- < \eta < \eta^+$$

$$\eta^{\pm} = \left[1 \pm \sqrt{\left(\frac{2\Delta T}{T}\right)^2 + \left(\frac{\Delta \dot{m}}{\dot{m}}\right)^2 + \left(\frac{\Delta W_e}{W_e}\right)^2}\right]$$

ΔT can be taken to be 0.03 newton and $\Delta\dot{m}/\dot{m}$ is essentially negligible, however, it has been taken as 0.01.

The computation of the upper and lower limit of each performance parameter for each set of measurement involves much laborious arithmetic. The small digital computer available in the laboratory has been programmed to compute and print out the following quantities:

$$\bar{v}^+,\ \bar{v}^-,\ W_k^+,\ W_k^-,\ W_s,\ W_\phi,\ W_e^+,\ W_e^-,\ \eta^+,\ \eta^-$$

given the inputs of the measured $\dot{m}$, T, V_s, V_L, I_L, and ψ. Thus, it is possible to obtain the upper and lower limit of each performance parameter within minutes after measuring the data.

It is also possible to verify at a glance that W_s and W_ϕ, two independent measurements of the same quantity W_e, fall within the expected maximum error of each other and of their mean $\overline{W}_e$.

It should be noted that the instrumentation, the measurement and the computation are simple and straightforward if the electrical quantities to be measured are sine waves of constant frequency. However, the plasma coupled to the inductance of the thrustor is a nonlinear load and harmonics are generated in the circuit. The series-resonant circuit presents a low impedance to the fundamental current for which it is tuned, but a high impedance to the harmonic frequencies; therefore even a small percentage of harmonic current in the coil causes an appreciable distortion of the voltage waveform appearing at the V_S terminals. Furthermore, a distorted waveform creates problems in the phase measurements. This fact must be taken in account and a suitable filter added to the signal-processing circuits.

5. CONSTRUCTION

5.1 GENERAL

The copper coil must be protected from contact with the mecury vapor (plasma) for two reasons:

1. The mercury vapor, when condensing on the copper, alloys with it resulting in quick destruction of the coil.
2. The conductive plasma shunts the inductance of the coil and results in turn-to-turn and turn-to-ground arcs which also can destroy the coil.

The protective material must be, therefore, a good electrical insulator, compatible with mercury vapor, capable of withstanding very high temperatures where it comes in contact with the plasma. In addition, it must be capable of forming on the copper coil without leaving voids and without cracking either during the cure or during operation. A general requirement, also, is that the thermal expansion coefficient of the insulating material should match that of copper, if possible; or otherwise, that the insulating material should be strong enough to cause plastic flow of the (annealed) copper without cracking.

The required characteristics, taken together, appear to describe a castable ceramic of which several are on the market. A preliminary screening of those listed in the commercial literature restricted the choice to several sold by Sauereisen and by Aremco; a final screening based upon tests of samples eliminated all but the Aremco Ceramacast 505. This material, although superior to all other available materials (including the PT 209 ceramic used in Contract AF 33(657)-8697) under the conditions of the tests, still was not entirely satisfactory under actual service conditions; but it did provide a starting point for the development of a material composition and a casting process that eventually produced satisfactory coils.

The first problem was shrinkage during setting and cure. Shrinkage is a common characteristic of all physical systems undergoing a hardening transformation. When a rigid object, such as the copper coil, is embedded in the shrinking material, stresses develop which may or may not result in cracks depending as the curing process develops sufficient strength after or before most of the shrinkage takes place. In the case of the ceramacast 505 the shrinkage (about 1 percent) occurred before adequate strength was developed, and fine hairline cracks remained in the ceramic after cure. The cracks extended to the copper, and caused arcs when the thrustor was fired. A first and basic improvement in occurrence of initial cracks was obtained by the use of a pre-cast and pre-cured base for the coil, in the form of a thin ceramic wafer over which the main casting was poured. This backbone provided a nonshrinking support for the ceramic during the cure as well as a flawless surface on the side facing the plasma. Yet cracks could still develop on the opposite face of the coil.

The problem of shrinkage was minimized by adding to the composition an inert, granular filler (tabular alumina) so as to occupy most of the volume with a non-shrinking component and to restrict the domain of the shrinking component to the interstices between granules where it could perform a binding function without changing the distances of the granules greatly. If the mixture could be so proportioned that the granules would fill exactly all the remaining space, a non-shrinking composition would result.

It was found, however, that before this condition could be obtained, air would remain trapped in the interstices between granules. Minute air bubbles embedded in the solid ceramic would appear at first sight essentially harmless, and so they are if the dielectric stress applied to the ceramic is dc or at a low frequency. If, however, the applied voltage is at a sufficiently high frequency, the air in the bubble can ionize. The concentrated heat, possibly combined with wall bombardment by the ions oscillating in the applied alternating field, slowly enlarges the cavity of the original bubble and extends it in some direction presumably determined by local weaknesses of the ceramic as well as by the direction of the applied field. The result is a "worm hole" that eventually, after many hours of slow progress, reaches either a copper surface or the external surface of the ceramic; the result of this is a catastrophic arc after an extended period of satisfactory operation. Such "worm holes" were found in all the coils that failed, after many hours of operation, with an applied voltage, at the time of failure, no higher or appreciably lower than the voltage they had successfully carried at various times

before. Some coils, to be sure, failed by direct breakdown at a weak spot: but this happened quickly, while voltage was being increased, the first time that sufficient voltage for breakdown was reached. In all cases of direct breakdown there was either a crack or insufficient thickness of insulation due to eccentricity of the coil in the mold.

The incidence of minute bubbles was reduced by mounting the mould on a vibrator and by shaking the mixture while it was being poured. This procedure did not, however, permit the use of a mixture containing enough granular alumina to eliminate shrinkage without retaining a few bubbles. It was found that the addition of a small quantity of sodium silicate to the mixture allowed the use of a much higher percentage of granular alumina, to a point where shrinkage was essentially cut to zero. The sodium silicate apparently acts as a lubricant at the points of contact of the hard granules, and permits closer packing under vibration; it also acts as supplementary binding agent between the solid particles and increases the mechanical strength of the casting.

The glassy characteristics of the sodium silicate have a detrimental effect, however, because the drying of the casting is delayed. Castings containing only Ceramacast 505 and tabular alumina appear to have such a combination of porosity and capillarity that they dry essentially uniformly throughout their cross-section. A series of sample ingots cast together and broken at various intervals, showed that the interior was becoming progressively and uniformly dryer as time went by, so that they could be cured in the oven, as specified by the manufacturer of the Ceramacast 505, about 36 hours after casting. Similar samples containing sodium silicate developed a hard, impervious crust that kept the interior quite wet and made a cure impossible for many days. Attempts at curing the casting before it was sufficiently dry resulted in the evaporation of the liquid inside the crust with consequent "puffing" of the coil like leavened bread.

It was possible in the end to find a compromise between the percentage of sodium silicate in the composition and the drying/curing schedule such that adequate coils could be produced in a reasonable time. The ceramic composition was further improved by using two mesh sizes of tabular alumina (analogous to the sand and the gravel in concrete) and by adding a small percentage of chopped quartz fibers for checking crack propagation. Since each coil required several weeks for its fabrication, and many days of testing before its quality could be fully assessed, any useful feedback of information to the manufacture of coils had a built-in delay

of several weeks. At the end of the program both the ceramic composition and the manufacturing process were adequate but not necessarily optimum. The coils made near the end of the program survived testing at a sufficiently high voltage and for a sufficient length of time to fulfill some of the requirements of the experimental thrustor program. The ultimate limits of coil quality and thrustor performance have not, however, been reached, and further progress can be expected from a continued study of the properties of ceramic aggregates of the type so far used.

5.2 RADIATION-COOLED COILS

The Statement of Work required an investigation of the possibility of operating the thrustor in a radiation-cooled mode, without water circulation. There are some basic differences between the radiation-cooled thrustor and a water-cooled one. A water-cooled coil consists of a copper tube, in which the water flows, covered by a layer of insulating material. The outer surface of the insulating material is exposed to the hot plasma, and is heated by radiation and plasma bombardment. The electric current heats the copper wire in proportion to its resistance. Under steady state conditions the temperature of each element will be such that the total power received is equal to the total power lost (power and heat are here used interchangeably). Power sinks are the flowing water and external space. The inner wall of the copper tube can be assumed at the temperature of the water. The outer surface of the coil will take the temperature which will radiate (according to $A\sigma T^4$) the net amount of power difference between the power delivered by the plasma and the power delivered by conduction to the copper and hence to the water; therefore the temperature profile inside the coil will be as shown in Figure 5-1. A temperature gradient is established in the insulating material with the highest temperature at the surface. The case of the radiation cooled coil is entirely different. The only sink is external space; therefore the outer surface must assume a temperature at which it radiates the sum of the power input from the plasma and the power input from the copper; all other things being equal, therefore the surface temperature must be higher than in the water-cooled case; in addition, a temperature gradient must be established so that the heat developed in the copper by I^2R losses can be delivered to the surface, and this is in the opposite direction to that of the water-cooled case. Therefore the temperature of the copper must be higher than the temperature of the surface. The situation is illustrated in Figure 5-1. It is clear that in the radiation-cooled case temperatures are everywhere much higher than in the water-cooled case, so that one likely mode of failure is the melting

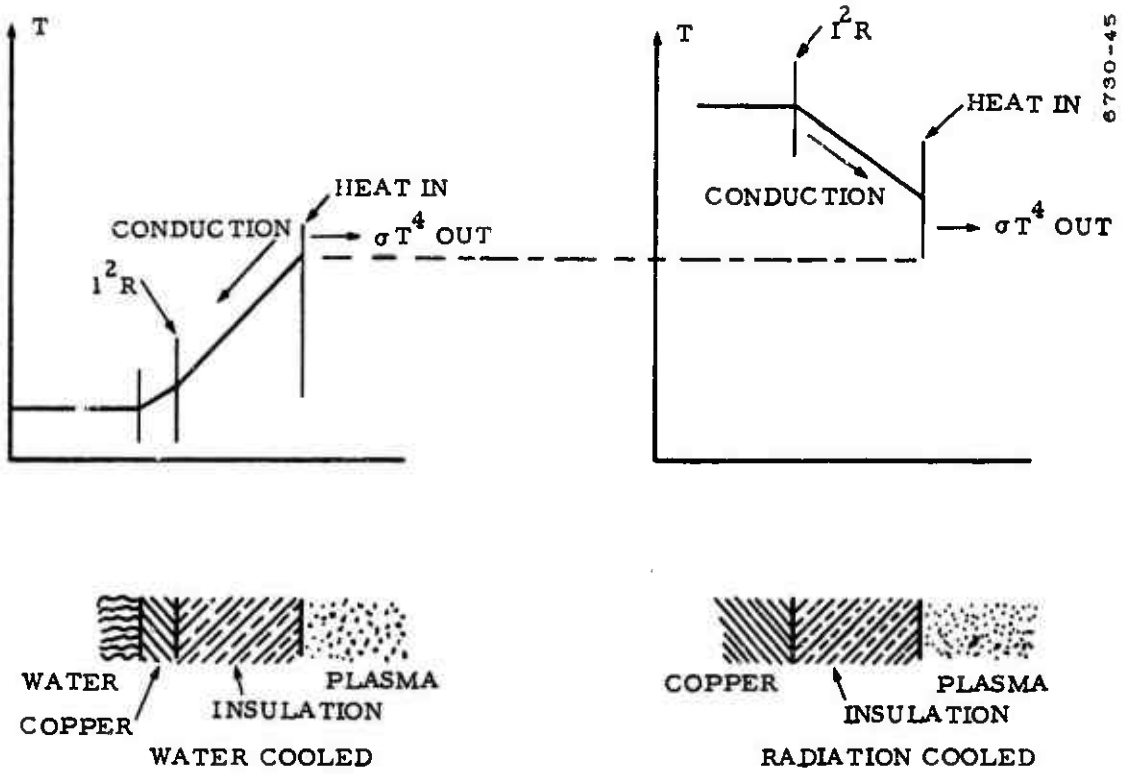

Figure 5-1. Temperature Diagrams of Water- and Radiation-Cooled Coils

of the copper; in addition, the stresses on the insulation are such that it may tend to crack because the outer layers are stressed in tension by the hotter, expanded inner layers. For this reason it is important that the material used has high mechanical strength and high thermal conductivity. High thermal conductivity can be obtained by the substitution of granular beryllia for the granular alumina in the aggregate. This was not done, however, during the past period because beryllia is much more expensive than alumina. It was decided to carry out all experimental development work with the cheaper alumina until a composition is found to be mechanically satisfactory (minimum shrinkage, no cracks, no air intrusions, etc.). At this point beryllia can be substituted volume for volume in the aggregate. The shift to water-cooled coils made this phase of the program unnecessary. To summarize, the radiation-cooled coil has in common with the water-cooled coil the following modes of failure:

1. Immediate breakdown, upon first application of voltage in the case of pre-existent cracks or pinholes exposing the copper to the plasma.
2. Delayed breakdown due to air inclusions which grow to "worm holes."
3. Direct voltage breakdown when the voltage gradient exceeds the dielectric strength of the insulation. This happens when the voltage is increased for the first time to a sufficient level in the case of thin or partially cracked insulation.

In addition, the radiation-cooled coil has the following peculiar modes of failure:

4. Cracks may develop due to the expansion of the copper and inner ceramic layers against the outer layers as the internal temperature increases.
5. If a sufficiently high temperature is reached without cracks, the copper may melt.

Early experiments were carried out in a bell jar to determine the operating temperature that could be expected in a radiation-cooled coil. A number of coils were tested with low frequency (60 cycles) power, whereby voltage and current could be accurately measured by standard instruments, and surface temperatures could be measured by thermocouples without the problems attendant to the induction heating of the thermocouples themselves by high frequency fields. The results are shown in Figure 5-2; also shown for reference is the slope proportional

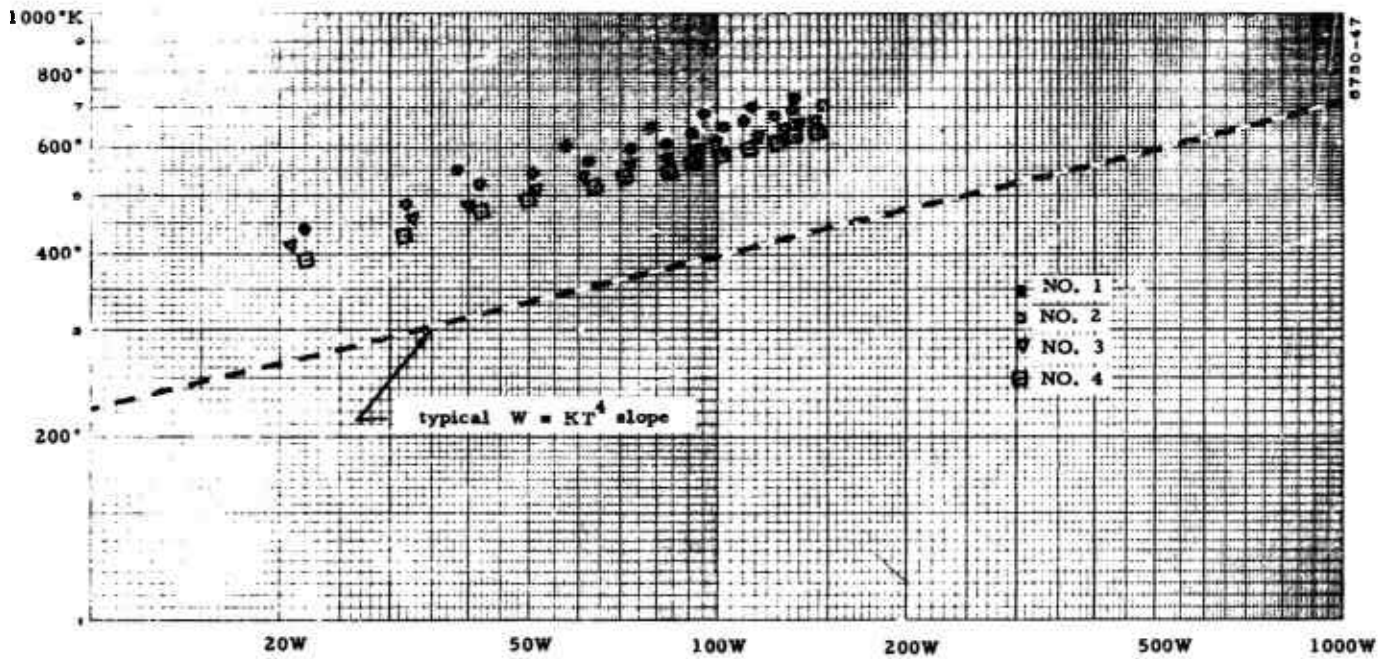

Figure 5-2. Coil Temperature as a Function of Input Power

to T^4. It appears that the heat loss from the coil was entirely governed by radiation, since the slope of the observed points is closely parallel to the slope of T^4. A computation of the radiated power per unit area of coil surface showed that the composition used (straight Ceramacast 505) had an emissivity close to that of a black body for the infrared wavelengths involved. The experiment also showed that the operating temperature of a coil could be expected to be in excess of 600°K, and probably close to 800°K. All the coils tested developed cracks that would have led to failures of type 4 if the applied voltage had been high enough; this was taken as an indication that the ceramic insulation lacked the mechanical strength to withstand the forces exerted by the expanding copper (similar tests, repeated later with an improved ceramic composition, resulted in melting the copper tube in its ceramic envelope without cracking the ceramic; the composition used was that tabulated in Table 5-1 opposite coils 39 and 40).

The same series of tests was used to measure the resistivity of the copper when hot. The results are shown in Figure 5-3; also shown is the resistance change as given by the handbook. This information was used for computing the ohmic losses of the coils in Section 2.2.

During the course of the development program, the gradually improving materials and techniques shifted the normal mode of failure from type 1 to type 2 to type 3. Type 4 may have occurred once or twice. Type 5 was not observed; but tests on copper tubes embedded in ceramic samples of more advanced composition were melted by the passage of heavy currents without breaking the ceramic as mentioned above.

Every coil was given a serial number from the time fabrication was started, and a detailed record of every step of the procedure was kept for reference against performance. Because of the long delay in information on feedback, however, the benefits of experience could not be applied to serially successive coils, and blocks of coils were produced that upon test behaved in rather similar fashion. This had the disadvantage that progress was necessarily slow, but on the other hand the advantage that a small amount of statistics could be collected to prevent undue influence of freak failures.

It was thus found that inner coils were much more vulnerable than outer coils, and that an outer coil would outlast several inner coils. Thus it happened that several outer coils, produced early in the program, remained available as spares to the end, and were never used; and soon production of outer coils was stopped altogether and all efforts were

TABLE 5-1

COMPOSITION OF COILS

Serial No.	Type	Cooling	Composition						Failure Mode	Life		
			1	2	3	4	5	6		Hr	Min	Sec
18	Inner	Radiation	100	80				22	I			5
19	Outer	Radiation	100	80				22	*	8	33	45
20	Outer	Radiation	100	90				22	2	70	15	15
21	Inner	Radiation	100	100				23	1	8	33	1
22	Inner	Radiation	100	100				22	2	7	42	58
23	Inner	Radiation	100	100				22	1		50	47
24	Inner	Radiation	100	100				22	2	1	13	37
25	Outer	Radiation	Dented – Not completed									
26	Outer	Radiation	100	105				22	***			
27	Outer	Radiation	Dented – Not completed									
28	Inner	Radiation	100	105				22	***			
29	Outer	Radiation	100	170		35		10	***			
30	Inner	Radiation	100	170		35		10	2	1	30	23
31	Inner	Radiation	100	170		35		10	2	1	30	44
32	Inner	Radiation	100	170		35		10	2	2	46	54
33	Inner	Radiation	100	170		35		10	3		10	36
34	Inner	Water	70	85	50			33	2	59	34	18
35	Outer	Water	70	95	50	6	2	31	**	100	48	26
36	Outer	Water	70	120	60	8	4	30	***			
37	Inner	Water	70	95	50	6	2	31	3	14	49	21
38	Inner	Water	70	95	50	6	4	31	3		3	46
39	Inner	Water	70	120	50	8	4	31	*	53	03	55
40	Inner	Radiation	70	120	60	9	4	30	***			
41	Inner	Water	70	130	65	10	4	29	3	33	51	29

Ingredients

1 Ceramacast 505
2 Tabular Alumina 14-24 Mesh
3 Tabular Alumina 60-80 Mesh
4 Sodium Silicate Solution Robinson 1583
5 Chopped Quartz Fibers, 1/4" Long
6 Distilled Water

*No failure, retired because of mechanical reasons.
**No failure.
***Not used. Available as a spare.

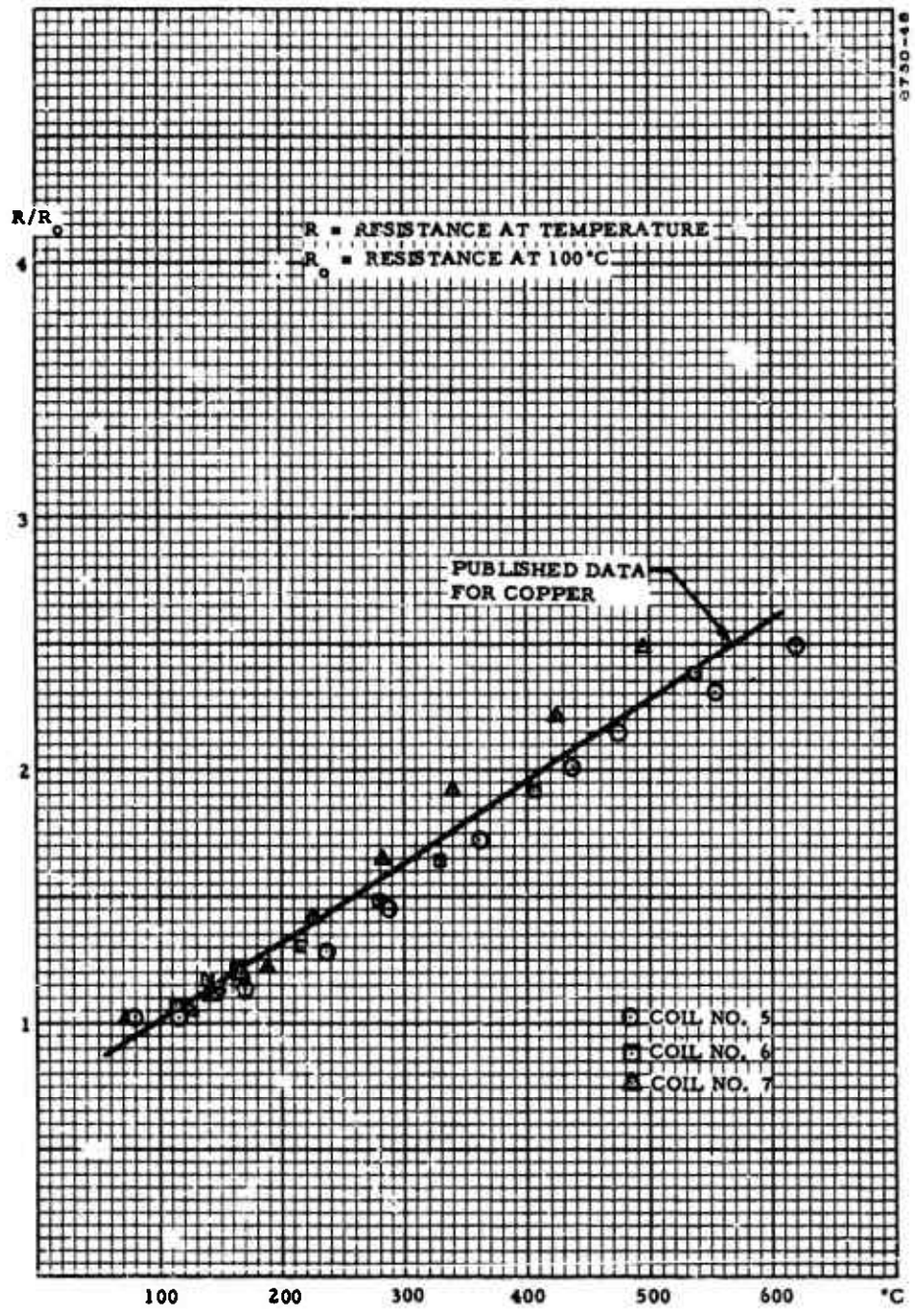

Figure 5-3. Copper Resistance as a Function of Temperature

devoted to the production of inner coils. Consequently the outer coils in service at the end of the program reflect materials and techniques not as refined as those used in the corresponding inner coils. Table 5-1 is a summary of the materials used in the series of radiation-cooled coils that were tested with significant results (excluding early coils that were subjected to preliminary tests only and not used in an operational thrustor). The quantities shown as ingredients are proportional units of weight (grams) except the quantity of sodium silicate, which is given in milliliters of saturated solution in water.

The life times shown in the last columns are for reference only. The lifetime is significant only when considered in conjunction with the power level at which the coil was operated, and in particular, with the current (determining I^2R losses and therefore temperature) in the case of radiation-cooled coils, and voltage (determining diselectric stress) in the case of water-cooled coils. This information is presented in Table 5-2, which shows the chronological sequence of the use of the coils in an operational thrustor. Tables 5-1 and 5-2 show in their proper places the water-cooled coils which were built in sequence with the radiation-cooled ones.

5.3 WATER-COOLED COILS

During much of the program the emphasis of the development effort was directed towards obtaining steady-state, long duration operation of the radiation-cooled thrustor, with the specific objective of 100 hours life. Before this objective could be reached the effort was re-directed towards obtaining the highest possible efficiency rather than the longest life time; and since efficiency could be made higher by using higher currents in the coils, water-cooled coils were called for rather than radiation-cooled ones.

The severe operating conditions of the radiation-cooled thrustor were such that the materials were subjected to an equivalent accelerated life-testing for the structures in the water-cooled mode, so that a vastly improved technology for building water-cooled thrustors was available when needed. This was proved by the fact that the thrustor was operated in the water-cooled mode at more than twice the voltage used in the radiation-cooled mode (and more than twice the current); the outer coil did not fail, and of the two inner coils used one did not fail and the other failed by direct breakdown (mode 3) at a point of weakness due to an assembly error which resulted in a localized lack of insulation inside one of the supporting ceramic legs; the failure happened at the highest voltage ever used in this series of tests.

TABLE 5-2

CUMULATIVE RECORD OF THRUSTOR FIRING

Date	Inner Coil				Outer Coil				Maximum Stress	
	Serial No.	On Time			Serial No.	On Time				
		Hr	Min	Sec		Hr	Min	Sec	Ampere	Kilovolt
10 April	22	0	05	55	19	0	05	55		
11 April		1	05	52		1	05	52	12.1	0.800
12 April		4	20	22		4	20	22		
13 April		6	18	51		6	18	51	12.0	0.750
14 April		7	22	58		7	22	58	16.0	1.200
4 May		7	29	54		7	29	54	18.2	1.000
5 May		7	31	13		7	31	16	19.5	1.140
7 May		7	42	58*		7	42	58	17.9	1.000
12 May	23	0	04	20		7	47	18	22.5	1.350
14 May		0	17	59		8	11	07	22.3	1.300
15 May		0	50	47*		8	33	45**	22.0	1.250
22 May	24	0	26	00	20	0	26	00	18.5	1.140
23 May		1	13	37*		1	13	37	17.0	1.060
1 June	30	1	30	23*		2	44	00	16.0	1.000
6 June	31	0	09	30		2	53	30	17.0	1.070
7 June		1	30	44*		4	24	14	16.5	1.000
9 June	32	1	4[illegible]	19		6	13	33	18.0	1.120
10 June		2	43	54*		7	15	09	16.8	1.050
12 June	33	0	10	36*		7	25	45		
19 June		0	31	51		7	58	36	18.3	1.130
20 June		3	49	05*		11	14	50	17.2	1.100
24 June	34	1	42	47		12	57	37	17.2	1.100
25 June		14	32	21		25	47	22	16.8	1.000
26 June		29	55	15		41	10	16	17.5	1.000
27 June		48	45	00		60	00	01	15.4	0.950
28 June		59	34	14		70	15	55*	14.5	0.850
5 July		59	34	18*	35	0	00	04		
7 July		4	16	07		4	16	11		
8 July	37	14	49	21*		14	49	25	17.5	1.100
9 July	38		3	46*		14	53	11		
11 July	39	2	01	04		16	54	16		
12 July		20	11	47		35	04	59	23.3	1.410
13 July		42	39	34		57	32	46	27.0	1.670
14 July		53	03	45**		66	56	57	30.0	1.850
26 July	41	5	04	01		72	00	58	29.0	1.770
27 July		16	16	01		83	12	58	34.0	1.980
28 July		27	28	01		94	24	58	37.0	2.130
29 July		33	51	29*		100	48	26	43.0	2.400

*Failure.

**No failure. Removed for other reasons.

The procedure for making a water-cooled coil of the latest type comprises the steps listed below.

1. Annealed copper tube (0.125" o.d., 0.012" wall) is bent and formed to shape in an aluminum mold (Figure 5-4). The strains and the work hardening due to the bending of the tube are removed by annealing again the tube in the mold.
2. The formed tube is removed from the mold and 0.250" diameter feed-lines are brazed to the terminals of the coils. The assembly is chemically cleaned, leak checked by helium leak detector, pressure tested at 80 psi, and cleaned again. Coils at this stage are shown in Figure 5-5.
3. The coils are dipped in a slurry of Ceramacast 505 with added sodium silicate to build up a first, closely adherent layer. The layer is dried, cured and carefully inspected for flaws, breaks, bubbles or lack of adherence.
4. Inner coils are small, compact and self-supporting; individual turns do not tend to sag and touch each other. Outer coils are limber so that turns may touch. Outer coils are dipped again and the process repeated until a sufficient thickness of insulation is built up to insure turn-to-turn insulation during the casting process.
5. A 0.060" - 0.080" thick ceramic wafer is cast in the bottom of the casting mold (see Figure 5-6). The wafer is vibrated, dried 24 hours, and cured 24 hours at 95°C.
6. The coil is suspended and centered in the mold above the wafer. Precise positioning is required to avoid shifts of location that result in thin ceramic walls and consequent danger of direct breakdown.
7. Three ceramic (Mullite) tubes are positioned so that their ends will be embedded in the casting. The tubes serve as mechanical supports of the coil in the thrustor and are located in standarized positions so that all coils are mechanically interchangeable.
8. The ceramic aggregate is poured, vibrated, air-dried 36 hours, cured at 50°C for 36 hours and at 95°C for 48 hours.
9. The coil is pulled from the mold. The feedlines are trimmed to length and coated with Silastic RTV 891. Three coats are

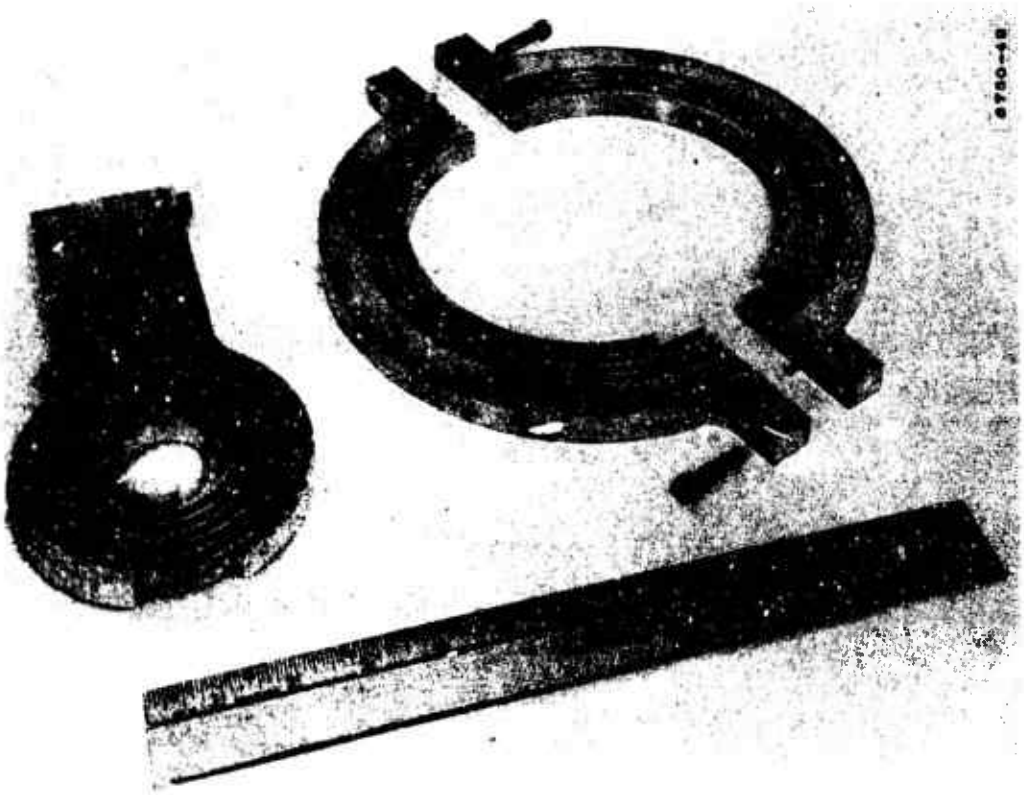

Figure 5-4. Aluminum Molds for Forming Coils

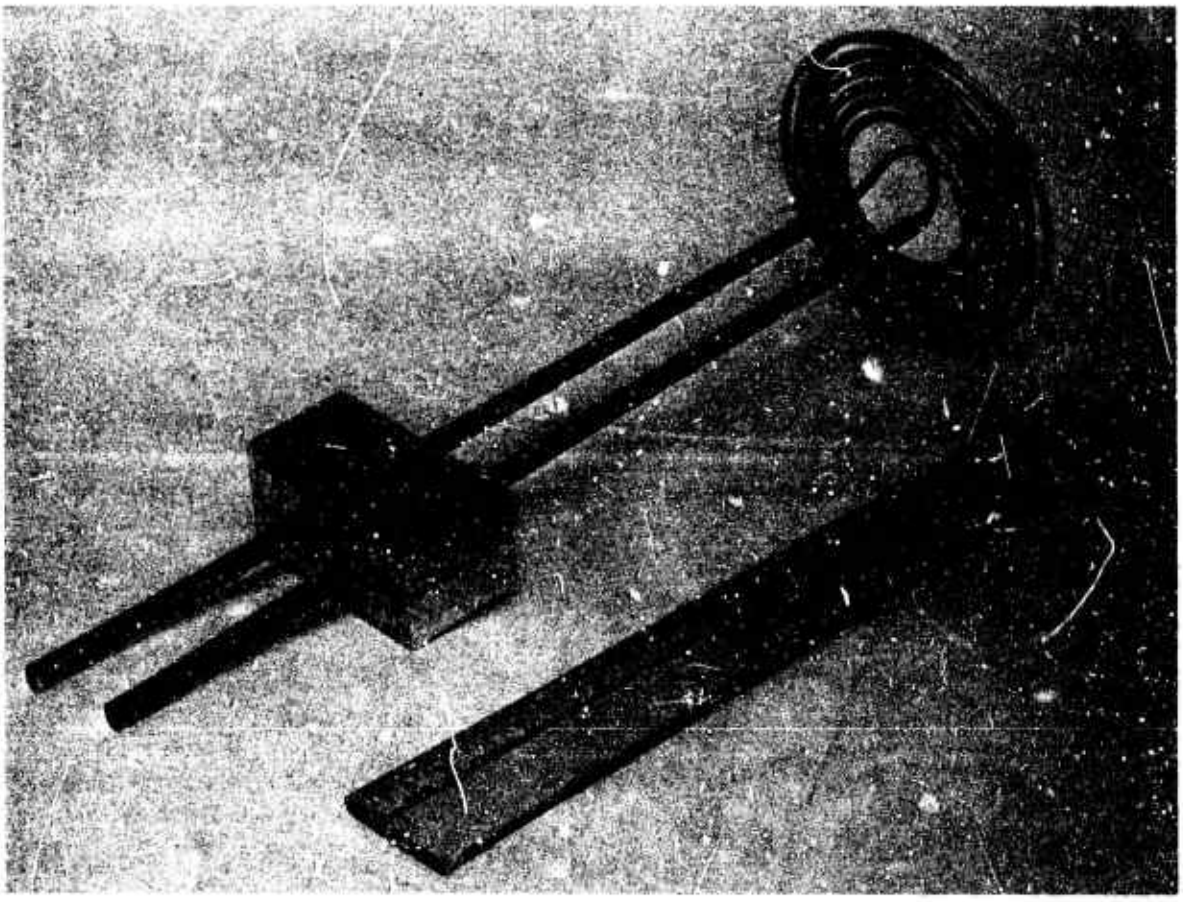

Figure 5-5. Formed Coil With Feed-Lines

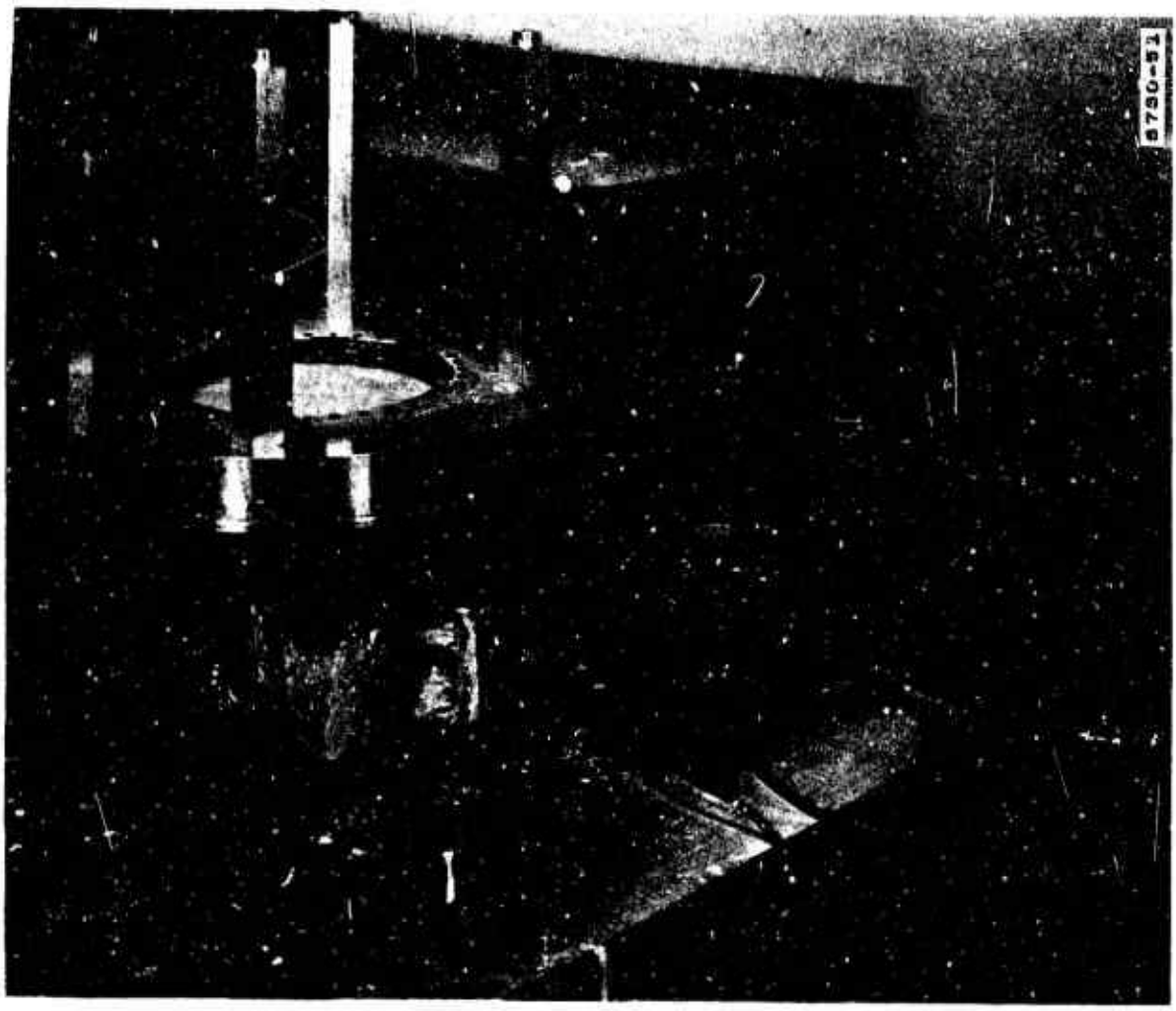

Figure 5-6. Ceramic Wafer in Mold, Mold on Vibrator

applied at intervals of no less than ten hours to insure complete cure of the preceding layer. Swagelock fittings are attached to the feedlines.

10. The coil is baked 12 hours at 150°C.

11. The coil is weighed and stored with dessicant in a sealed container until needed.

Figure 5-7 shows an inner coil, an outer coil and the nozzle mounted on an assembly fixture for fitting the connecting leads. Figure 5-8 shows a complete thrustor mounted on the thrust stand.

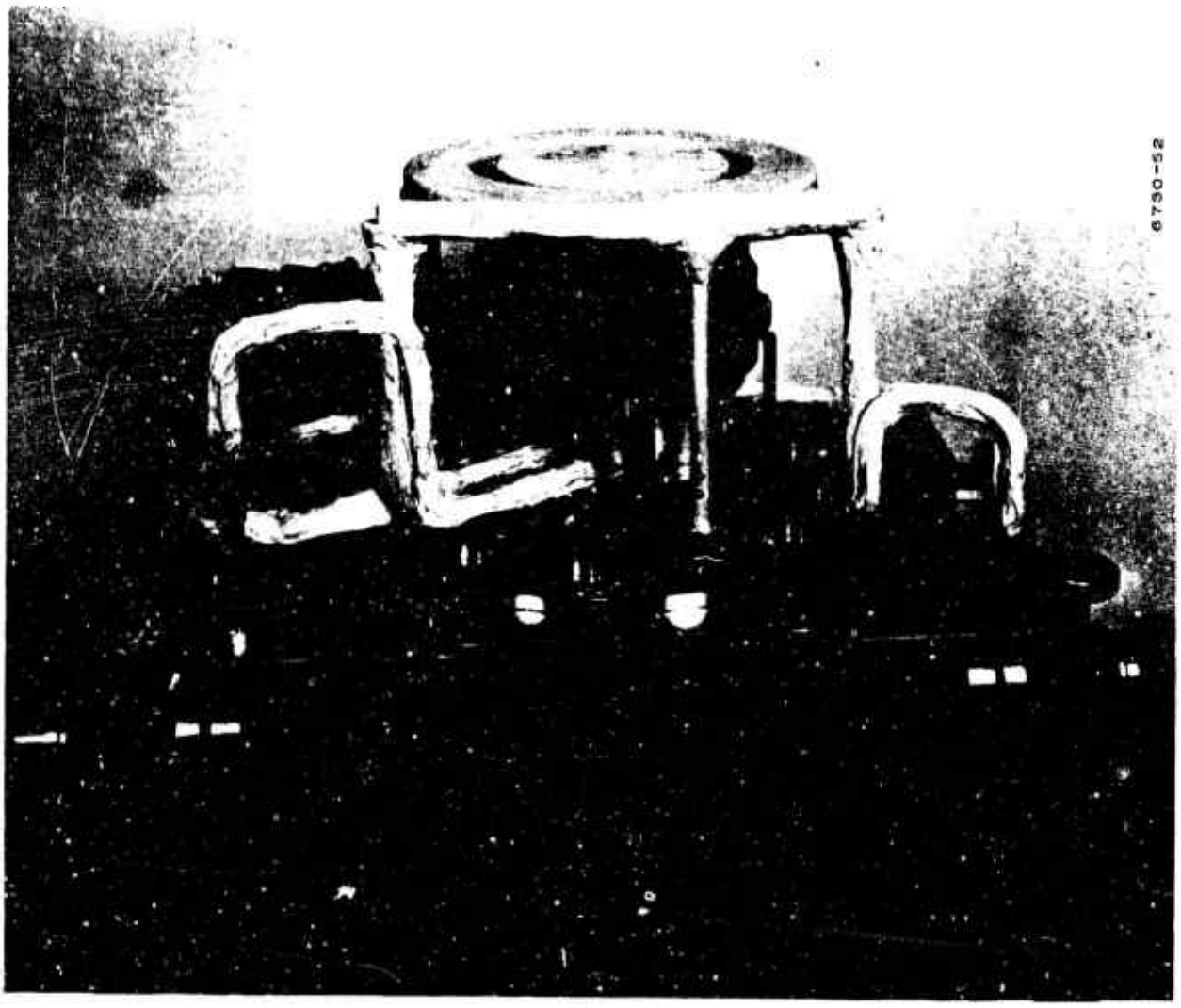

Figure 5-7. Thrustor on Assembly Fixture

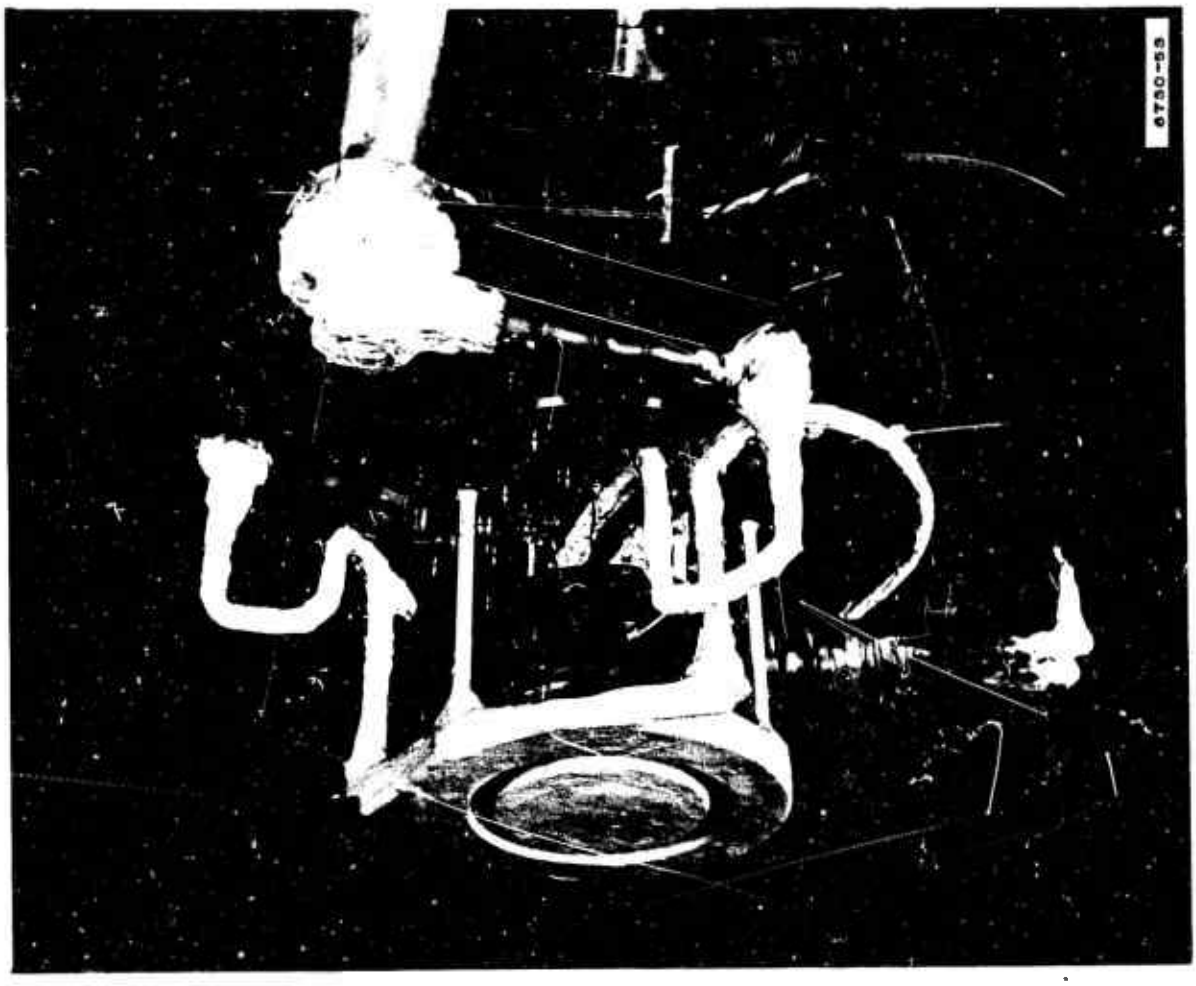

Figure 5-8. Thrustor Mounted on Thrust Stand

6. THRUSTOR PERFORMANCE

6.1 GENERAL

The Statement of Work required demonstration of thermal equilibrium for the validity of a performance measurement, mainly for the purpose of insuring that no mercury could condense in the feed system or evaporate from a previously condensed state so as to cause the thrustor to operate with an instantaneous mass flow different from that measured at the metering feed pump. This requirement was observed by noting that the thermal time constant for heating and cooling processes in the thrustor system is of the order of 15 minutes (temperatures are monitored by thermocouples at six points of the mercury feed system and two points of the platform), and by requiring no measurable change of temperature anywhere in the system for at least one hour before the time of an official observation.

It was observed, however, that as long as the temperatures were everywhere higher than the condensation temperature of mercury at the local mercury pressure, so that no condensation could occur anywhere in the mercury feed system between the boiler and the nozzle, then the measured thrust and electrical loading did assume their final value within seconds of a change of either mass flow, as determined by the metering feed pump, or of applied electric power; no changes could be measured thereafter for as long as mass flow and power were kept constant. Similarly, it was observed that the measured values were not affected by the duty cycle: the readings were identical whether the thrustor was fired for two seconds every minute, as it was done at the beginning of a run for outgassing the thrustor and the chamber, or for thirty seconds every minute, as it was done after several hours, when the outgassing process was well underway, or during continuous unlimited firing, as it was done when the chamber was fully outgassed (firing was interrupted for two seconds every minute to guard against drifts of the zero baseline of the performance recording system; thus the highest normal duty cycle was 96.7%).

It appears therefore that the practice of long firing periods at constant power and mass flow before a measurement could be accepted as valid was extremely conservative. Nevertheless this practice was observed in all measurements, because the concurrent goal of lifetime testing required that the thrustor be continuously fired for many consecutive days, so that time was available for long waits between changes of operating conditions. Only at the end of the radiation-cooled phase, when water-cooled coils were to be tested, the firing time required for acceptance of a measurement was slightly shortened, with the concurrence of the Air Force Project Officer, in order to provide a larger number of data points in the available time, since the emphasis was shifted from long life time to higher performance.

No difference in performance was observed between radiation-cooled and water-cooled thrustors over the range of operating parameters accessible to both modes. In fact, all measurements were extremely consistent and repeatable from unit to unit whenever the units were operated at the same mass flow and power level.

The range of operating parameters accessible to the thrustor was explored by maintaining a constant mass flow and varying the coil current I_L, or by keeping the current constant and varying the mass flow; the series resonant capacitor C_s was always tuned to provide an indicated phase angle $\theta = 90°$ and a minimum value of V_s. In general, for each new coil, input power was increased in steps, starting at a low value (of the order of two or three kilowatt) which was maintained during outgassing of the thrustor and chamber, and then increasing the coil current in steps of two or three amperes rms; the mass flow was changed in steps of no more than 10% and each setting was maintained through at least one timing cycle of the automatic mass flow measuring apparatus (see Report, Section 5. 3. 1).

This procedure resulted in a detailed map of the performance parameters over a range of mass flow between 0. 035 and 0. 16 grams/sec and power levels up to about 12 kilowatt. It was found that the most sensitive indicator of correct tuning was the phase angle θ and, to a slightly smaller extent, the phase angle ψ. Both angles responded promptly and distinctively to small changes of mass flow. Near the end of the program, after several thousand hours of operation, the metering pump in the mercury feed system showed some signs of wear: the cyclic cam lobe which drives the pump pistons developed a flat spot where the cam followers had some play. This play resulted in a small irregularity in the delivery of the

mercury to the boiler coincident with the passing of each piston from suction to delivery. The small transient periodic irregularities were detectable in the recorded traces of both phase angles but not in the recorded trace of the developed thrust nor of the other electrical parameters (voltages and currents). The effect was particularly obvious at the very low mass flows, where the transient irregularities represented a larger proportional fraction of the total flow.

All performance parameters were continuously recorded on two 8-channel Sanborn recorders. Recorder No. 1 recorded the following channels:

1. Thrust (newton)
2. Coil current I_L (ampere rms)
3. Coil voltage V_L (kilovolt rms)
4. Cos θ ($-1 < \cos \theta < +1$)
5. Series resonant voltage V_s (kilovolt rms)
6. Phase angle ψ (degrees)
7. Plate resonant voltage of transmitter V_B (kilovolt rms)
8. Plate current of transmitter I_B (ampere d. c.)

Recorder No. 2 recorded the following channels:

1. Chamber pressure by ion gauge (10^{-3} Torr full scale)
2. Foreline pressure by Thermocouple gauge
3. Plasma light output by photomultiplier
4. Analog signal of C_s capacitance
5. Spare
6. Eight multiplexed channels of water temperatures
7. Eight multiplexed channels of water temperatures
8. Eight multiplexed channels of thrustor temperatures

The normal operating procedure during the tests was as follows:

Every twelve hours, at midnight and noon, the paper was cut and the roll removed from each Sanborn recorder, and the data were analyzed during the following twelve-hour period.

The chart from Recorder No. 2 was examined first, and the following data transcribed on specially prepared forms and on standardized graphs:

1. On-off ratio (duty cycle) when less than 96.7%.
2. Total cumulative on time for the coil set assembled in the thrustor. These were taken from Channel 3, which indicated whether the plasma was actually ionized or not.
3. Thrustor temperatures.
4. Capacitance of tuning capacitor C_S.
5. Notes and comments written on the chart by the operator at the time of occurrence.

Inspection of the graphs showed the time periods in which the temperatures and other conditions were constant for the required long intervals, and such times were noted as potential sources of valid performance points.

The chart from Recorder No. 1 was examined next, and the drift of the thrust baseline was transcribed on the same graphs that were showing the thrustor temperatures (it was thus found that the long term drift of the thrust baseline did not correlate with the thrustor temperature, but with the ambient temperature and was due to the electronic circuits in the Instrument rack). Then the time periods previously noted for their uniform condition were examined in close detail, and if the electrical parameters were found to be equally uniform, the values were transcribed in another form as a potentially valid performance point. The final acceptance of the readings came after computation of the error limits and verification of the power readings W_S and W_ϕ. In this manner anywhere between one and eight points were collected each day.

6.2 EXPERIMENTAL DATA

Table 6-1 shows the measured, valid, performance points. The points are arranged in order of increasing mass flow, and for each mass flow, in order of increasing coil current. The event identification, listed for reference purposes, is built up by the month, day, (decimal point), hours and minutes of the record. The other columns are labeled by the symbols used in Section 4.4.

The information contained in Table 6-1 can be usefully presented in graphical form by transcribing the data in a suitable format. Figures 6-1, 6-2, and 6-3 present the value of as a function of T for three approximate values of the mass flow $\dot{m}$. Each point is represented by a rectangle limited by the maximum probable errors defined in Section 4.4, i.e., the top and bottom margins of the rectangle are $\eta+$ and $\eta-$, and the right and left margins of (T + 0.01) and (T - 0.01) newton.

From the point of view of a potential user, the most interesting presentation is that in the (T, $\bar{v}$) plane, where performance parameters are directly related to the desired mission requirements. Since $\bar{v}$, the average exhaust velocity, is defined as $\bar{v} = T/\dot{m}$, it is proportional to the specific impulse ($I_{sp} = \bar{v}/g$) so that the $\bar{v}$ axis can also be labeled with corresponding values of I_{sp}. By definition, the lines of constant $\dot{m}$ are fixed in the (T, $\bar{v}$) plane and are shown for reference. The following illustrations show contours of constant coil current I_L, coil voltage V_L, input power W_e, and efficiency η. When plotting the experimental points on the graphs it was found that the amount of smoothing required to generate regular curves was extremely small. In practically no event did a parameter fall more than one increment width away from the average locus of the parameter; for example, all points with I_L = 35 ampere fall between the locus of I_L = ampere and that of I_L = 37 ampere.

The trends which are apparent in the illustrations are unmistakeable; but the area so far covered lies below the transition to the high ionization efficiency observed at high power level under Contract AF33(657)-8697. Direct extrapolation of the data collected under that contract, with a correction applied for the lack of ferrites in the current configuration, indicated that a change of ionization efficiency can be expected in the range of coils current $50 < I_L < 90$ ampere. Currents in this range could not be reached with the radiation-cooled coils, but were being approached with water cooled coils at the end of the contract period. Point No. 03 was measured with the highest current (43 amperes), and was the last

TABLE 6-1

THRUSTOR PERFORMANCE DATA

Event No	Identif.	$\dot{m}$ gm/sec	T Newton	$\bar{v}^+$ Km/second	$\bar{v}^-$ Km/second	I_L Amp.	V_L Kv	W_e^+ Kilowatt	W_e^- Kilowatt	η^+ Percent	η^- Percent
01	729.1108	0.0353	0.21	6.843	5.048	36.5	2.20	8.631	7.463	10.16	5.35
02	729.1215	0.0353	0.23	7.410	5.614	41.0	2.15	10.341	9.031	9.92	5.54
03	729.1234	0.0353	0.32	9.960	8.160	43.0	2.40	12.061	10.539	15.51	10.14
04	727.0115	0.0381	0.18	5.555	3.893	27.4	1.75	5.247	4.506	11.85	5.58
05	727.0306	0.0381	0.20	6.080	4.417	32.7	1.95	7.063	6.095	10.56	5.38
06	729.0930	0.0421	0.23	6.201	4.705	37.0	2.20	8.383	7.222	10.33	5.75
07	729.0830	0.0421	0.25	6.684	5.179	38.0	2.25	8.922	7.697	11.27	6.56
08	726.2230	0.0439	0.18	4.811	3.371	29.0	1.71	5.604	4.865	9.52	4.49
09	727.0706	0.0446	0.21	5.409	3.990	32.2	1.95	7.110	6.150	9.74	5.13
10	714.0915	0.0451	0.24	6.017	4.613	30.0	1.85	6.215	5.359	14.04	8.00
11	714.0145	0.0459	0.18	4.612	3.231	25.0	1.55	4.233	3.614	12.23	5.75
12	713.2345	0.0459	0.17	4.394	3.014	25.5	1.58	4.416	3.774	10.61	4.77
13	713.2115	0.0459	0.20	5.058	3.674	27.0	1.65	4.776	4.079	13.08	6.65
14	726.1721	0.0484	0.18	4.366	3.060	29.2	1.76	5.876	5.070	8.29	3.91
15	726.1904	0.0484	0.19	4.573	3.266	29.8	1.80	6.214	5.373	8.61	4.23
16	727.0940	0.0498	0.23	5.24.	3.977	32.5	1.93	7.170	6.198	10.19	5.67
17	727.0816	0.0498	0.24	5.449	4.177	33.2	1.98	7.411	6.407	10.64	6.07
18	726.1439	0.0547	0.20	4.232	3.074	29.0	1.70	5.732	4.952	9.05	4.61
19	729.0645	0.0549	0.26	5.309	4.155	37.0	2.20	8.875	7.681	9.31	5.54
20	713.1345	0.0555	0.20	4.178	3.035	26.5	1.61	4.768	4.085	10.80	5.49
21	713.1300	0.0555	0.21	4.358	3.215	26.7	1.65	4.921	4.218	11.41	5.99
22	713.1159	0.0555	0.21	4.358	3.215	27.0	1.67	4.974	4.255	11.29	5.93
23	607.1030	0.0564	0.12	2.776	1.655	16.0	1.00	2.878	2.548	7.70	2.50
24	713.0915	0.0566	0.18	3.737	2.619	25.0	1.55	4.037	3.426	10.43	4.90
25	727.1300	0.0571	0.23	4.580	3.470	32.8	1.91	7.403	6.422	8.59	4.79
26	726.1256	0.0600	0.19	3.693	2.638	28.7	1.74	5.711	4.922	7.58	3.72
27	726.1158	0.0600	0.20	3.877	2.821	29.0	1.77	5.924	5.116	8.06	4.12
28	726.0928	0.0607	0.22	4.141	3.098	27.8	1.70	5.582	4.823	14.77	0.52
29	727.1500	0.0635	0.24	4.276	3.278	32.2	1.92	7.090	6.131	8.73	4.98
30	607.0230	0.0647	0.12	1.874	1.837	16.5	1.00	2.977	2.632	5.80	2.14

TABLE 6-1 (cont)

Event No	Identif.	$\dot{m}$ gm/sec	T Newton	$\bar{v}^+$ Km/second	$\bar{v}^-$ Km/second	I_L Amp.	V_L Kv	W_e^+ Kilowatt	W_e^- Kilowatt	η^+ Percent	η^- Percent
31	601.1300	0.0653	0.10	2.016	1.047	16.0	1.00	2.507	2.176	5.35	1.19
32	712.2230	0.0655	0.18	3.232	2.265	23.3	1.41	4.009	3.445	9.02	4.25
33	619.1831	0.0689	0.14	2.491	1.572	18.3	1.13	2.845	2.466	7.80	2.90
34	727.1701	0.0695	0.25	4.048	3.136	32.5	1.91	7.336	6.363	8.27	4.83
35	727.1755	0.0695	0.25	4.048	3.136	33.0	1.96	7.888	6.862	7.68	4.48
36	729.0359	0.704	0.27	5.492	4.336	36.5	2.20	9.344	8.119	9.45	5.73
37	620.0732	0.0722	0.15	2.514	1.636	17.0	1.05	2.617	2.277	9.08	3.64
38	515.0910	0.0727	0.15	2.498	1.627	19.0	1.13	5.212	4.666	4.46	1.79
39	515.0802	0.0727	0.16	2.635	1.764	21.0	1.20	5.799	5.196	4.48	1.92
40	708.1200	0.0728	0.15	2.494	1.624	17.5	1.10	2.629	2.270	9.00	3.60
41	620.1340	0.0742	0.15	2.450	1.596	17.2	1.10	2.637	2.284	8.80	3.52
42	712.1345	0.0750	0.18	2.824	1.979	22.0	1.33	3.883	3.371	8.09	3.82
43	729.0047	0.0757	0.28	5.674	4.518	36.0	2.18	9.004	7.809	10.49	6.47
44	620.0920	0.0762	0.12	1.988	1.158	17.0	1.10	2.616	2.269	5.92	1.81
45	522.1725	0.0771	0.12	1.966	1.145	16.0	0.96	2.581	2.248	5.92	1.81
46	727.2130	0.0775	0.26	3.763	2.945	34.0	1.97	8.383	7.313	6.96	4.15
47	625.1530	0.0778	0.11	1.820	1.007	16.1	0.93	2.106	1.823	6.25	1.66
48	522.2335	0.0784	0.13	2.061	1.254	16.8	1.04	2.799	2.438	6.14	2.09
49	515.0315	0.0792	0.18	2.673	1.873	22.0	1.25	6.270	5.621	4.66	2.22
50	523.0137	0.0795	0.14	2.160	1.363	17.0	1.06	2.868	2.498	6.70	2.49
51	606.2151	0.0808	0.14	2.125	1.341	17.0	1.07	3.277	2.903	5.72	2.14
52	625.0645	0.0841	0.15	2.160	1.407	16.8	1.00	2.319	2.003	8.84	3.54
53	625.0230	0.0847	0.12	1.791	1.043	16.4	0.98	2.165	1.863	6.47	1.97
54	712.1100	0.0847	0.18	2.496	1.749	22.1	1.34	3.796	3.276	7.34	3.46
55	728.2320	0.0853	0.30	3.885	3.141	35.1	2.03	8.741	7.624	7.86	5.01
56	727.2335	0.0861	0.26	3.385	2.649	32.7	1.92	8.0858	7.034	6.50	3.88
57	624.2350	0.0862	0.13	1.875	1.141	16.0	0.95	2.073	1.783	7.58	2.58
58	728.0120	0.0866	0.27	3.481	2.748	33.0	1.93	8.411	7.362	6.63	4.03
59	624.2030	0.0867	0.15	2.096	1.365	17.2	1.07	2.448	2.111	8.13	3.26
60	624.1825	0.0870	0.15	2.088	1.360	17.1	1.05	2.429	2.092	8.17	3.27

TABLE 6-1 (cont)

Event No	Identif.	$\dot{m}$ gm/sec	T Newton	$\bar{v}^+$ Km/second	$\bar{v}^-$ Km/second	I_L Amp.	V_L Kv	W_e^+ Kilowatt	W_e^- Kilowatt	η^+ Percent	η^- Percent
61	625.2200	0.0882	0.19	2.513	1.794	16.7	1.00	2.347	2.039	12.50	6.15
62	626.0500	0.0899	0.20	2.577	1.872	17.0	1.00	2.311	2.001	13.66	6.97
63	414.1351	0.0918	0.11	1.563	0.864	11.0	0.60	2.563	2.255	4.56	1.22
64	414.1340	0.0918	0.11	1.542	0.853	12.8	0.70	1.690	1.476	6.57	1.75
65	626.1500	0.0932	0.17	2.164	1.484	17.0	1.00	2.342	2.029	9.78	4.40
66	728.1940	0.0942	0.31	3.625	2.951	37.0	2.13	9.930	8.688	6.65	4.29
67	728.1545	0.0956	0.29	3.363	2.699	35.1	2.00	8.998	7.878	6.39	4.01
68	626.1100	0.0960	0.16	1.997	1.337	17.5	1.00	2.423	2.103	8.26	3.52
69	728.0510	0.0967	0.26	3.014	2.358	33.0	1.91	8.577	7.525	5.43	3.24
70	728.1420	0.1064	0.32	3.305	2.708	35.0	2.00	9.376	8.233	6.60	4.32
71	728.0815	0.1066	0.29	3.016	2.421	33.5	1.93	8.841	7.765	5.82	3.66
72	626.2300	0.1135	0.19	1.952	1.394	16.2	0.98	2.196	1.905	10.39	5.11
73	727.0500	0.1144	0.19	1.938	1.384	15.4	0.92	1.940	1.672	11.72	5.76
74	728.1130	0.1153	0.30	2.876	2.326	35.5	2.05	9.887	8.688	5.12	3.27
75	728.0945	0.1154	0.29	2.786	2.236	33.2	1.93	8.809	7.737	5.40	3.39
76	505.0340	0.1172	0.12	1.293	0.753	15.0	0.91	3.000	2.648	2.76	1.58
77	505.0320	0.1172	0.13	1.379	0.838	16.0	0.91	3.283	2.897	3.47	1.19
78	505.0250	0.1172	0.14	1.464	0.924	16.0	0.96	3.287	2.908	3.93	1.47
79	413.1420	0.1181	0.05	0.691	0.156	12.0	0.75	1.551	1.330	1.66	0.01
80	411.1837	0.1181	0.15	1.539	1.002	12.0	0.80	1.706	1.467	8.58	3.43
81	512.1711	0.1191	0.16	1.608	1.077	20.0	1.18	5.406	4.840	2.93	1.26
82	512.1405	0.1191	0.17	1.651	1.119	22.5	1.35	7.382	6.658	2.25	1.00
83	628.1100	0.1245	0.14	1.378	0.870	14.5	1.75	1.961	1.622	6.58	2.45
84	628.0600	0.1251	0.15	1.452	0.946	14.0	1.75	1.800	1.571	7.62	3.06
85	504.1532	0.1338	0.17	1.507	1.034	18.5	1.06	4.862	4.347	3.23	1.46
86	504.1217	0.1338	0.18	1.581	1.108	19.5	1.14	4.777	4.262	3.63	1.72
87	504.1551	0.1338	0.20	1.731	1.258	18.2	1.00	4.515	4.037	4.62	2.37
88	507.0627	0.1694	0.16	0.757	0.105	16.0	0.91	3.371	2.991	3.32	1.42
89	507.0513	0.1694	0.20	1.367	0.993	17.9	1.00	4.115	3.664	4.01	2.06

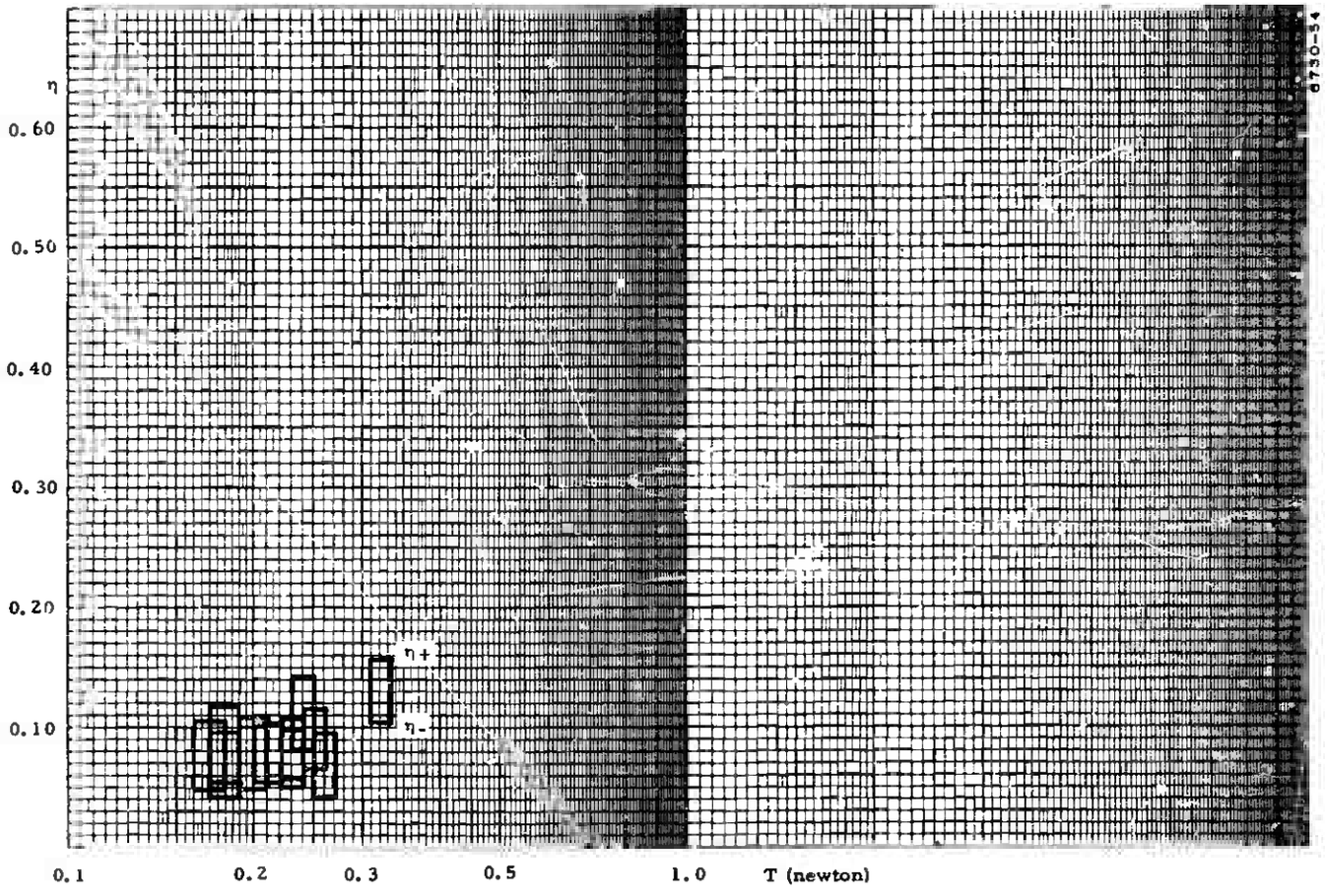

Figure 6-1. Efficiency vs Thrust for $3.5 < \dot{m} < 5.5 \times 10^{-5}$ Kg/sec

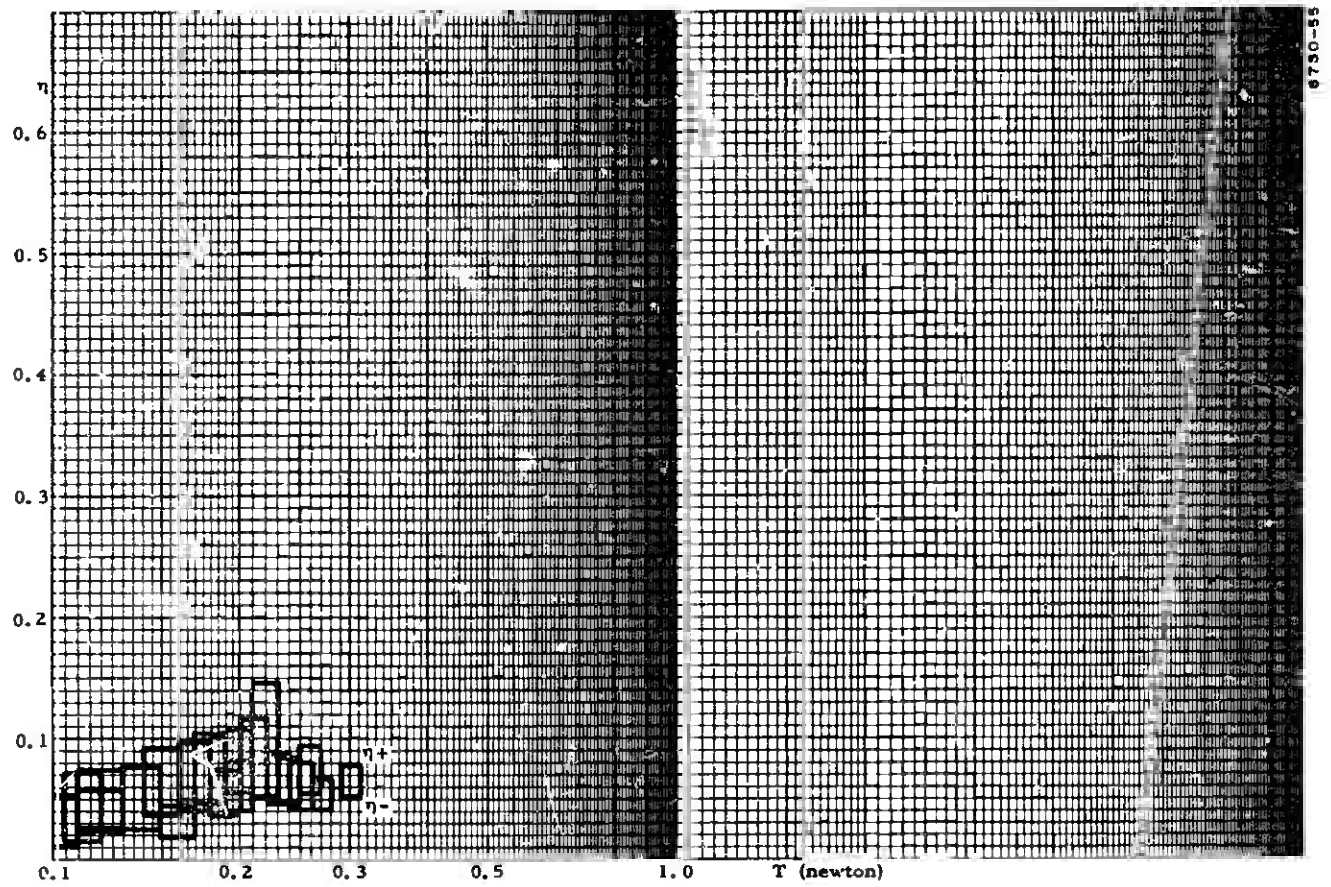

Figure 6-2. Efficiency vs Thrust for $5.5 < \dot{m} < 9 \times 10^{-5}$ Kg/sec

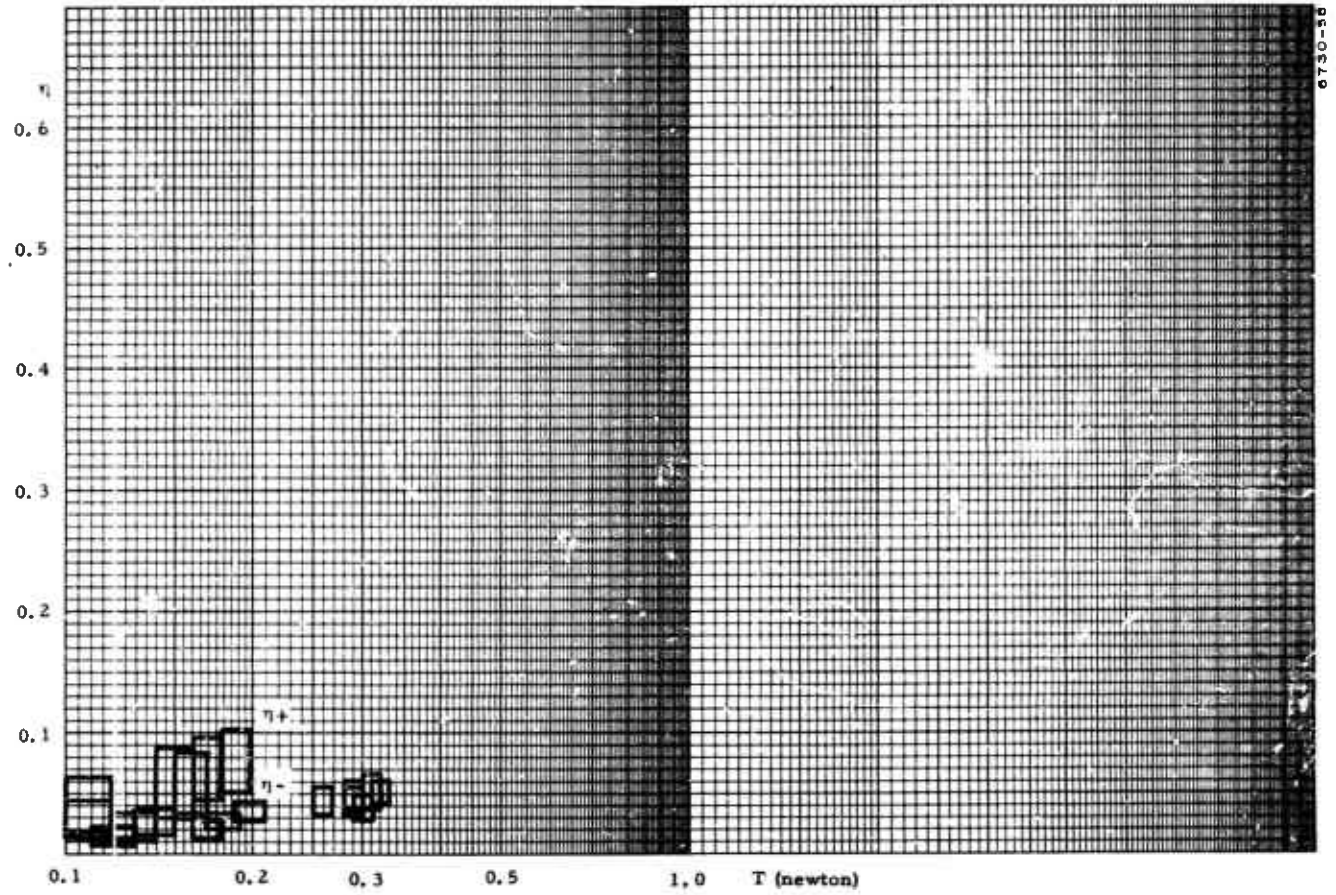

Figure 6-3. Efficiency vs Thrust for $9 < \dot{m} < 16 \times 10^{-5}$ Kg/sec

of the series; it was also obtained with the lowest mass flow (3.5×10^{-5} K_g/sec). Inspection of Figures 6-4 through 6-7 shows that this point does not belong to an orderly extrapolation of the other measured values, but rather indicates some change of the functional law of dependence of performance on current, voltage and/or velocity. Figure 6-8 shows efficiency τ as a function of current 1_L for a mass flow of 3.5 and 3.8×10^{-5} Kg/sec, with the data points represented by the usual rectangles. The peculiar position of point No. 03, above the orderly extrapolation of the other measured values, may indicate the approach of a transition to higher efficiency; however, in view of the results of Section 2.3, it appears more likely that, from this combination of mass flow and current, the threshold could be reached more easily by an increase of mass flow rather than an increase of current. This indeed was contemplated in the plans for the continued testing of the coil, but was prevented by the failure of the coil. The conditions corresponding to point No. 03 were maintained for one hour and three minutes; the inner coil failed at a weak spot when an attempt was made to increase the coil current prior to a new scan of the mass flow range from a minimum to a maximum.

Figure 6-9 is a reproduction of the traces recorded during the observation of point No. 03. The duty cycle was temporarily reduced to 50% to see whether a better vacuum in the chamber would make any difference (it did not; all readings taken below 5×10^{-4} torr were independent of pressure). For comparison, also shown are the traces of point No. 70 in which a similar value of thrust was obtained with a much larger mass flow at a much lower efficiency.

Figure 6-9 also illustrates the effect of the mass flow fluctuations, due to the play in the feed pump, on the electrical quantities. Since the mass flow is the lowest ever used, and the wear in the pump is the worst (being this point, 03, the latest in the series), the induced fluctuations in current and voltage, as well as phase, are quite noticeable. Capacitor C_s was adjusted to tune out the series resonant circuit under conditions of average mass flow, as indicated by $\theta = 90°$ ($\cos \theta = 0$). This condition happens to be closely obtained during the firing period indicated by an asterisk, and the reported readings are taken there. It is of interest to note that the phase angle θ is a sensitive indicator of mass flow loading: a swing in one direction indicates a mass flow lower than average, in the other higher, as shown on the trace of $\cos \theta$. Inspection shows that when the mass flow drops below average, current and voltage climb above average, and the thrust record shows fast fluctuations as if conditions in the thrustor were at the threshold of an instability. This is not the case for point 70.

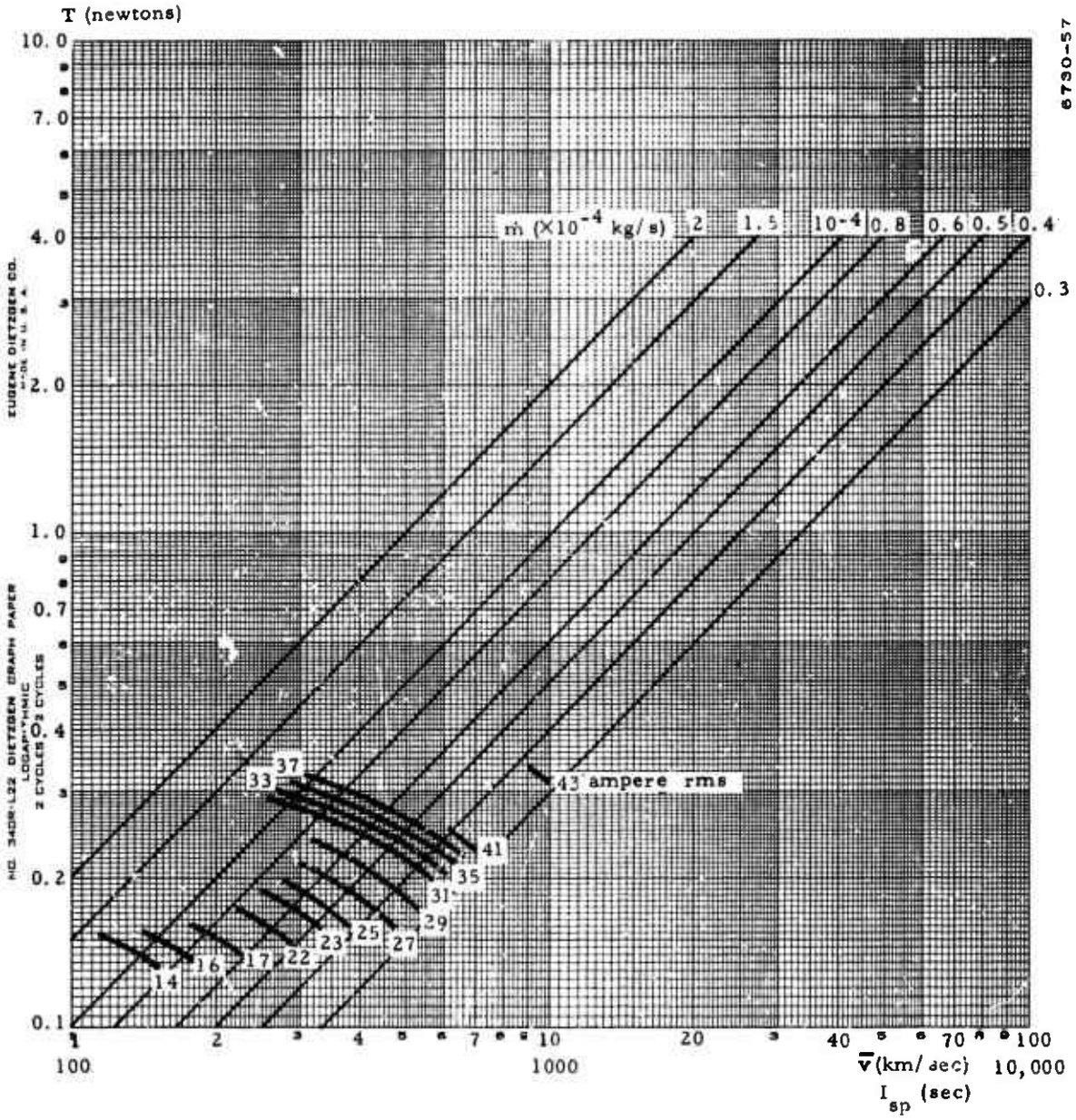

Figure 6-4. Contours of Constant Current I_L in the $(T, \bar{v})$ Plane

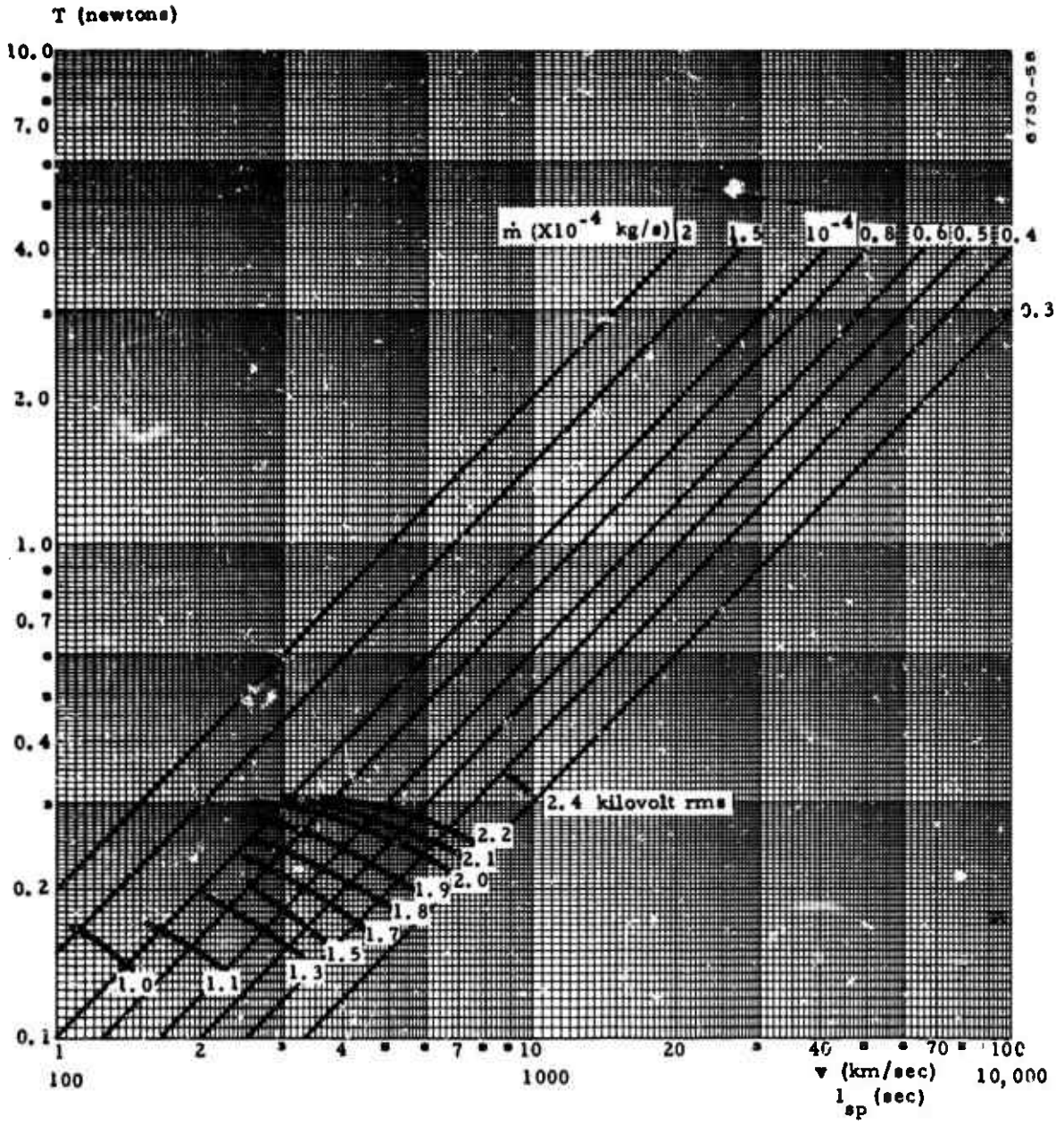

Figure 6-5. Contours of Constant Voltage V_L in the (T, $\bar{v}$) Plane

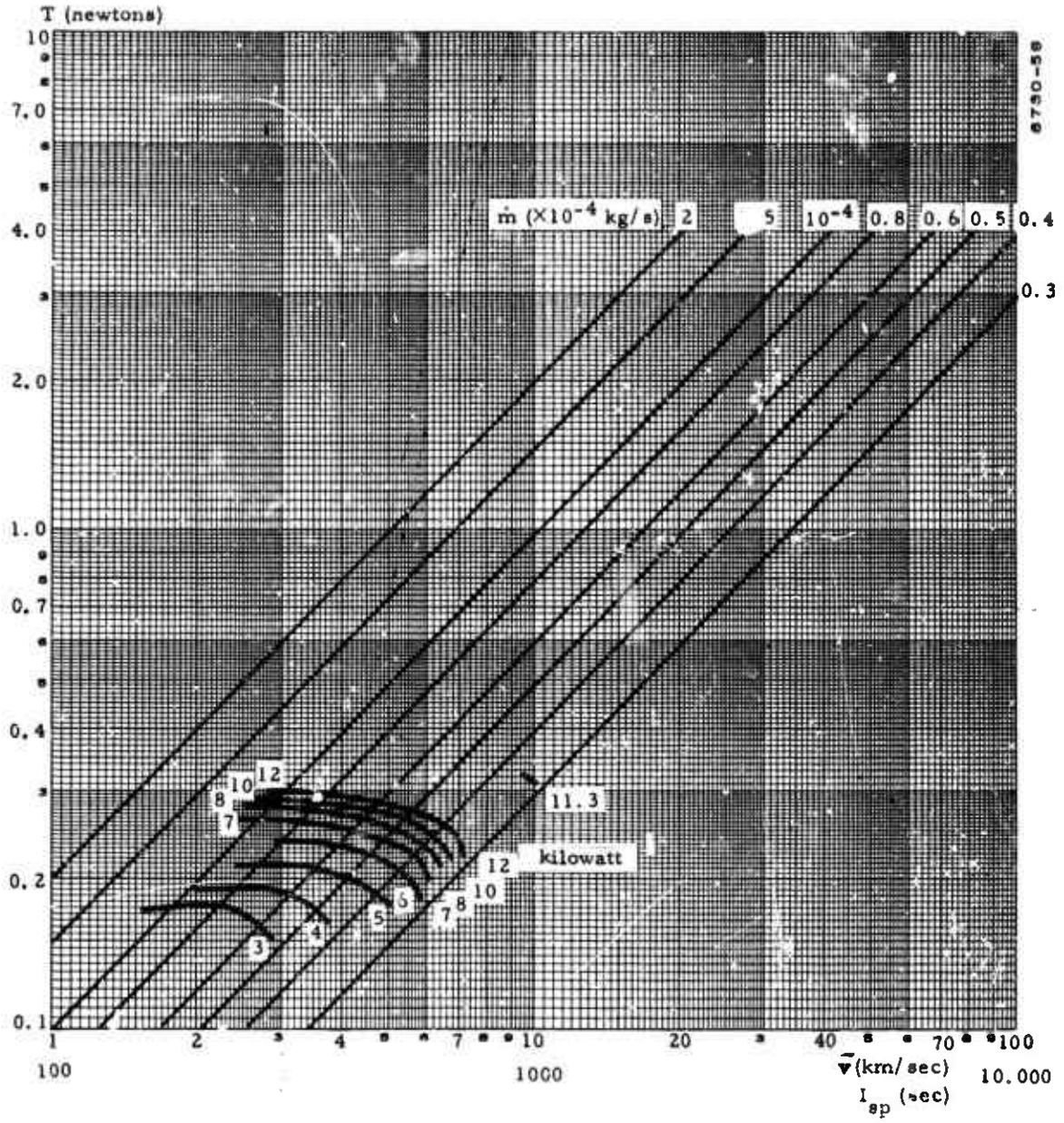

Figure 6-6. Contours of Constant Power W_e in the (T, $\bar{v}$) Plane

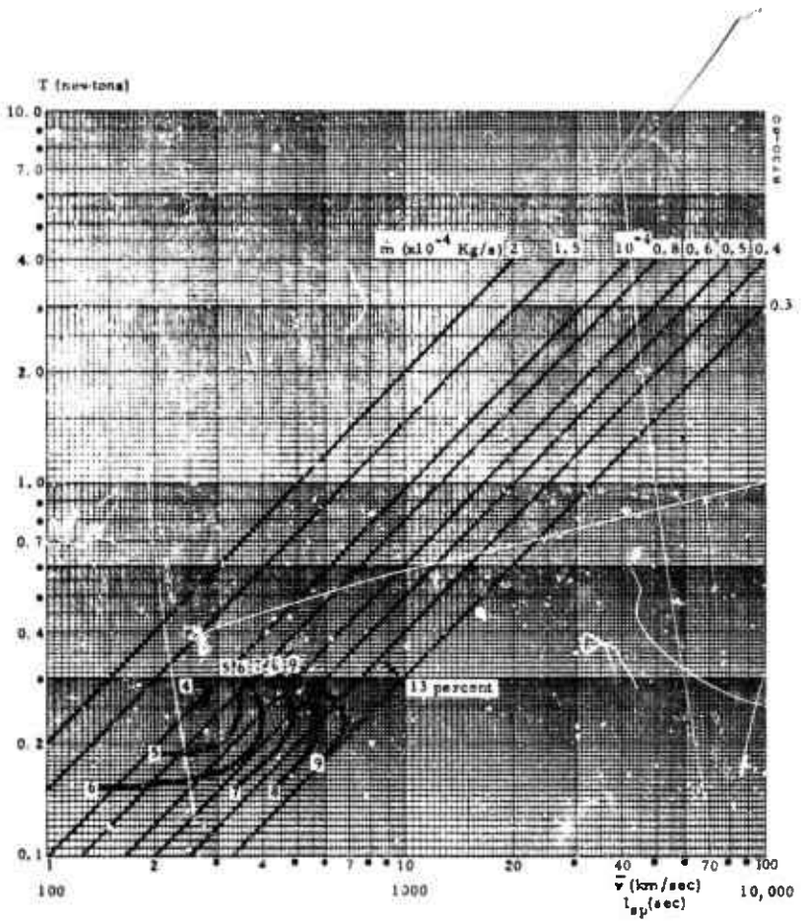

Figure 6-7. Contours of Constant Efficiency η in the $(T, \bar{v})$ Plane

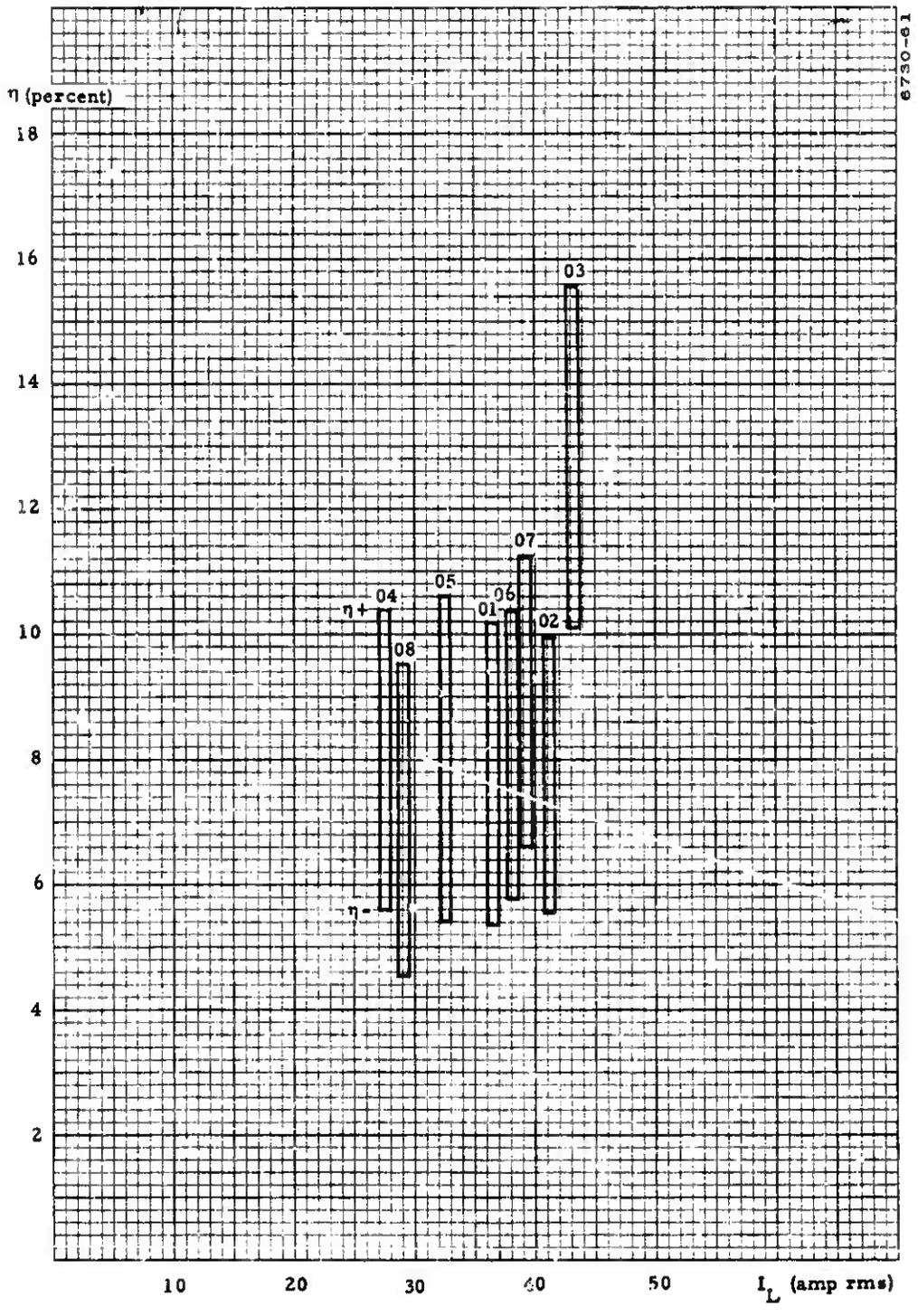

Figure 6-8. Efficiency vs coil current I_L ($\dot{m}$ = 3.5, 3.8 × 10^{-5} Kg/sec)

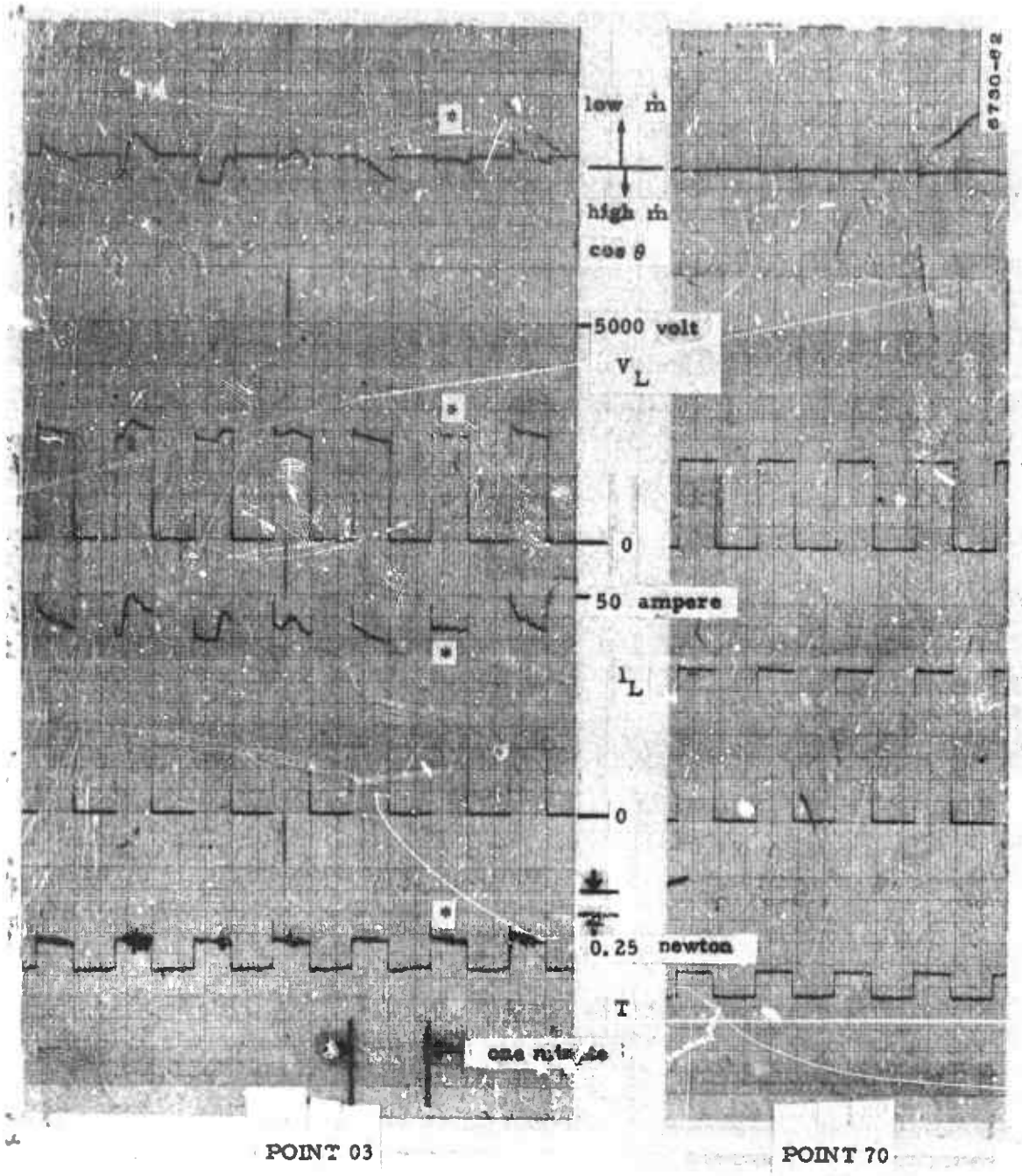

Figure 6-9. Recorded Traces of Observed Performance

6.3 MASS UTILIZATION

The loss of efficiency from the theoretical values can be attributed either to excess power required to ionize the mercury vapor above 10.4 electron-volts per ion pair, or to lack of ionization for part of the effluent mass, or to a combination of both mechanisms.

If we assume that the total mass flow $\dot{m}$ is divided in two components, the ionized fraction $\dot{m}$ and the neutral fraction $\dot{m}_o$, we can define the mass utilization η_m

$$\eta_m = \frac{\dot{m}_i}{\dot{m}} = \frac{\dot{m}_i}{\dot{m}_i + \dot{m}_o}$$

Then, if we assume that $\dot{m}_i$ is accelerated and supplies the entire measured thrust, while $\dot{m}_o$ is not accelerated at all and supplies no measurable thrust*, we can compute the average velocity of the accelerated component

$$\bar{v}_* = T/\dot{m}_i = T/\eta_m \dot{m}_i = \bar{v}/\eta_m$$

and the efficiency of the acceleration process

$$\eta_* = T^2/2\, m_i\, W_e = T^2/2\, \eta_m\, m_i\, W_e = \eta/\eta_m .$$

If the mass efficiency can be independently measured, it becomes possible to obtain an indication of the relative importance of the two aspects of the ionization process: how many ions are made, and how much power is spent in making them. An estimate of η_m is obtained by plotting the observed points on a graph, derived from the basic theory, in which the presentation is very sensitive to η_m and nearly independent of the other

*In other words, if we assume that the mean-free-path λ for charge exchange collisions is large compared with the dimensions of the interaction region. The information in Figure 2-45 shows that this assumption is not far from the truth.

parameters. Such graph is found in the form of a family of curves of constant η_m in the $(T/I_1, \dot{m})$ plane, already shown as Figure 2-47.

The result is shown as Figure 6-10. The experimental points cluster is a well defined band, with very low scatter, with approximately $0.05 < \eta_m < 0.1$. Whereas Figure 6-10 provides an immediate visual presentation of the distribution of η_m, Table 6-2 shows the corresponding value for each observed point, identified by the same number as in Table 6-1. Also shown are the values of $\bar{v}_*$ and η_* (since both $\bar{v}_*$ and η_* are inversely proportional to η_m, it is easy to compute the error limits v_*^- and v_*^+ as well as η_*^- and η_*^+ taking the non-starred values from Table 6-1 if desired. This was not done in Table 6-2 for simplicity). In addition, Table 6-2 shows the energy per ion pair, in electron volts, corresponding to that fraction of the input power which is not accounted for elsewhere. The information contained in Table 6-2 can be presented in graphical form in the $(T, \bar{v}_*)$ plane, corresponding to Figures 6-4 through 6-7, except that now the velocity axis refers to the velocity of the ionized fraction only of the total mass flow (see Figures 6-11 through 6-14); the presentation of Figure 6-11 is of particular interest because it affords a direct comparison with the theoretical predictions of Figure 2-44. It can be seen that the agreement is quite good. By inspection of these figures one comes to the conclusion that the thrustor accelerates very effectively the ionized fraction of the effluent mass, and that the loss of efficiency is predominantly associated with the escape of non-ionized mass. Also, the ionization mechanism appears to be effective in the sense that not many electron-volts are required to ionize those atoms which are ionized. It appears therefore that a substantial increase of performances can be expected by the action of any mechanism which can increase the number of ions present in the interaction region.

The existence and effectiveness of a mechanism of this sort has been observed in electrodeless inductive discharges before; not only under Contract AF33(657)-8697, but also during a project sponsored by the Air Force Office of Scientific Research (AF 49(638)-1251, which was concerned primarily with making accurate electrical measurements of the operating power and the resistance and inductance reflected into the driving circuit by the plasma[5], and during a project sponsored by the

[5] Penfold, A. S., and Warder, R. C., "Research on Electromagnetic Plasma Acceleration, Volume II, An Investigation of the Various Plasma Mischarges Surrounding a Solenoidal Coil Excited with Current at 4 Megacycles," Final report, Contract AF 49(638)-1251, Litton Publication 5865, January 1967.

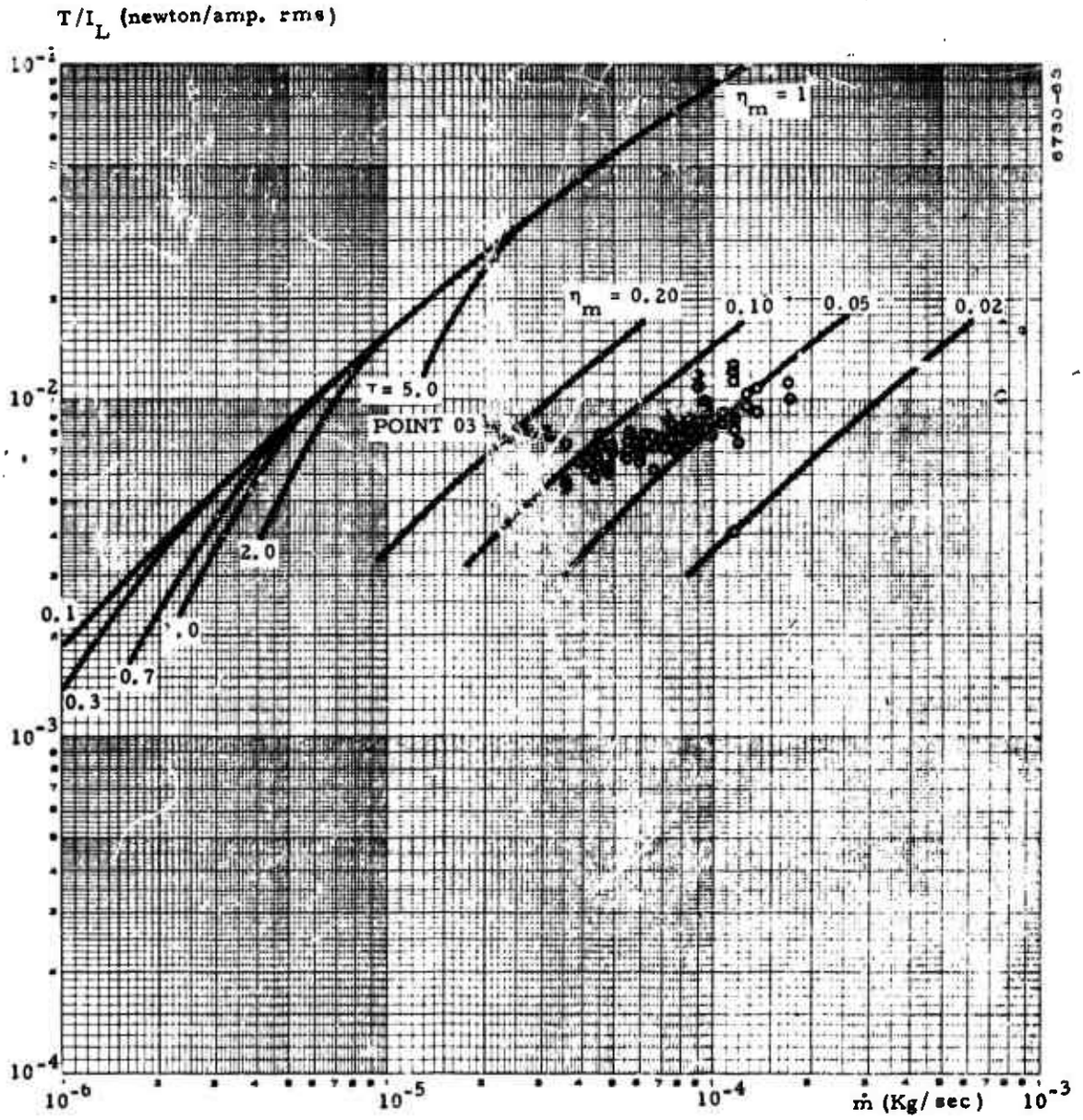

Figure 6-10. Mass Utilization

TABLE 6-2

PARAMETERS OF IONIZED FLOW

Event No.	T/I_L	η_m	$\bar{v}^*$	η^*	$\frac{e-v}{ion}$
01	0.00575	0.092	64.62	84.2	781
02	0.00560	0.087	74.85	88.8	706
03	0.00744	0.121	74.87	105.9	
04	0.00656	0.097	48.70	89.8	269
05	0.00611	0.091	57.67	87.5	473
06	0.00621	0.087	62.67	92.4	324
07	0.00657	0.093	63.77	95.8	176
08	0.00620	0.085	48.12	82.4	496
09	0.00652	0.083	56.62	89.5	374
10	0.00799	0.108	49.21	102.0	
11	0.00719	0.092	42.62	97.7	42
12	0.00666	0.087	42.57	88.3	239
13	0.00740	0.094	46.44	104.9	
14	0.00616	0.075	49.50	81.3	565
15	0.00637	0.077	50.90	83.3	519
16	0.00707	0.084	54.91	94.4	179
17	0.00722	0.088	54.69	94.9	160
18	0.00689	0.074	49.36	92.2	204
19	0.00702	0.077	61.45	96.4	140
20	0.00754	0.080	45.08	101.8	
21	0.00786	0.088	43.02	98.8	21
22	0.00777	0.085	44.54	101.	
23	0.00750	0.081	27.35	62.9	442
24	0.00719	0.074	42.94	103.5	
25	0.00701	0.073	55.13	91.6	278
26	0.00662	0.065	48.70	86.9	358
27	0.00689	0.068	49.24	89.5	284
28	0.00791	0.080	45.24	95.5	95
29	0.00745	0.071	53.19	96.5	101
30	0.00727	0.068	27.28	58.3	533
31	0.00624	0.056	27.34	58.3	535
32	0.00772	0.071	38.71	93.4	105
33	0.00765	0.067	30.32	79.8	233
34	0.00769	0.069	52.05	94.9	145
35	0.00757	0.067	53.61	90.7	294

TABLE 6-2 (cont)

Event No.	T/I_L	η_m	$\bar{v}^*$	η^*	$\frac{e\text{-}v}{ion}$
36	0.00739	0.064	76.78	118.5	
37	0.00882	0.076	27.30	83.6	146
38	0.00789	0.066	31.25	47.3	091
39	0.00761	0.064	34.36	49.9	186
40	0.00857	0.073	28.20	86.3	126
41	0.00872	0.072	28.09	85.5	133
42	0.00818	0.066	36.38	90.2	144
43	0.00777	0.064	79.65	132.5	
44	0.00705	0.055	28.60	70.2	347
45	0.00750	0.060	25.92	64.4	373
46	0.00764	0.061	54.98	91.0	298
47	0.00683	0.053	26.66	74.6	243
48	0.00773	0.060	27.62	68.5	351
49	0.00818	0.064	35.51	53.7	1090
50	0.00823	0.065	27.10	70.6	305
51	0.00823	0.062	27.95	63.3	453
52	0.00892	0.067	26.61	92.3	58
53	0.00731	0.052	27.24	81.1	173
54	0.00814	0.059	35.97	91.5	120
55	0.00854	0.062	56.66	103.7	
56	0.00795	0.057	52.92	91.0	276
57	0.00812	0.056	26.92	90.7	74
58	0.00818	0.056	55.61	95.1	157
59	0.00872	0.063	27.46	90.3	80
60	0.00877	0.062	27.80	92.2	65
61	0.01137	0.081	26.58	115.1	
62	0.01176	0.085	26.17	121.3	
63	0.01000	0.077	15.75	37.5	415
64	0.00859	0.058	20.64	71.7	168
65	0.01000	0.069	26.43	102.7	
66	0.00837	0.054	60.88	101.2	
67	0.00826	0.054	56.12	96.2	121
68	0.00914	0.061	27.32	96.5	26
69	0.00787	0.050	53.72	86.7	444
70	0.00914	0.054	55.67	101.1	

TABLE 6-2 (cont)

Event No.	T/I_L	η_m	$\bar{v}^*$	η^*	$\frac{e\text{-}v}{ion}$
71	0.00865	0.051	53.30	92.9	216
72	0.01172	0.066	25.34	117.4	
73	0.01233	0.069	24.07	126.6	
74	0.00845	0.045	67.79	93.2	244
75	0.00873	0.047	53.42	93.5	199
76	0.00799	0.042	24.07	51.0	558
77	0.00812	0.043	25.65	53.9	565
78	0.00874	0.047	25.40	57.4	480
79	0.00416	0.020	21.17	41.7	628
80	0.01250	0.072	17.64	83.4	62
81	0.00799	0.041	32.34	50.4	031
82	0.00755	0.038	36.44	42.7	786
83	0.00965	0.047	23.61	94.8	30
84	0.01071	0.055	21.80	97.0	14
85	0.00918	0.042	29.89	55.1	729
86	0.00923	0.042	32.01	63.6	587
87	0.01098	0.051	29.30	68.5	396
88	0.01000	0.038	11.34	62.3	77
89	0.01117	0.042	27.76	71.4	310

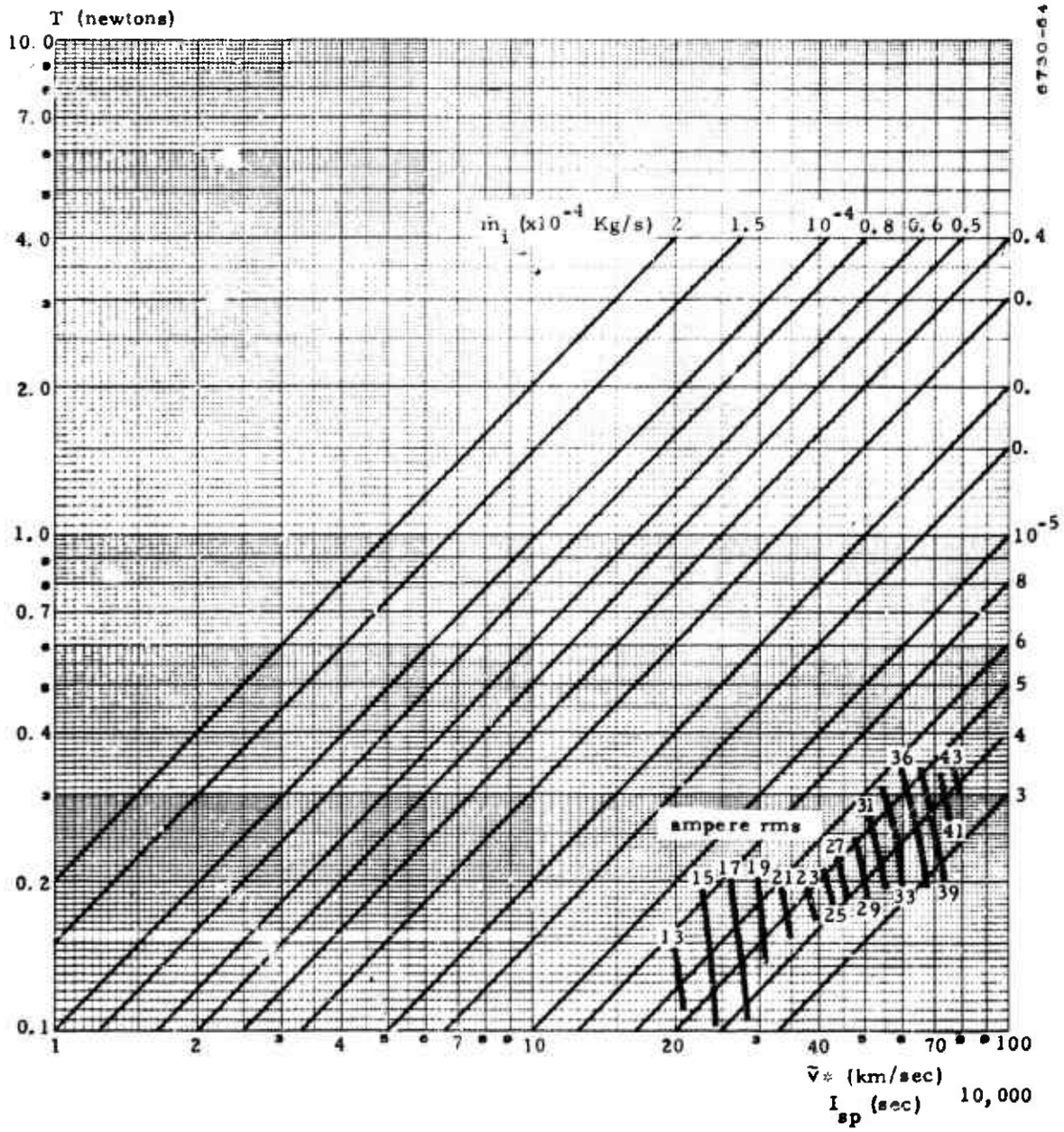

Figure 6-11. Contours of Constant I_L in the (T, $\bar{v}_*$) Plane

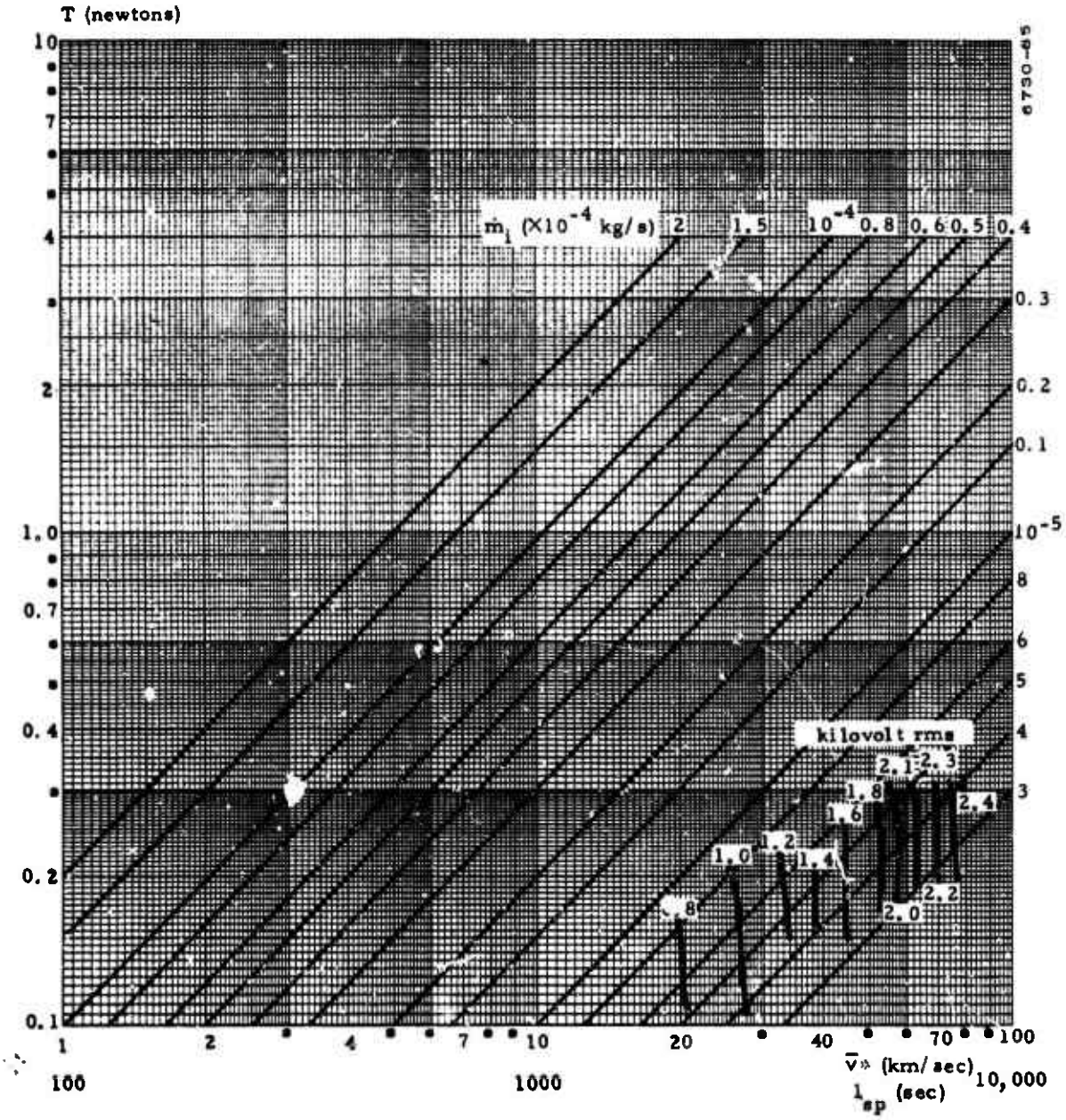

Figure 6-12. Contours of Constant V_L in the (T, $\bar{v}_*$) Plane

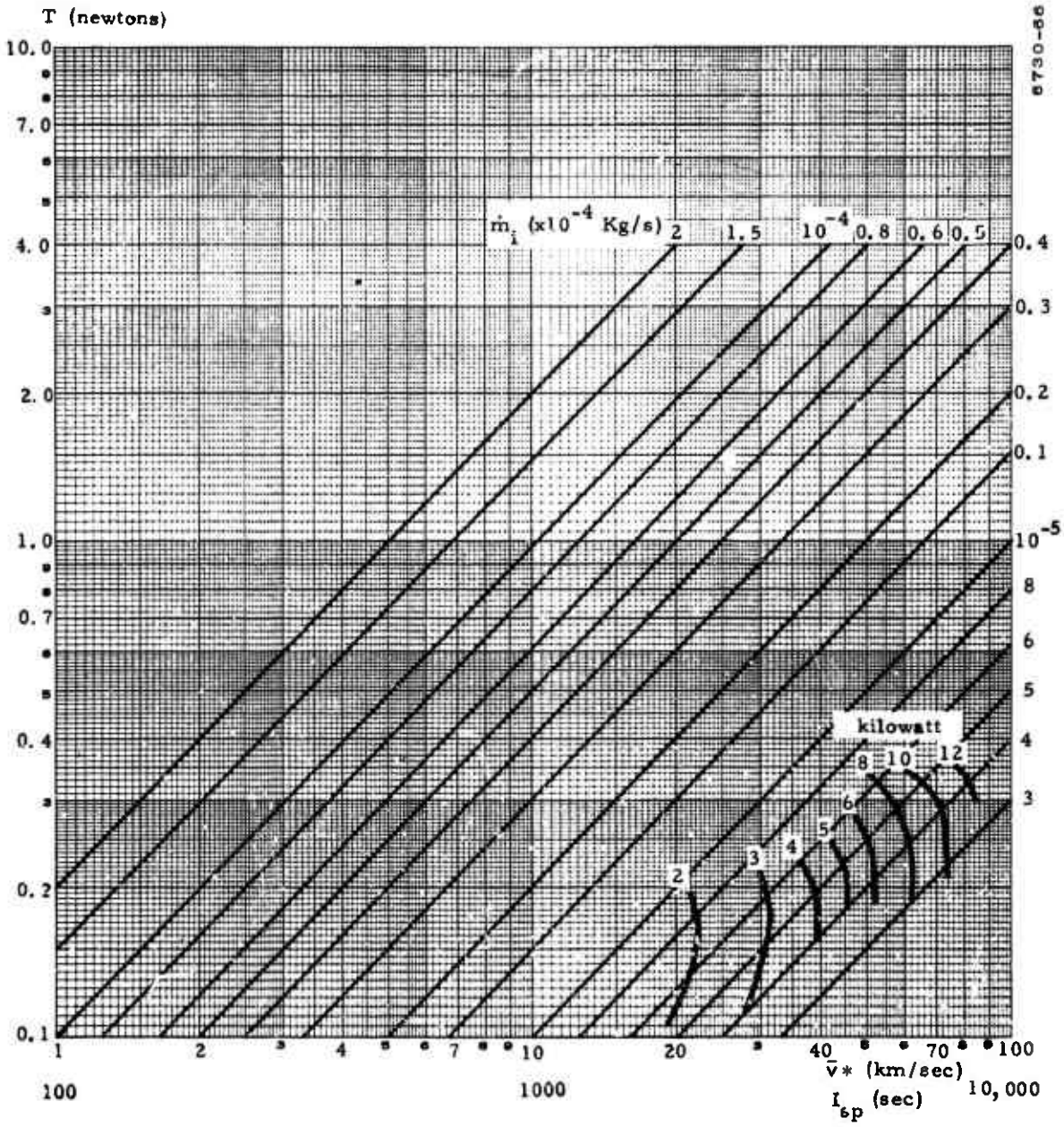

Figure 6-13. Contours of Constant W_e in the (T, $\bar{v}_*$) Plane

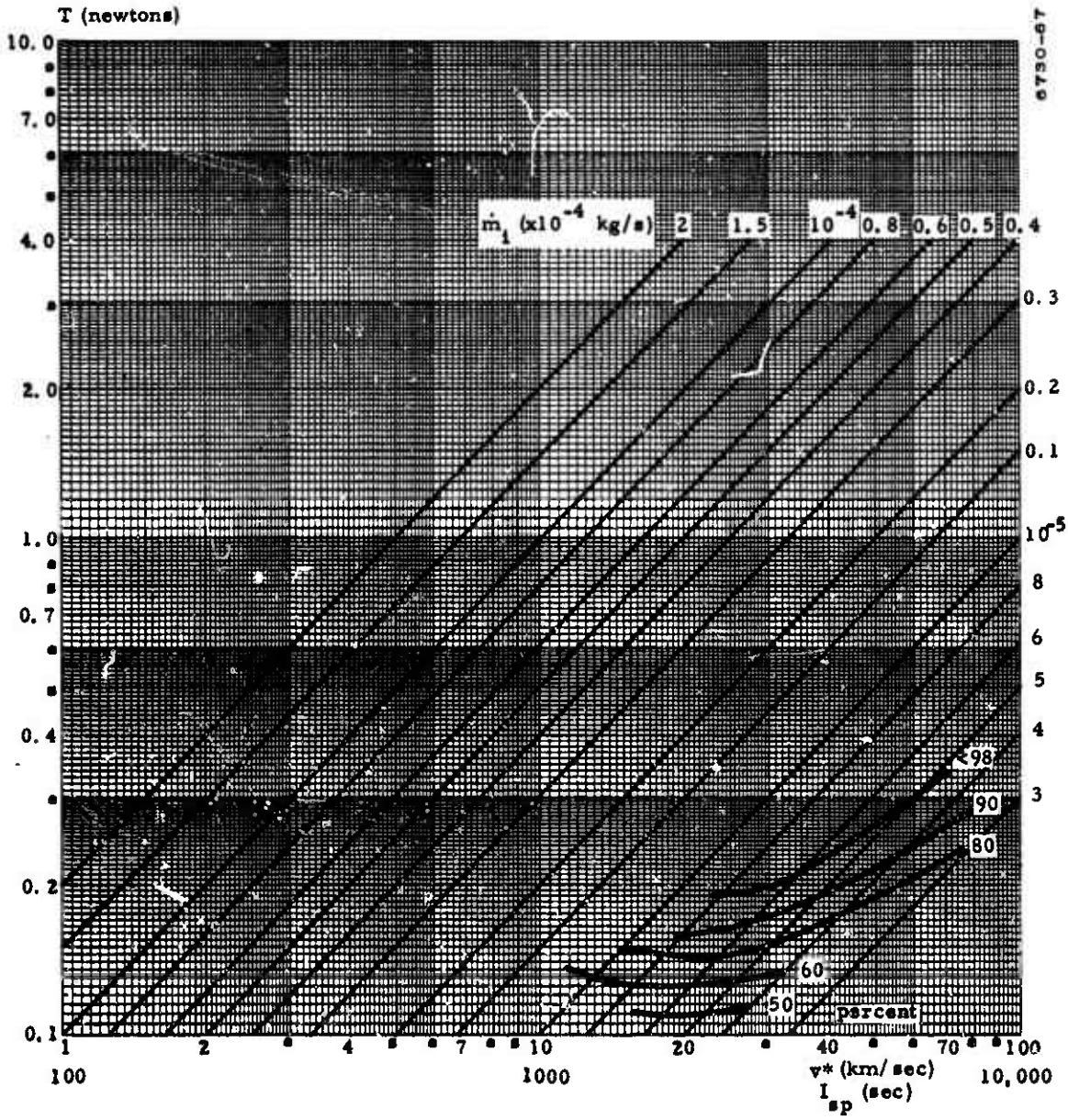

Figure 6-14. Contours of Constant η_* in the (T, $\bar{v}_*$) Plane

Army Engineering laboratory, Fort Belvoir, Virginia (DA-44-009-AMC-1447 T), in which the emphasis was directed toward making extensive diagnostic measurement of the plasma state using spectroscopic, microwave, and probe techniques[6]. In all cases the transition was observed to be abrupt and to be a function of the applied drive: when the applied current and/or voltage and/or magnetic field induction exceeded a definite threshold, then the gas conductivity increased by a very large factor.

The available evidence seems to indicate that this mechanism can be expected to begin to operate, in the case of the thrustors, at coil currents above approximately 70 amperes. Since coil currents of this magnitude have not been reached in the course of the contract, the exact location of the threshold boundary has not been identified.

[6] Thornton, J. A., "An Investigation of the Energy Exchange Processes in Nonequilibrium Plasmas," Final report, Contract DA-44-009-AMC-1447 (T), Litton Publication 5794, January 1967.